nature
photonics

Image reconstruction
in nonlinear media

5

COVER IMAGE

In nonlinear media, internal wave mixing typically renders signal information unreadable. Now Christopher Barsi and his coworkers have shown how digital holography techniques can deconvolve the nonlinear distortions and reconstruct the image-wave, anywhere along its propagation path. In the future, the technique may benefit applications such as material characterization and super-resolved microscopy.

Letter p211;
News & Views p195

ON THE COVER

Magnetic recording
Plasmonic assistance
Article p220

Silicon photonics
Slow-light-enhanced nonlinearity
Letter p206

Atom optics
Gigahertz-bandwidth probe
Article p225

Ready for action. Construction of the National Ignition Facility in the United States is now finally complete and tests are starting that involve all 192 of its high-power laser beamlines.
Editorial p177
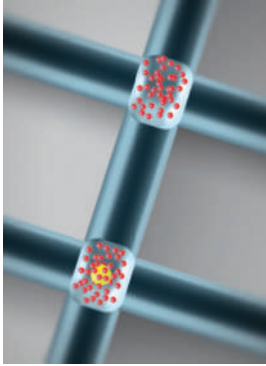
Exploiting the Faraday effect in vapour cells containing hot gas atoms may offer a route for performing quantum information processing.
Article p225;
News & Views p197

NIF wakes up

The first step towards the goal of nuclear fusion triggered by laser beams has been taken with the construction and test firing of the National Ignition Facility in the United States.

In the small hours of Thursday 26 February, while most of the residents of California were safely tucked up in bed asleep, one of the largest laser experiments in the world was awakening. Just before 2 a.m., the National Ignition Facility (NIF) in Livermore fired all 192 of its high-power laser beams into a target chamber for the very first time. Each beamline carried a pulse of ultraviolet laser energy with an average of 420 J into the centre of the target chamber, resulting in a total of 80 kJ being deposited. From the point of view of energy, this represents twice the 40-kJ capability of the giant OMEGA laser at the University of Rochester, USA, which has been running since 1995 and combines 60 laser beams.

The ultimate goal at NIF is to ramp up the energy of its 192 beams so that a colossal 1.8 MJ of energy can be delivered to a tiny hollow gold target cylinder filled with deuterium and tritium, and thus trigger nuclear fusion. The idea is that the intense nanosecond-duration laser beams generate a 'bath' of soft X-rays that heat the outer layer of the fuel causing it to explode, generating shock waves that will compress its core to 100 times the density of lead. This will cause it to reach a temperature of more than 100 million degrees Celsius and pressures that are thousands of times that of the Earth's atmosphere. The fuel core will then ignite and thermonuclear burn will quickly spread through the compressed fuel, releasing 10 to 100 times more energy than the amount deposited by the laser beams. Well, that's the theory anyway.

The February beam firing marks the unofficial completion of the NIF project, which has taken 10 years to build, cost around US$3.5 billion and been plagued by controversy, delays and overspending. The Department of Energy project was originally due for completion by 2004 for a budget of $1.2 billion. In 2000 it was bailed out with further funding and an extension of the construction schedule to 2008, but the project leaders had a tough time persuading members of the US Congress that it should be continued. Finally, the last of the giant project's 6,206 optical components was installed on 26 January this year, ahead of a federal deadline of 31 March for the project's
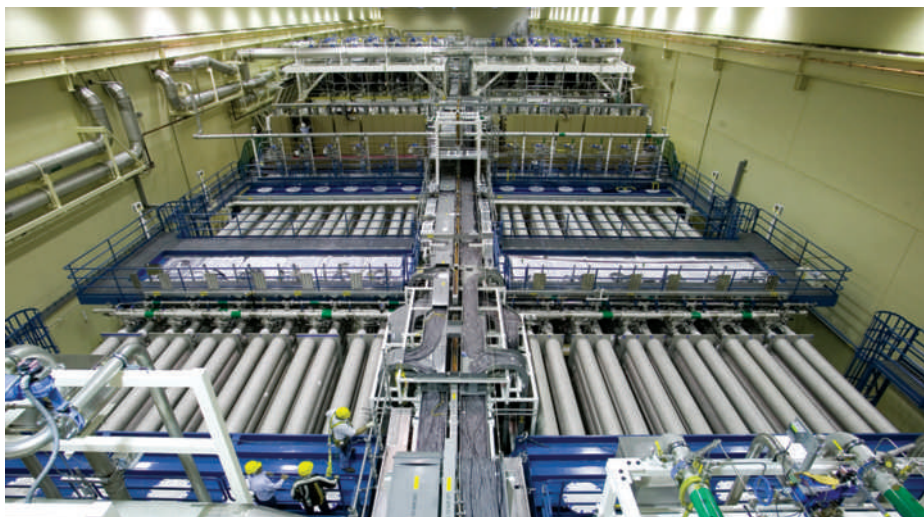
Internal view of one of NIF's laser bays showing several of its beamlines. The facility is now complete.

completion. Although NIF's staff must be breathing a sigh of relief that construction is now finished, the daunting task of achieving fusion and a net energy release is still ahead. The hope is that this will be accomplished within the next two years, with experiments due to commence shortly.

Europe is not far behind in the laser fusion game, with its own project nearing completion. Laser Mégajoule (LMJ), a similar facility to NIF, is being built in Bordeaux, France, by the French atomic agency CEA and is due for completion next year, two years behind schedule. It aims to deliver a similar energy to NIF but will feature 240 beamlines, divided into eight groups of 30.

LMJ and NIF will be followed by a giant European project called HiPER (the High Power laser Energy Research facility), which was formally launched in October 2008 and is now in a planning and preparatory stage. It is estimated to be operational sometime around 2020. HiPER involves 25 scientific institutions from 11 European nations and the location of the facility has not yet been announced, although the United Kingdom is understood to be a strong contender. Once constructed it hopes to build on the 'proof of principle' results from NIF and LMJ to demonstrate a more commercially practical approach to sustained laser fusion using 'fast ignition', which in principle is more

efficient. Unlike NIF and LMJ, which use a single simultaneous burst of energy from all their laser beams both to compress and to heat the target, HiPER will split the process into two discrete stages involving different lasers. One set of beams will compress the target, followed almost instantaneously by a secondary picosecond laser beam that will heat the compressed target and drive it to ignition. The attraction of the scheme is that it relaxes the requirements on the energy of the compression laser beams and the manufacture of the fuel target. The downside is that the scheme is as yet unproven and so there are no guarantees that it will work. Another difference between NIF, LMJ and HiPER is that the latter would be developed as a civilian research facility and would not have the military ties with defence research that have in the past generated criticism and opponents for existing laser fusion schemes. A forerunner test facility to HiPER, called PETAL, is being built in the Aquitaine region in France to test the science behind the fast ignition scheme.

Whether HiPER will provide unequivocal proof that laser fusion is indeed a practical approach to addressing mankind's energy generation problems is not yet clear. What is clear is that much fascinating laser and nuclear physics, a mountain of engineering challenges and a large sum of money will be involved in trying to find out. ❐

A bright future for synchrotron imaging

To the Editor — Among the analytical techniques able to yield molecular information about biological samples, a growing interest in Fourier transform infrared (FTIR) microscopy[1] has emerged during the past decade. However, there are technical challenges and limitations when applying FTIR microscopy to biological issues, owing to the limited brightness of commercial infrared sources, and the poor sensitivity and resolution of detectors. These problems have prevented high-quality analysis of thick soft-tissue sections (>20–30 μm) (ref. 2), single cells (~10 μm in size) and hard tissues such as bone or teeth[3]. We wish to draw attention to the fact that, thanks to the emergence of high-brightness synchrotron sources equipped with focal plane array (FPA) detectors, this situation now looks set to change.

A synchrotron source has the capability of providing infrared light through a 10-μm pinhole that is 2–3 orders of magnitude brighter than a conventional Globar such as those available in commercial FTIR instrumentation[4]. This superior signal-to-noise ratio (SNR) is expected to allow imaging with a spatial resolution down to the diffraction limit, or to allow analysis of thicker samples while maintaining good spatial resolution[5].

Although FTIR microscopes are now available on most of the infrared synchrotron facilities around the world (see www.lightsources.org/cms/), only a few research studies have quantitatively validated the expected advantages of a synchrotron for biomedical applications. So far, the main success obtained by combining a FTIR microscope with a synchrotron source is hard-tissue analysis[6], which has provided results that are not possible with standard sources. However, FTIR microscopy on soft tissues and cells has still not taken advantage of the performance of synchrotron sources, largely owing to detector limitations.

The availability of the infrared FPA detector[7] and its recent installation at ultra-bright synchrotron radiation facilities around the world (Table 1) promises to extend the performance and overcome the existing limitations[8]. In particular, FPA detectors promise to reduce data acquisition time from hours to minutes, improving the

spectral quality and overcoming possible contributions from synchrotron radiation instability. But because no commercially available optical microscopes have been designed for use with an infrared synchrotron source, the optimal match between such sources and FPA detectors is still at the early stage of development. Linear arrays of small size coupled to an infrared microscope promise to achieve fast imaging and increase performances in terms of both spatial and time resolutions. However, the use of FPA infrared detectors optimized in the mid-infrared range seems the best solution to collect fast infrared images over large tissue areas, because of their sensitivity and speed of read-out. Alignment and optimization of these devices remains a challenge when noise or instabilities are present and because of optical layout limitations. A huge effort has already been made, with many ideas implemented and others under investigation at third-generation storage ring facilities, to improve stability and, as a consequence,

spatial resolution, contrast and acquisition time of an image. There is thus a brilliant future for infrared synchrotron microscopy and imaging, and important results in biological and biomedical applications are expected in the coming years. ❏

References
1. Petibois, C. & Déléris, G. *Trends Biotechnol.* **24**, 455–462 (2006).
2. Petibois, C. et al. *Analyst* **131**, 640–647 (2006).
3. Mendelsohn, R. et al. *Appl. Spectrosc.* **54**, 1183–1191 (2000).
4. Cestelli-Guidi, M. et al. *J. Opt. Soc. Am.* **22**, 2810–2817 (2005).
5. Smith, T. D. *Nucl. Instrum. Methods Phys. A* **483**, 565–570 (2002).
6. Burghardt, A. J. et al. *Bone* **40**, 160–168 (2007).
7. Colarusso, P. et al. *Appl. Spectrosc.* **52**, 106A-120A (1998).
8. Moss, D. et al. *Infrared Phys. Technol.* **49**, 53–56 (2006).

C. Petibois and G. Déléris
Université de Bordeaux, CNRS UMR 5084, 146 Rue Léo Saignat, 33076 Bordeaux-Cedex, France.
e-mail: cyril.petibois@u-bordeaux2.fr

M. Piccinini, M. Cestelli-Guidi and A. Marcelli
INFN—Laboratori Nazionali di Frascati, Via E. Fermi 40, 00044 Frascati (Roma), Italy.

Table 1 | Infrared synchrotron beamlines with current and planned FPA detectors.

Country	Synchrotron facility	Beamline
Germany (Karlsruhe)	ANKA (planned)	Beamline IR2 http://ankaweb.fzk.de
Italy (Frascati)	DAΦNE (installed)	Beamline SINBAD www.lnf.infn.it/dafnel
Italy (Trieste)	ELETTRA (installed)	Beamline SISSI www.elettra.trieste.it/info/index.html
Sweden (Lund)	MAX-Lab (installed)	Beamline 73 www.maxlab.lu.se
UK (Oxfordshire)	Diamond (under commission)	Beamline 22 www.diamond.ac.uk/Beamlines/Beamlineplan/B22/index.html
China (Hefei)	NSRL (under commission)	Beamline U4 www.nsrl.ustc.edu.cn/EN
Australia (Melbourne)	Australian Synchrotron (under commission)	IR Beamline www.synchrotron.vic.gov.au/content.asp?Document_ID=490
USA (Berkeley)	ALS (installed)	Beamline 1.4.4 www-als.lbl.gov
USA (Brookhaven)	NSLS (installed)	Beamline U10B www.nsls.bnl.gov
USA (Madison)	SRC (under commission)	Beamline 031-IR www.src.wisc.edu

Bruker Hyperion 3000 FTIR imaging systems are available in all facilities, except at ALS and NSLS where Thermo-Nicolet Continuum XL systems are available.

Prospects for LED lighting

Siddha Pimputkar, James S. Speck, Steven P. DenBaars and Shuji Nakamura

More than one-fifth of US electricity is used to power artificial lighting. Light-emitting diodes based on group III/nitride semiconductors are bringing about a revolution in energy-efficient lighting.

Since the development of incandescent light bulbs in the late 1800s, various methods of producing white light more efficiently have been investigated. Of these, white-light sources based on light-emitting diodes (LEDs) look set to have a considerable impact on issues such as energy consumption, environment and even the health of individuals. Roughly 22% of the electricity generated in the United States is dedicated to lighting applications[1]. If all conventional white-light sources in the world were converted to the energy-efficient LED light sources, energy consumption could be reduced by around 1,000 TW h yr^{-1}, the equivalent of about 230 typical 500-MW coal plants, reducing greenhouse gas emission by about 200 million tonnes (ref. 2).

White-light sources based on reliable and energy-efficient LEDs have only recently been made possible through developments in semiconductors (Fig. 1 shows a white-light LED in action). It is possible to generate light in semiconductor materials (such as GaN or AlInGaP) by injecting electrons into the conduction band of the material and providing lower-energy sites ('holes') in the valence band into which they can fall, thereby creating light of a colour corresponding to the energy gap between the conduction band and valence band, also called the bandgap. A light-emitting diode is an electronic device integrating electrical access to the bandgap structure and allowing for efficient light generation.

LEDs essentially consist of three different types of materials layered on top of each other. The bottom layer has a high concentration of free electrons (for example n-type GaN doped with Si) followed by multiple alternating thin layers (1–30 nm) of material with a smaller bandgap (InGaN/GaN), also called quantum wells. The sandwiching of a smaller-bandgap material (InGaN) between layers of larger-bandgap material (GaN) creates a well that spatially traps electrons and holes, allowing them to recombine efficiently, generating light with the wavelength of the smaller-bandgap material. Above this 'active layer', there is a layer of material with a high concentration of holes (p-type GaN doped with Mg).

Until recently, the only high-luminosity LEDs available emitted red light. For white light, however, two or more wavelengths are required to generate a broad spectrum of light that is a better approximation of a black-body radiation curve, such as that of the Sun. One way to produce additional colours is to use a material that absorbs light of one wavelength and emits at longer wavelength.

Phosphors are commonly used for this task and a select few have received considerable attention, such as rare-earth-doped yttrium aluminium garnets (YAG:RE). For example, cerium-doped YAG can absorb blue and ultraviolet light and emit yellow light relatively efficiently[3]. Crucial to this process is the fact that higher-energy light (for example ultraviolet or blue) is converted to lower energy (for example yellow or red). Therefore, LEDs emitting red light cannot be used for white-light generation using phosphors; instead a short-wavelength ultraviolet, violet or blue LED is required.

Early attempts to produce blue-emitting semiconductors focused on SiC, but these devices proved inefficient (0.03% efficiency[4]) owing to the material's indirect bandgap. The GaN revolution has since provided efficient ultraviolet, violet and blue light emitters. GaN is a direct-bandgap semiconductor material with a 3.45-eV bandgap, which corresponds to near-ultraviolet light (364 nm). GaN was first investigated as a potential material for LEDs in the late 1960s by Paul Maruska and Jacques Pankove at the Radio Corporation of America (RCA) and in later years additionally by Isamu Akasaki and co-workers at Nagoya University in Japan and by Shuji Nakamura at Nichia Corporation.

After many years of research, great advances were made by growing high-quality GaN on a foreign material, sapphire (Al_2O_3), in 1986 (ref. 5) and then by demonstrating p-type conductivity in GaN doped with Mg by activating the material in a post-growth anneal[6]. These breakthroughs led to the first high-efficiency blue LEDs of the time (1.5% efficiency[7]) in 1992, and then to the first viable blue and green LEDs at efficiencies up to 10% in 1995 (ref. 8). Recent developments[9] have also yielded high-brightness, yet still rather inefficient, yellow LEDs.

Largely owing to these achievements, it is now possible to generate white light using LEDs. The three most popular approaches are shown in Fig. 2a. These are a blue LED with yellow phosphors; an ultraviolet LED with blue and yellow phosphors (or red, green and blue phosphors); and a device that combines red, green and blue LEDs. Figure 2b presents
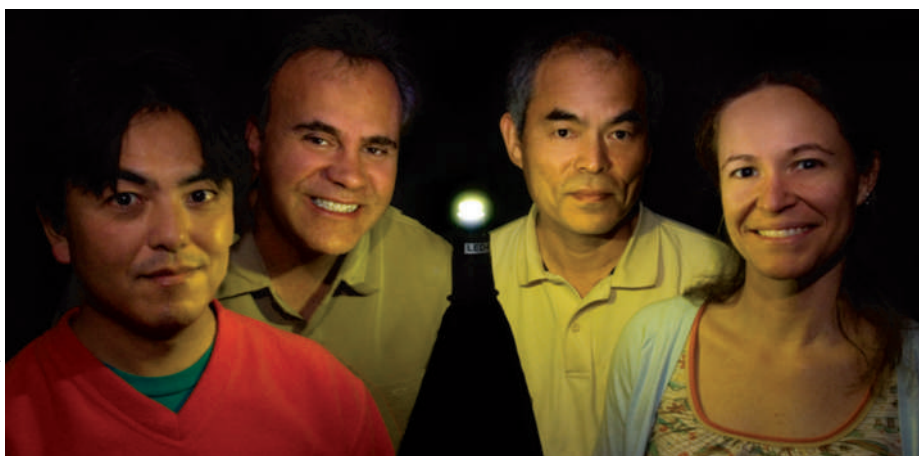
Figure 1 | White light from a cone-shaped LED illuminates researchers from the University of California, Santa Barbara. From left to right, Hisashi Masui, Steve DenBaars, Shuji Nakamura, Natalie Demille.

RANDY LAMB, UCSB
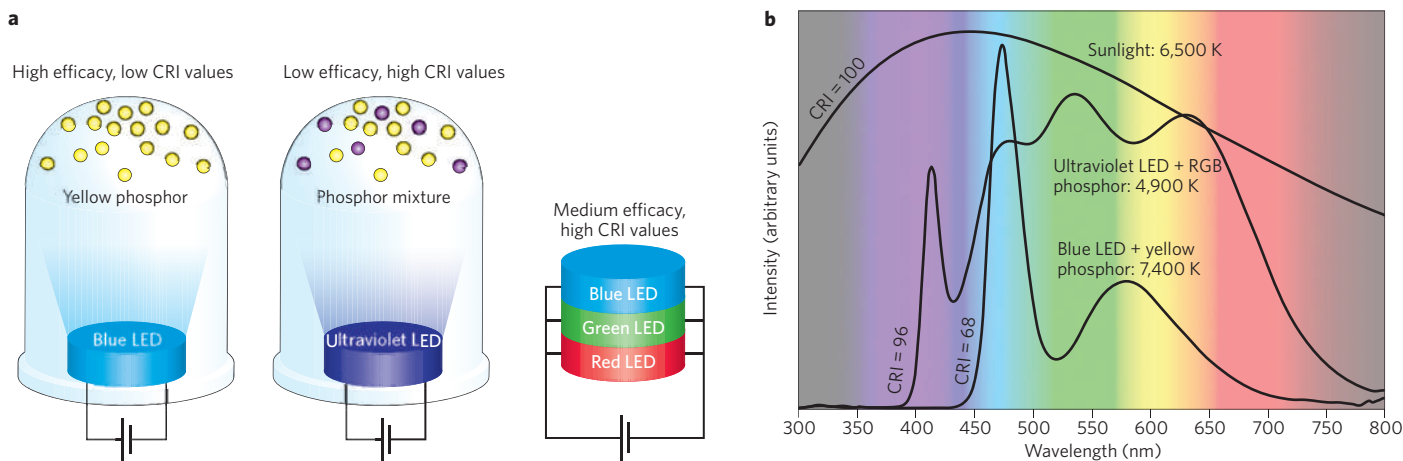
Figure 2 | White light based on LEDs. **a**, Three dominant ways to produce white light based on LEDs. **b**, Comparison of the spectrum of ideal sunlight with two LED-based white-light sources.

the spectra for two phosphor-based white LEDs and sunlight.

Naturally there are pros and cons to each of the schemes. The advantage to using a blue LED and a yellow phosphor is its high theoretical efficacy, which is attractive for the creation of a cheap, bright white-light source. However, this benefit comes at the expense of a lower value for the colour-rendering index (CRI; see Box 1 for definition), which is typically so low that such devices are undesirable for indoor use. Ultraviolet LEDs with phosphor mixtures provide a better CRI value and are suitable for indoor applications but at the expense of poorer efficacy. To control white light dynamically, the third approach, a combination of three (or more) LEDs of different wavelengths is attractive, and may lead to higher efficacies than the ultraviolet–phosphor LEDs, but will generally be the most expensive option until further advances are made. The historic development of luminous efficacy for the most common white-light sources is shown in Fig. 3.

Performance parameters

There are several key performance parameters to consider when discussing LEDs. Recent research has heavily focused on improving the external quantum efficiency (EQE), which is commonly defined as the product of the injection efficiency, the internal quantum efficiency (IQE) and the extraction efficiency. The injection efficiency is the ratio of electrons being injected into the quantum wells to those provided by the power source, the IQE is the ratio of photons generated to the number of electron–hole recombinations, and the extraction efficiency is the ratio of photons leaving the LED to those generated.

Box 1 | The metrics for judging a white-light source

Luminous efficacy

To quantify the energy efficiency of a white-light source, it is common to consider its ability to produce a visual sensation. This quantity, called luminous efficacy, derives from convoluting the spectral power distribution of the light source with the spectral sensitivity of the human eye, which peaks at 555 nm (green). Luminous efficacy is calculated by taking the ratio of the produced visual sensation (expressed in lumens, where 1,700 lumens is roughly equal to the light output of a 100-W incandescent bulb) to the electrical power required to produce the light (expressed in watts).

Colour temperature

White light may be classified as being warm, neutral or cold and is referenced with respect to the white light emitted by an ideal white-light source, for example black-body radiation sources such as the Sun or a body at a certain temperature. As the temperature of an ideal black body is raised from 2,000 K to 10,000 K, the emitted white light goes from reddish ('warm') through to bluish ('cold'). LEDs can currently be engineered from warm through to cold (2,500 K to 10,000 K), although cost and efficiency factors need to be considered.

In the case of white-light generation using phosphors, a conversion efficiency factor (the ratio of emitted longer-wavelength photons to shorter-wavelength absorbed photons) also needs to be factored into the EQE determination.

Without filters, incandescent bulbs typically glow a warm yellowish white. Fluorescent lights are generally bluish, but recent phosphor engineering has pushed their colour into the warmer, yellowish white.

Colour-rendering index

Another important parameter is the ability to reproduce colours of an object as seen under an ideal white-light source, such as the Sun. By illuminating eight standard colour reference samples, first with an ideal white-light source (at the same colour temperature as the source being tested), then with the white-light source of interest, it is possible to quantify the deviation in reflected spectra. From these deviations, the colour-rendering index (CRI) is determined. In this scheme sunlight and incandescent bulbs have a value of 100, which is ideal. Other white-light sources reproduce the colour of objects with varying degrees of perfection, signified by a lower CRI. Generally, values above 80 are considered sufficient for indoor lighting, whereas lower values are acceptable for outdoor lighting (street lights). Metal halides have CRI values between 85 and 95, LED-based white-light sources 60–95, fluorescent lamps 50–90, mercury vapour 20–50 and sodium lamps 5–20.

Future progress should depend on improvements in each of these areas: IQE; light extraction efficiencies; elimination of significant roll-off in EQE when operating LEDs at high currents to push today's peak laboratory EQE values
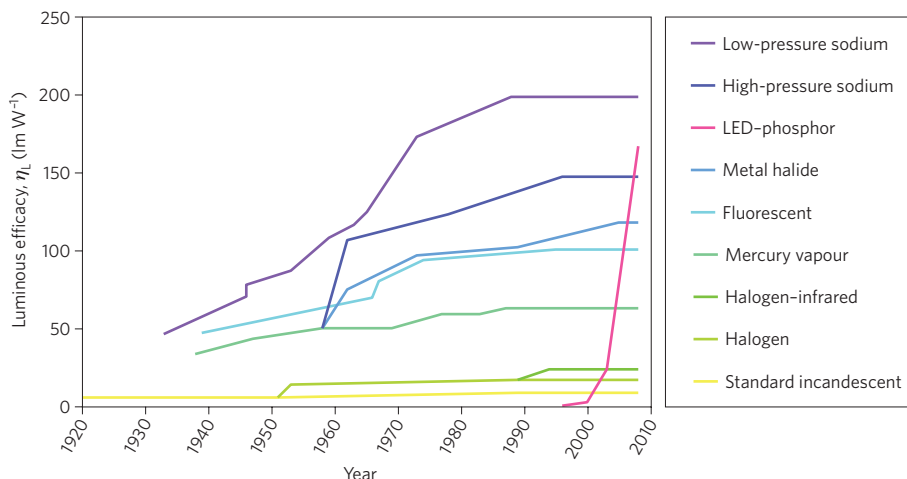
Figure 3 | Historic development of the most common white-light sources and improvements in their ability to produce white light efficiently. The theoretical limit for luminous efficacy η_L is less than 420 lm W^{-1} for good-quality white light, and 263 lm W^{-1} for a blue LED combined with a yellow phosphor. For definition of luminous efficacy, see Box 1. (Data from refs 2, 21.)

of ~75% (ref. 10) to higher values; and phosphor conversion efficiency.

The IQE of today's best LEDs is at least 75% (ref. 10) and may even be approaching 80%. To make further improvements towards 100% IQE, non-radiative recombination centres need to be eliminated. More importantly, a shift is needed in growing the LEDs, from polar to nonpolar or semipolar crystallographic directions instead, to eliminate strain-induced electric polarization fields currently seen within the quantum wells[11]. Generally speaking, polar devices, which are currently the dominant devices produced in industry, are proving to be inferior to nonpolar devices as recombination is not as efficient. This topic is currently an important research area, as semiconductor growth techniques in nonpolar crystallographic directions are still immature[12]. Growing in nonpolar or semipolar directions allows the device structure to be further optimized, for example by increasing the thickness of the quantum wells[13], thereby further increasing the IQE.

When it comes to the extraction efficiency, because of large differences in the refractive indices of air and the GaN materials system, a considerable fraction (90–95%) of the generated photons within the LED are trapped by total internal reflection. Methods under investigation include ways to increase the amount of light hitting the LED–air interface at near-perpendicular values to reduce the occurrence of total internal reflections (for example, surface roughening techniques to generate microscale cones on the surface[14], optimizing the exterior shape of the LED chip and patterning the sapphire substrate

to reduce light scattering), and methods of eliminating the passage of light through certain layers of material by integrating or embedding photonic crystals into the LED[15].

An important mystery that needs to be solved in the near future is the decrease in EQE seen when operating at higher current densities (over 10 A cm^{-2}) when trying to increase the luminous flux (currently about 160 lumens per power LED chip, roughly equivalent to a 30-W incandescent bulb). This 'efficiency droop' may be associated with enhanced Auger recombination[16], or possibly carrier overflow from the quantum wells due to the high carrier population[17]. Although the exact cause has not yet been determined, it is believed that using thicker quantum wells and altering the structure to lessen carrier overflow will reduce this to the point that it will be possible to operate at higher efficacies and currents. Progress is also being made in optimizing the phosphor materials and mixtures to improve conversion efficiencies[18] and improve the quality of the white light through longer-wavelength phosphor emission. This needs to continue[19].

Bright future

White-light sources based on LEDs have a promising future. Continued advances are expected to exceed Haitz's law[20], which forecasts that every 10 years the amount of light generated by an LED increases by at least a factor of 20, while the cost per lumen drops by at least a factor of 10. The ultimate goal for LED-based white lighting is to replace all incandescent bulbs and compact fluorescent lamps to provide an energy-efficient and long-lasting option for everyday use. It is anticipated that cost-effective

drop-in replacements for incandescent bulbs will be readily available in the next couple of years once mass-produced LEDs have comparable metrics to the best LEDs in research laboratories today and the electronic circuits that operate LED structures have improved efficiencies and form factors.

Ultimately it is clear that LEDs will result in reduced energy costs for lighting, and will also eliminate the exposure to mercury found in fluorescent bulbs. Although initial costs may seem steep to an end-user (LEDs are today around 50 times as expensive as incandescent light bulbs and around seven times the cost of compact fluorescent lamps, based on normalized light output), when averaged out over the lifetime of the product LEDs are actually already a cheaper solution (around a seventh of the price of incandescent bulbs and two-thirds the price of compact fluorescent lamps) and will soon become more so.

So what are the ultimate limitations to white LED performance? The key constraints, the theoretical maximum efficacy (~260 lm W^{-1}) and, when operating under high currents the thermal management and degradation of the polymer material that encapsulates the LED and suspends the phosphor materials. Despite these limitations and current challenges, it is anticipated that further advances in white LEDs will revolutionize the lighting industry and lead us into a more energy-efficient and bright future. ❑

Siddha Pimputkar, James S. Speck, Steven P. DenBaars and Shuji Nakamura are in the Materials Department, Solid State Lighting and Energy Center (SSLEC), University of California, Santa Barbara, California 93106, USA.
e-mail: shuji@engineering.ucsb.edu

References
1. Department of Energy. *Solid State Lighting Research and Development, Multi-Year Program Plan FY'09–FY'14.* <http://www1.eere.energy.gov/buildings/ssl/projects.html> (2008).
2. Krames, M. R. *et al. J. Disp. Technol.* **3,** 160–175 (2007).
3. Allen, S. C. & Steckl, A. J. *Appl. Phys. Lett.* **92,** 143309 (2008).
4. Edmond, J. A. *et al. Physica B* **185,** 453–460 (1993).
5. Amano, H. *et al. Appl. Phys. Lett.* **48,** 353–355 (1986).
6. Nakamura, S. *et al.* US patent 306,662 (1994).
7. Akasaki, I. *et al. Inst. Phys. Conf. Ser.* **129,** 851–856 (1992).
8. Nakamura, S. *et al. Jpn. J. Appl. Phys.* **34,** L797–L799 (1995).
9. Sato, H. *et al. Appl. Phys. Lett.* **92,** 221110 (2008).
10. Narukawa, Y. *et al. Phys. Status Solidi A* **205,** 1081–1085 (2008).
11. Waltereit, P. *et al. Nature* **406,** 865–868 (2000).
12. Yamada, H. *et al. Phys. Status Solidi* **2,** 89–91 (2008).
13. Kim, K.-C. *et al. Appl. Phys. Lett.* **91,** 181120 (2007).
14. Fujii, T. *et al. Phys. Status Solidi C* **2,** 2836–2840 (2005).
15. Erchak, A. A. *et al. Appl. Phys. Lett.* **78,** 563–565 (2001).
16. Shen, Y. C. *et al. Appl. Phys. Lett.* **91,** 141101 (2007).
17. Vampola, K. *et al. Appl. Phys. Lett.* **94,** 061116 (2009).
18. Allen, S. C. *Appl. Phys. Lett.* **92,** 143309 (2008).
19. Ronda, C. R. *J. Luminesc.* **72-74,** 49–54 (1997).
20. Steele, R. V. *Nature Photon.* **1,** 25–26 (2007).
21. Flesch, P. *Light and Light Sources* (Springer, 2006).

A new twist to tuning lasers

Self-organizing liquid crystals could spawn a new breed of extremely useful and cheap tunable lasers. Such lasers may ultimately prove to be useful for creating flat-screen displays with better colours, enhanced sensors and compact medical instruments. *Duncan Graham-Rowe* takes a closer look.

The term 'self-assembly' has in recent years become synonymous with the field of nanotechnology. But now, thanks to the naturally occurring, self-organizing behaviour of liquid crystals, we could soon see lasers being self-assembled too. According to the scientists developing them, such liquid crystal lasers would be tiny and highly tunable, and ultimately so cheap that they could be made disposable.

These new lasers work by combining the properties of a laser dye with those of the natural photonic bandgap created by the periodic structures of liquid crystals, particularly cholesteric liquid crystals which have a periodic helical structure and are regarded as a one-dimensional photonic crystal. By controlling the degree to which these crystals twist, and therefore their periodicity, it is possible to tune the output wavelength of the lasers.

The potential benefits of these lasers are huge, says Stephen Morris who works as part of a research team led by Harry Coles at the Centre for Molecular Materials for Photonics and Electronics at Cambridge University, UK. This is because liquid crystal lasers combine the best features of dye, gas and solid-state lasers, leaving their respective drawbacks behind, says Morris.

Although dye lasers offer highly wavelength-tunable output, they tend to be rather large. Similarly, gas lasers are also bulky and have fixed wavelengths. On the other hand, semiconductor lasers, such as those used in DVD players, may be small but their wavelengths are fixed or have only

a narrow tuning range. In contrast, liquid crystal lasers can be made very small and highly tunable. "Their wavelengths can be tuned from deep ultraviolet to near-infrared," says Morris.

Because of these benefits, there is a real potential for these lasers to become a truly disruptive technology, dislodging existing lasers and creating new applications, spanning from laser projectors and sensors to new forms of flat-screen displays and multi-purpose medical scanners.

"In their simplest form, lasers have two mirrors and light bounces back and forth between them," explains Peter Palffy-Muhoray, associate director at the Liquid Crystals Institute at Kent State University in Ohio, USA. The distance between these reflectors defines the optical cavity that ultimately determines the wavelength of light emitted by the laser. As can be imagined, operation of the laser is very sensitive to the positioning of the mirrors.

In the case of liquid crystal lasers, the optical cavity is defined by the pitch — the length of one complete twist — of the crystals, and no mirror is needed, says Palffy-Muhoray. "Normally we have to make lasers very precisely but here the biggest advantage is the liquid crystals do it for us. All we have to do is to pump the liquid and we're ready to go," he says.

Moreover, it is easy to control the length, or the pitch, of the crystals chemically, mechanically or electrically, says Morris. "It's like a spring," he adds. The length can be made longer or shorter and by doing so the wavelength of the laser light emitted can be easily controlled.

Unusual as this approach may sound, the idea is in fact far from new, with some of the earliest patents in the area dating back as far as 1973. Later theoretical forays were made by the likes of Eli Yablonovitch at the University of California in Los Angeles, and Sajeev John at the University of Toronto in Canada, both of whom independently predicted in 1987 that lasing was possible from these kinds of materials. Both realized that spontaneous emission could be inhibited within the photonic bandgap of liquid crystals.
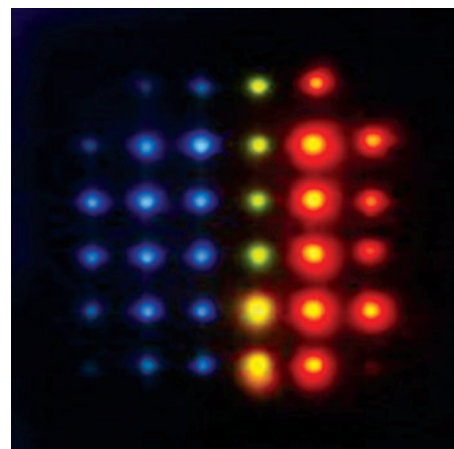
Figure 2 | Image of laser emission from the gradient-pitch liquid crystal laser cell illustrating simultaneously occurring polychromatic laser emission. The cell is filled with two different liquid crystal and dye mixtures from opposite sides.

Early experiments also showed that under certain circumstances liquid crystals could show extraordinary gain. "However, they couldn't show that it was lasing," says Palffy-Muhoray. It took another 12 years before Azriel Genack and Victor Kopp at Queen's College of the City University of New York, USA, were able to give the first unequivocal evidence for band-edge lasing.

The remarkable property that makes liquid crystals attractive for lasing materials is their capability of self-organizing themselves into photonic bandgap structures, according to both Morris and Palffy-Muhoray. "You could literally paint walls with something that could emit laser radiation perpendicular to the wall," says Palffy-Muhoray.

Indeed, for one of the potential applications this is precisely the plan—to create self-organizing thin films for flat-panel displays. "The potential for display applications is large," says Hideo Takezoe, another pioneer in the field from the Tokyo Institute of Technology in Japan. Using this approach, he says, laser displays with multi-cholesteric liquid crystals in hybrid structures containing dyes (see Fig. 1) could be produced at very low cost. The use of liquid crystal lasers could potentially improve the colour quality of displays because the
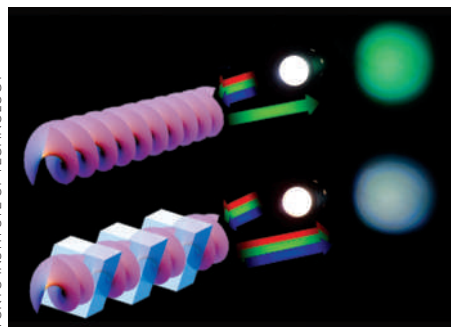
Figure 1 | Image of red–green–blue reflection by a hybrid dye liquid crystal structure.

© 2007 JSAP
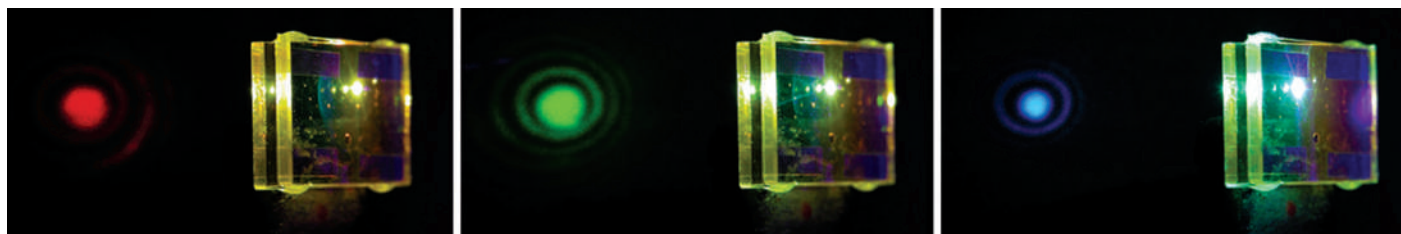
Figure 3 | Tunable laser action. Laser action tunable in the whole visible region can be achieved by laterally moving the cholesteric liquid crystal cell with respect to the position of a pumping beam. These figures show red–green–blue lasing by the excitation of three laterally shifted positions.

pitch of these liquid crystals, and thus their light-emitting wavelengths, can be very precisely controlled.

In fact, both the Cambridge group and Takezoe's team have shown that it is possible to create a cell of liquid crystals whose pitch follows a gradient depending on where they are, as shown in Figs 2 and 3. In particular, Takezoe's demonstration shows that under the excitation of blue light pulses (420 nm, pumping energy of 1.9 mJ per pulse) the various dye formulations throughout the cell will simultaneously emit monochromatic red, green and blue (RGB) light at wavelengths of 620, 550 and 475 nm, as can be seen from Fig. 3. This capability would provide more natural and continuous colours in displays, says Takezoe.

Besides displays, the potential for medical applications is also vast, says Morris. Generally, in such applications many different types of laser are needed because different treatments require different wavelengths. "The advantage offered by liquid crystal lasers is its capability of creating multi-purpose lasers that can be used for many treatments ranged from dermatology to cancer and diabetes detection," says Morris. Also, given their compact size, they could even be used for lab-on-a-chip applications, hints Morris.

Liquid crystal lasers can also be extremely useful as a form of sensor, says Palffy-Muhoray. "They are very responsive to almost any kind of stimuli, such as temperature changes and even slight mechanical stress," he says. The particular factor that makes liquid crystal

lasers attractive as sensors is that the environmental changes are represented as a change in frequency of the light emitted rather than signal strength, he explains. "It's much easier to detect changes in frequency than changes in amplitude," he emphasizes. Although commercial applications of liquid crystals are still a way off, Palffy-Muhoray holds the opinion that the first applications are likely to be sensors of this kind.

Another peculiar property of these materials is that they can be elastomerized to make themselves sensitive to mechanical stresses. Palffy-Muhoray and his co-workers demonstrated this rather spectacularly by showing how a dye-doped cholesteric liquid single-crystal elastomer can be reversibly stretched to produce direct changes in the wavelength of light emitted, as shown in Fig. 4. More specifically, his team showed that a pump beam with 35 ps pulses at a wavelength of 532 nm generated from a frequency-doubled mode-locked Nd:YAG laser could produce lasing from the liquid crystals over the range of 544–630 nm with linewidths of ~3.5 Å. The reported pump threshold for non-deformed samples with a thickness of 0.25 mm was ~280 μJ.

Despite their potential benefits, there is a consensus that these lasers still have some way to go before they will become commercially available. "It's not at the practical stage yet," says Takezoe. "Nobody has created a continuous-wave laser yet."

Morris confirms that the demonstration of a continuous-wave liquid-crystal laser is now one of the next challenges. Only picosecond

pulsing of up to 20 pulses a second has been demonstrated, he says. Typical output energies range from hundreds of nanojoules per pulse up to 10 μJ per pulse, and slope efficiencies are in the range of 1–30%. "The main limiting factor for continuous–wave lasing is related to the light emitter that is doped into the liquid crystal," he says. "These are typically laser dyes which are not suitable for continuous-wave operation owing to photobleaching and other effects." In conventional dye lasers, this is circumvented by keeping the dye flowing and effectively 'flushing' out the energy.

Another challenge that needs to be overcome is to find a way to lower the excitation threshold for lasing, says Palffy-Muhoray. "Theoretically you could make it as low as you want, but achieving this in practice is a whole different ball game and requires a deeper level of understanding of the lasing mechanisms," he adds.

"The goal is to remove the need for an additional excitation source," says Morris. However, this can only be done if the threshold is made low enough whereby the additional source can be replaced with something like a flash lamp or, even better, a light-emitting polymer, he says.

Ironically, the company that was established to try to commercialize this research, Chiral Photonics, set up by Genack and Kopp in 1999, became sidetracked over the following decade. Despite having a head start in this field, the aim of the firm became distracted by another idea, say Genack. "It morphed into something else," he says. "We tried to pursue it for a while, and hope to eventually return to it."

If so, they may not want to leave it too long. Although there are still no commercial products in the market, the field is gathering momentum and it seems that it is only a matter of time before ultra-cheap liquid crystal lasers are being assembled *en masse* for displays, medical diagnostics and new types of sensor. ❒

Duncan Graham-Rowe is a freelance science and technology journalist based in Brighton, UK. e-mail: duncangr@gmail.com

© 2001 WILEY-VCH
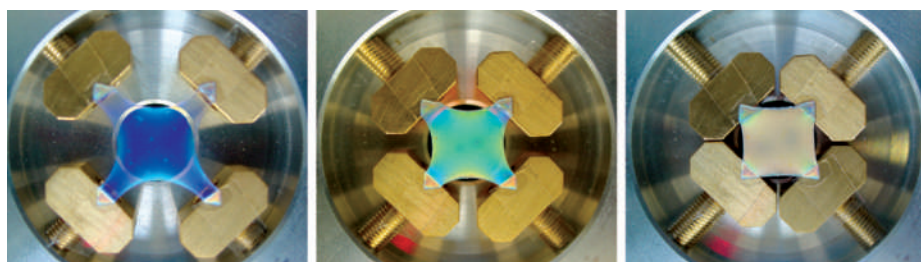
Figure 4 | Changing appearance of a sample of cholesteric liquid single-crystal elastomer under white-light illumination as a function of mechanical strain.

research highlights

NANOPHOTONICS
Scattered away
Nano Lett. ASAP Article
doi:10.1021/nl802580r (2009)
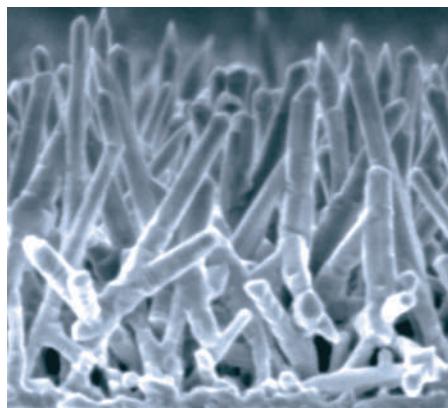
Optical scattering is important not just from a technological point of view, but also because it lies at the heart of striking fundamental effects such as random lasers and the Anderson localization of light (where multiple scattering in random media prevents the diffusion of waves). Otto Muskens and colleagues in the Netherlands have now studied light trapping and Anderson localization effects in nanowire arrays and concluded that once optimized they offer one of the most strongly scattering materials yet created.

Muskens *et al.* chose gallium phosphide (GaP) nanowires as their testbed because the bandgap of GaP, 548 nm, is relatively wide, making it easier for the effects of multiple scattering to be unambiguously identified and distinguished from those of light absorption. The researchers investigated how the diameter of the wires, their volume fractions and their alignment on the substrate affected their scattering. As the nanowire diameter increased, the mean free path of light decreased, reaching a minimum of 0.16 μm. This is shorter than that of the most strongly scattering titanium dioxide powders and is comparable to that of porous GaP networking materials, two of the strongest scatterers in existence. From a practical aspect, the findings could help improve light trapping in solar cells.

DIFFRACTION
In focus
Phys. Rev. Lett. **102,** 043601 (2009)

The phenomenon of diffraction, which causes waves to spread out and diverge as they propagate, is often troublesome. In recent times, researchers have used electromagnetically induced transparency (in which a signal field propagates through an atomic medium with a slower group velocity in the presence of a second control field) to reduce or eliminate the diffraction spreading of beam-like fields. Israeli scientists have now proposed an interesting new way to eliminate diffraction in arbitrary images imprinted on slow light, preserving both the intensity and phase information throughout.

The approach presented by Ofer Firstenberg *et al.* is unique because it uses moving atoms and the associated Doppler effect to correct the path of diverging light. Their scheme makes use of a strong plane-wave control beam, a uniform atomic vapour and a weak signal. As a result of the Doppler effect, any deviations of the control and signal beams from collinear propagation lead to a so-called two-photon detuning effect. By adjusting the relative frequency of the two light fields, this detuning can be tweaked so that the slowly propagating signal pulse is 'pulled' back to the central region, preserving the spatial profile of the field and completely eliminating beam spreading. The technique could be used in high-resolution imaging, image storage and nonlinear optics.

QUANTUM OPTICS
All aboard the quantum train
Science **323,** 486–489 (2009)

Quantum states can be transferred from one system to another through the process of quantum teleportation. However, to perform this feat, scientists must first establish entanglement between the two systems and use only classical communication during the transmission. Now, Steven Olmschenk and his colleagues have reported the first successful transfer of a quantum bit of information, or qubit, between two distant ytterbium ions spaced one metre apart.

Olmschenk and co-workers use microwave and ultrafast laser pulses and a beamsplitter to perform the entanglement. The energy of the photons emitted by each of the ytterbium ions during photonic excitation becomes entangled with the original atomic state. Using a technique known as entanglement swapping, this atom–photon entanglement can be transferred to the other system. The outcome is that measuring the state of one of the ions (which destroys the entanglement) yields a qubit (a 0 or 1), and the information of this measurement result is 'teleported' to the other ion.

The fidelity of the process is 90% but the entanglement efficiency — 1 out of 100 million — is still too low to be useful for a practical scheme. Nevertheless, the ability to teleport quantum states of stationary, massive particles over macroscopic distances is an important first, because atoms are ultimately much better suited as quantum memory banks than photons.

MEDICAL OPTICS
Therapeutic light
Opt. Lett. **34,** 232–234 (2009)

New Swedish research could help to improve light-based cancer treatment schemes. Johan Axelsson and co-workers have demonstrated a way to map the distribution of a photosensitizer — a light-activated chemical that is central to photodynamic therapy — inside the prostate gland.

In interstitial photodynamic therapy (IPDT), optical fibres are implanted into cancerous tissue. The light that they deliver excites a photosensitizer which has been previously administered to the patient, resulting in the generation of radicals such

SINGLE-PHOTON SOURCES
Nanowire funnels
Opt. Express **17,** 2095–2110 (2009)

Solid-state single-photon sources are in great demand in the fields of quantum communication and information processing. They typically consist of a quantum dot as the photon emitter, buried inside a semiconductor microcavity. But even after a decade of intense research, scientists do not have a source that uses a nano-sized resonator and offers extraction efficiencies close to unity.

French researchers have now investigated several designs for single-photon sources that are based on the emission of a quantum dot inside a gallium arsenide nanowire. Through suitable tapering, the nanowire's ends can be made to form efficient metallic–dielectric mirrors that redirect photons towards the substrate, and the divergence of the far-field radiation can be reduced. With careful choice of geometry, the nanowires can act as nano-antennas with a volume of just $0.05\lambda^3$ (λ being the wavelength) that help to funnel the emitted photons into a single-mode channel. Calculations suggest that very high efficiencies, exceeding 90%, should be attainable using collection optics with a numerical aperture of 0.85. In contrast to optical nano-antennas based on plasmonic physics, this approach does not rely on resonance effects and is compatible with a broad spectral range (70 nm at a wavelength of 950 nm).

as singlet-state oxygen molecules that kill local cells, and thus the tumour. The success of IPDT depends on careful optimization of the distributions of light, photosensitizer and tissue oxygenation. However, it is difficult to obtain knowledge of the photosensitizer distribution.

Using data collected from clinical trials and optical phantoms, Axelsson *et al.* devised an algorithm that successfully reconstructs the spatial distribution of a fluorescent photosensitizer. A total of 18 optical fibres, which are coupled through a fibre switch to 18 diode lasers, are used to perform photodynamic therapy, and are arranged so as to maximize the light dose within the prostate while surrounding tissues are spared.

TERAHERTZ TRIALS
The Great Pyramids of silicon
Appl. Phys. Lett. **94,** 041106 (2009)
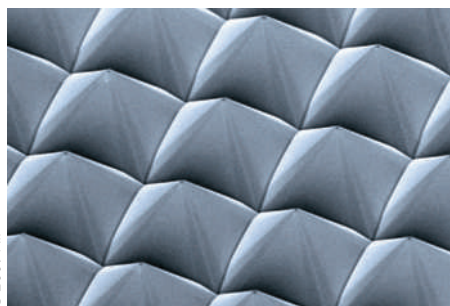
© 2009 AIP

Researchers in New York have found that etching tiny pyramidal structures into the surface of silicon can significantly improve the transmission of terahertz waves. When silicon is covered with micropyramids, the researchers found it to be 89% less reflective over a broad range of terahertz frequencies.

Silicon, in particular high-resistivity silicon, is widely used in terahertz components because it is transparent from the microwave to the infrared. But silicon also tends to be very reflective at an air interface, and as much as 30% of the incoming terahertz power is lost from a single surface. By improving impedance matching, these reflection losses can be mitigated. Chen *et al.* use crystallographic wet etching to create an array of sub-wavelength pyramids on one side of a silicon substrate. The pyramids have apex angles of 72° and base lengths ranging from 110 to 30 μm.

Using pyramids with a 60-μm period, the team finds that reflections are reduced by a maximum value of up to 89% for frequencies ranging from 0.2 to 3.2 THz. This enhanced transmission band can be further increased by tuning the base length of the pyramid. Optimization of the pyramid design should allow further improvements to be made in the anti-reflectivity properties.

SLOW LIGHT
With a view to a chip
Phys. Rev. Lett. **102,** 056801 (2009)

The past few years have witnessed breakthroughs in our ability to slow down and stop light, in media ranging from photonic crystals to optical fibres and metamaterials. In 2007, scientists showed how terahertz light could be brought to a halt in metamaterials while being separated into its constituent colours, producing a 'trapped rainbow'. Qiaoqiang Gan and collaborators now offer a prescription for how to achieve the rainbow trapping of light in the telecommunication wavelength regime, which is of greater practical importance.

Using finite-difference time domain calculations and nanometre-scale metal gratings, they show how the dispersion properties can be tailored such that the cut-off frequency falls within the telecoms region. The team uses graded structures (with a graded grating depth) to gradually couple light into surface plasmon polariton modes with a very low group velocity. As the grating depth changes, the cut-off frequency varies, and incoming waves at different frequencies are trapped at different positions, leading to the trapped rainbow effect. The next step will be to back up these feasibility studies with real experiments.

BIO-IMAGING
In the iPALM of your hand
Proc. Natl Acad. Sci. USA
doi:10.1073/pnas.0813131106 (2009)

Scientists in the United States have developed a microscopy technique that can take three-dimensional pictures of proteins and other structures with a resolution of better than 20 nm. The method — interferometric photoactivated localization microscopy (iPALM) — will shed light on how nanometre-scale biomolecules are organized into micrometre-scale structures in cells.

The power of iPALM stems from its ability to combine the resolution of a single-photon, multiphase interferometric scheme with the molecular specificity offered by PALM. At the heart of this is the concept that fluorescent molecules such as proteins are intrinsic quantum sources. Thanks to wave–particle duality, this means that an emitted photon can simultaneously travel along two optical paths, which can be recombined so that the photon interferes with itself.

The iPALM collects the fluorescent photon into an upper and lower objective lens and passes that wavefront through a three-way beamsplitter. If the fluorescent molecule is centred between the two objectives when the wavefront passes through, no interference is seen. If the molecule is located off-centre, the reunited wavefront will interfere with itself, which can be detected as a change in intensity. Researchers can pinpoint the location of a fluorescent molecule to 10–20 nm, which is the same resolution as that offered by electron microscopy.

ASTRONOMY
Eye on the prize
Opt. Express **17,** 1925–1934 (2009)
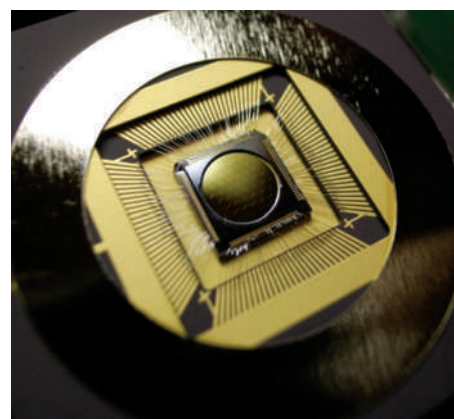
© 2009 OSA

Are there Earth-like planets out there? This is one of the burning questions facing astrophysicists today, but is difficult to answer because of the challenge of observing faint, distant planets against their parent stars. Scientists in France and Australia have proposed a new instrument that uses optical fibres to alter the pupil geometry of a telescope and improve its eye for extrasolar planets.

Telescope pupils are not well suited for high dynamical range imaging. But the single-mode fibres that Kotani *et al.* discuss are perfect spatial filters; any light injected into them emerges as a Gaussian beam with a coherent, flat wavefront. When separate beams filtered in this way are allowed to interfere, the combination is uncorrupted by phase corrugations. As a result, speckle noise, one of the main sources of loss and noise when studying faint planetary candidates, is eliminated.

The authors use this approach to retrieve the image of a simulated binary star. Laser beams injected into 5-μm pinholes generate the binary star light, and a microlens array divides the input pupil into 36 sub-apertures. Each beam is focused onto the core of an individual fibre, and the reconstructed image successfully shows two point-like sources (the binary star). Fringe visibilities are measured with an accuracy of 2%.

DATA STORAGE

Heat-assisted magnetic recording

By using light to assist the recording process, hard disk drive capacity could potentially be increased by two orders of magnitude. The idea is to heat the magnetic medium locally, thus temporarily lowering its resistance to magnetic polarization.

Liang Pan and David B. Bogy

In 1878 Oberlin Smith introduced to the world the idea of magnetically storing the electrical signals produced by the telephone on a steel wire. More than 130 years later, and after moving from wires on drums recording analogue signals to disks capable of storing digital data, magnetic recording has firmly established itself as the dominant computer data storage technique. The current device of choice is the hard disk drive (HDD).

Modern HDDs use read and write transducers positioned by air bearings a few nanometres above a disk (made from a magnetic medium and rotating at a linear speed of tens of metres per second) to access the data. Figure 1a shows an illustration of the standard perpendicular recording scheme in a HDD where the transducers are located at the vertical trailing end of the scanning head.

The areal recording density of HDDs has been doubling roughly every two years. Various technology innovations and breakthroughs, including thin-film technology, giant magnetoresistance (GMR) heads and the use of perpendicular recording in place of longitudinal recording, have helped to maintain this trend.

Today, the areal recording density of HDDs based on perpendicular recording technology has exceeded 200 gigabits (Gb) per square inch. This corresponds to a data-bit size of less than 150 nm in width and 25 nm in length. But perpendicular recording is only a short-term solution; its ultimate areal density is expected to be limited to about 1 Tb in^{-2}. At this density, conventional magnetic recording will hit the superparamagnetic limit where the ambient thermal energy and neighbouring bit polarizations are able to change the direction of the magnetic moment for a single bit. Many solutions have been proposed for further increases in areal recording density, but two of the most promising are heat-assisted magnetic recording (HAMR) and the use of bit patterned media (BPM). Although there are debates about which approach will eventually succeed,
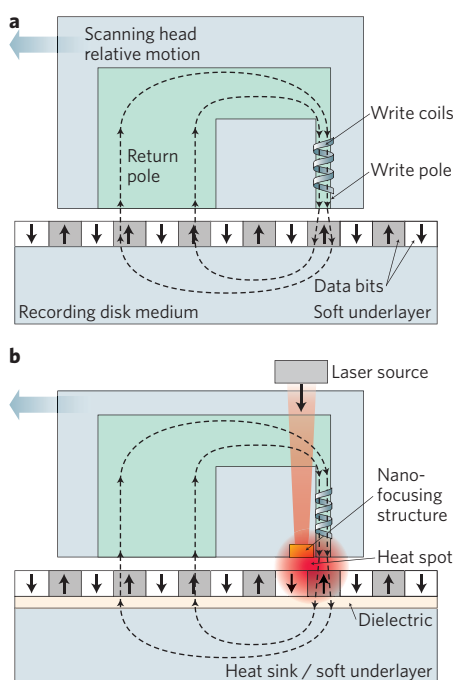
Figure 1 | Schematic of perpendicular recording HDD and heat-assisted magnetic recording (HAMR) systems. **a**, In a conventional HDD, a perpendicular recording head works above a disk medium where the data are stored as vertical magnetized bits. The write transducer, consisting of write coils, a write pole and a return pole, is at the vertical trailing end of the scanning head. **b**, A HAMR head recording to a disk medium with high thermal stability. A laser is used to heat the medium locally in order to assist the recording process by temporarily lowering its resistance to magnetic polarization.

it is likely that some combination of the two approaches will ultimately lead to recording densities of 300 Tb in^{-2} (ref. 1).

Both HAMR and BPM have pros and cons. For example, the recording medium for HAMR has better thermal stability and higher resistance to changing magnetic polarization. Therefore it can retain a much higher recording density at room temperature, but on the other hand,

at this temperature, it also requires a much higher recording magnetic field, which is beyond the capability of thin-film recording transducers like those used in currently available HDDs. HAMR uses laser radiation to heat the recording area of the medium momentarily and thus reduce its polarization resistance below that of the magnetic field emitted from the recording head (Fig. 1b).

In contrast, BPM attempts to overcome the thermal stability problem by replacing the current continuous medium with well-defined single-domain magnetic islands for individual bits. Nanoimprinting provides a potentially low-cost method of media fabrication, but the major challenge still to be met is to fabricate a master mould with the smallest possible bit size to achieve a high areal density. The development of advanced nanolithography technologies is required for the realization of BPM.

The idea of using laser light to assist magnetic recording, as in HAMR, is not new to the data storage industry. In fact it has been used for over 10 years in magneto-optical drives, which can record at a bit size as small as 150 nm with the aid of a hot spot generated by an infrared laser beam focused to a small spot by a high-numerical-aperture lens. The density of data achievable for magneto-optical drives can be improved by using shorter-wavelength laser sources or solid immersion lenses. However, these diffraction-based methods are ultimately limited to laser beam spot sizes of the order of half the wavelength of light. By using a solid immersion lens with high-index oils, the wavelength can be shrunk to about a quarter of the vacuum wavelength. To achieve a density of 1 Tb in^{-2}, however, the laser beam needs to be focused down to a size of about 25 nm, which is substantially beyond the capability of conventional optics.

On page 220 of this issue, Bill Challener and colleagues from the hard disk manufacturer Seagate disclose[2] results from their first-generation HAMR head, which makes use of surface plasmons to allow focusing of a light beam below the

diffraction limit. Surface plasmons are collective oscillations of electrons that are coupled to light and propagate along an interface between a dielectric and a metal. They are strongly localized to the surface interface and exponentially decay in amplitude away from it.

An attraction of surface plasmons is that they can have wavenumbers much larger than those of conventional electromagnetic waves. With careful design of the metallic structures, this means that optical energy can be delivered to a size below the diffraction limit[3–5]. Surface plasmons can produce field intensities in the near field that are orders of magnitude higher than in the incident light. To take advantage of this fact for application to devices, precise control of gaps is often required because this higher field decays exponentially with distance from the metal surface. Fortunately, the gap between the transducers and recording medium in hard disk drives is very small and well regulated using advanced air-bearing surface designs, which makes surface plasmon structures — offering enhanced and sub-diffraction-limit fields — a perfect match for HAMR.

Recently, a plasmonic transducer for subwavelength focusing of light for nanolithography was reported[6] in the form of an aperture surrounded by a metallic grating. It allowed experimental writing of an 80-nm-wide line recorded at a linear speed of 10 m s^{-1}. Although it is hoped this technique can be improved to a linewidth of 20 nm, it is unfortunately not practical for HAMR because the transducer is incompatible with the thin-film head manufacturing process and may not operate well in the presence of a metallic recording film[7].

Challener et al. have now designed a near-field transducer (NFT) that uses surface plasmons and is specifically intended for use with HAMR. The NFT has a lollipop

shape consisting of a small disk and a thin peg made of gold. During the recording process, the NFT is used to excite surface plasmons resonantly. A longitudinal incident field to excite the plasmons is obtained by using a parabolic-shaped thin-film waveguide, called a planar solid immersion mirror, and two sets of diffraction gratings to couple the free-space laser beam into the mirror. The resultant field is predominantly of a particular (longitudinal) polarization, which is advantageous when a metallic recording medium is placed near to the NFT. This is because the NFT's peg creates image charges in the medium that greatly assist the energy transfer through strongly coupled dipole interactions. Unlike many other surface plasmon structures considered previously, the NFT has a strongly localized interaction with the metallic recording medium, and up to 8% of the optical energy is coupled to the recording medium. More importantly for real-world applications, this NFT is compatible with current mass manufacturing techniques for thin-film heads.

Although the 70-nm-wide recording tracks generated by this first-generation HAMR head only correspond to an areal recording density of 200 Gb in^{-2}, which is less than the current state of the art, it has the potential to be extended to much higher densities, possibly as high as 300 Tbit in^{-2}, in the future.

Despite the exciting potential of HAMR, many practical issues still need to be explored before it is ready for commercial deployment. The HAMR process requires local temperature rises in the magnetic medium of 300 K or even higher, so thermal management is an important issue that needs to be tackled. On the recording head side, although up to 8% of the optical energy can be delivered to the recording medium in the current design, much of the energy is

lost to heating the local structure and could result in head deformation and component failure after repeated heating cycles. More efficient heat sink designs and better NFT coupling efficiency are needed for reliability and power conservation.

Regarding the recording medium, its deformation due to momentary heating cycles and thermal damage or depletion of the disk lubricant could cause serious drive failures. Materials suitable for the higher thermal loads, including the invention of new disk lubricants, are also critically important. Furthermore, owing to the evanescent nature of near-field waves, the transducer's coupling efficiency depends exponentially on the gap size between the NFT and the recording medium. This will require dedicated gap regulation techniques, which could be very challenging when the head-to-medium gap reduces to a few nanometres, as may be the case when recording at even higher areal densities.

Despite the challenges, the future for heat-assisted magnetic recording is now promising. Challener and colleagues' work — the first device-level HAMR demonstration — should spur on future research to overcome the remaining hurdles. ❐

Liang Pan and David B. Bogy are at the Computer Mechanics Laboratory, Department of Mechanical Engineering, University of California, 5146 Etcheverry Hall, Berkeley, California 94720, USA.
e-mail: lpan@berkeley.edu;
dbogy@cml.me.berkeley.edu

References
1. Mcdaniel, T. W. J. Phys. Condens. Matter. 17, R315 (2005).
2. Challener, W. A. Nature Photon. 3, 220–224 (2009).
3. Stockman, M. I. Phys. Rev. Lett. 93, 137404 (2004).
4. Zhang, X. & Liu, Z. Nature Mater. 7, 435–441 (2008).
5. Conway, J. A. Efficient Optical Coupling to the Nanoscale. PhD thesis, Univ. California, Los Angeles (2006).
6. Srituravanich, W. et al. Nature Nanotech. 3, 733 (2008).
7. Kryder, M. H. et al. Proc. IEEE 96, 1810 (2008).

NONLINEAR OPTICS

Silicon gets the green light

Third-harmonic generation enhanced by slow-light pulses in a photonic crystal waveguide offers a way to generate green light emission from silicon.

Toshihiko Baba

In recent years silicon photonics has gone from strength to strength, with a continual stream of developments in the optical functionality of silicon chips. The ability to slow light in silicon devices looks set to offer still more useful nonlinear optical

effects. An example of one such opportunity, the generation of green light in silicon by nonlinear optics, is presented in this issue. On page 206, Bill Corcoran and co-workers from the University of Sydney, Australia, and the University of St Andrews, UK,

report the emission of green light from a silicon photonic crystal waveguide[1]. The green emission originates from nonlinear third-harmonic generation enhanced by slow-propagating pump pulses of near-infrared light (see Fig. 1). The finding not

only shows that silicon can be used as an emitter of green light but also suggests a new nonlinear function in CMOS-compatible silicon waveguides.

In fact, green laser light is commonly generated by optical nonlinear wavelength conversion, albeit in nonlinear crystals carefully designed for the task. For example, second-harmonic generation from short pump pulses at a near-infrared wavelength of 1.0–1.1 µm is used to create green laser pointers. And full-colour visible emission containing green light has been observed through supercontinuum generation in silica fibres with femtosecond pulse pumping. In recent years, mode-locked pulsed lasers based on erbium-doped fibre amplifiers have also been widely used as practical light sources for ultrashort pulses at wavelengths ranging from 1.53 to 1.56 µm. Simple nonlinear emission of green light is therefore becoming readily available.

The work carried out by Corcoran *et al.* makes use of slow light to increase the nonlinear effect present in silicon photonic-crystal waveguides. A photonic crystal is an artificial mosaic nanostructure that has a multidimensional periodicity on the optical wavelength scale[2]. In recent years, a thin membrane featuring a two-dimensional air-hole array — a photonic crystal slab — has become a useful platform for functional photonic devices, such as micro- and nano-lasers, ultra-compact waveguide components and negative refractive optics.

The photonic crystal waveguide is formed by introducing a line defect consisting of missing air-holes into the photonic crystal slab. The waveguide's light transmission window is dictated by the slab's photonic bands, which in turn are determined by the geometry of the photonic lattice. Transmission usually lies around a wavelength that is roughly four periods of the photonic lattice. Light with a wavelength shorter than two periods is strongly diffracted and completely radiated out to free space. This behaviour is in stark contrast to conventional waveguides, in which shorter-wavelength light is confined more strongly in the waveguide. Another unique characteristic of the photonic crystal waveguide is the generation of slow light with a greatly reduced group velocity.

The generation of slow light by various systems is being driven by the desire to produce optical buffers and strong light–matter interactions[3]. Fundamentally, the slowing occurs because of an optical resonance with electrons or structures. A benefit of the photonic crystal waveguide approach is that it suits integration on a chip and operates at room temperature. Because the low group velocity also implies spatial
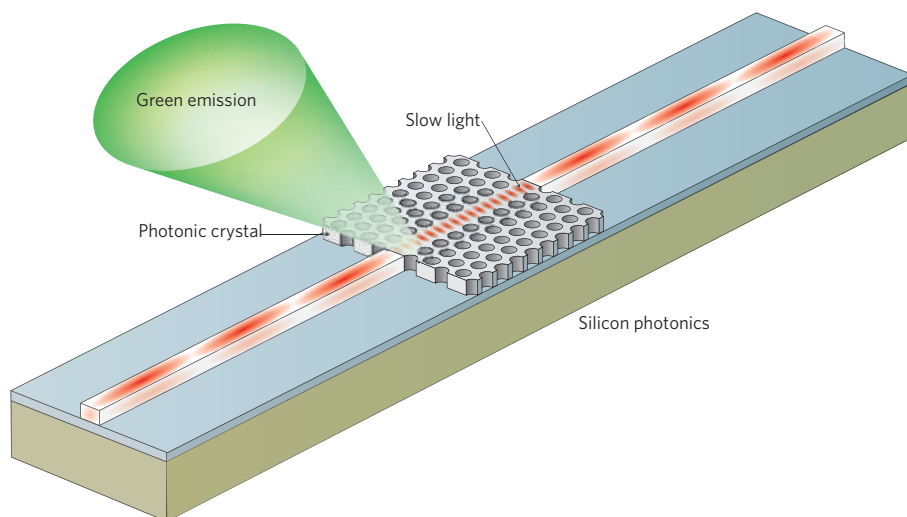
Figure 1 | Green light emission from a silicon photonic-crystal waveguide by slow-light-enhanced third-harmonic generation.

compression of the optical energy, the light intensity is increased and the interaction time with the material of the structure is prolonged in inverse proportion to the group velocity, resulting in more efficient optical nonlinear effects.

With this in mind, slow-propagating ultrashort optical pulses with high peak intensity are considered to be the most beneficial for enhancing nonlinear effects. Until recently, however, this was difficult to achieve because of the limited frequency bandwidth and strong higher-order dispersion usually associated with slow light. Several approaches have been tried to overcome these difficulties, and one of them is band engineering of the photonic-crystal waveguide. Fine tuning of the photonic-crystal structure deforms the shape of photonic bands, and an optimum structure shows a straight photonic band, which provides a low group velocity as well as a moderate bandwidth and zero dispersion suitable for ultrashort pulse transmission. It is now possible to generate experimentally picosecond- to femtosecond-wide pulses that propagate with a speed a hundred times lower than the speed of light in vacuum.

As silicon is stable against mechanical, optical and thermal stresses, it is best suited as the material for the thin membrane of a photonic-crystal slab. Silicon can sustain heating caused by nonlinear losses, such as two-photon absorption and free-carrier absorption, induced by the high peak intensity of the slow light.

Usually, green light is strongly absorbed in silicon. In the experiment by Corcoran *et al.*, however, the photonic lattice allows the green light to escape rapidly to free space. For efficient harmonic

generation, phase matching of the pump wave and harmonic waves is essential to maximize the spatial overlap of these two waves. But this requirement is relaxed in the photonic-crystal waveguide, because the phase mismatch is compensated by the phase shift due to the photonic lattice. In addition, the mismatch might be eliminated altogether by the quick escape of green light to free space (the nearly vertical green emission in the experiment suggests that the pump light was converted almost directly to free-space modes with an optimum radiation angle for phase matching).

Corcoran *et al.* show that the slow-light pulse effectively reduces the threshold peak-power level of pump light for green-light generation to 5–10 W, with a time-averaged value of less than 100 µW. This low power level is aided by the waveguide's small effective cross-section of nearly 0.4 µm², which strongly confines and concentrates the pump light. This threshold power level is five to six orders of magnitude lower than for earlier third-harmonic generation in bulk silicon. Nevertheless, the third-harmonic generation still requires much higher light intensity than is needed for second-harmonic generation.

Corcoran *et al.* estimate that the conversion efficiency is 10^{-7}. Although this value is five orders of magnitude higher than that reported in three-dimensional polystyrene photonic crystals, it is still much lower than expected for ideal band-to-band transition. The key to increasing the efficiency is to further increase the internal intensity of the pulse. To do so, first the coupling loss of pump light into the waveguide needs to be reduced. In this experiment, a loss of 10 dB or higher is present because a lensed fibre is

used to couple pump light to the waveguide with very small modal cross-section. If a state-of-the-art spot-size converter were to be used with the waveguide, this loss could be reduced to less than 1 dB. In addition, the slow-light pulse in this experiment was 1.5 ps wide, corresponding to a wavelength bandwidth of 2 nm. If the full bandwidth of 10 nm measured for slow light is fully used to launch a shorter pulse, the peak intensity is five times higher for the same time-averaged power. These two improvements would potentially improve the efficiency by several orders of magnitude, if nonlinear losses were suppressed.

Another direction for future research is to reduce the nonlinear losses, in particular that of free carriers. Silicon has an

absorption-edge wavelength of 1.11 μm, so two-photon absorption is unavoidable for pump wavelengths around 1.55 μm as the absorption occurs with pump wavelengths up to twice the absorption-edge wavelength. However, the free-carrier absorption of excited carriers by two-photon absorption is usually more severe in terms of the absorption itself and the heating induced. It can be avoided by shortening the carrier lifetime to less than the repetition period of the pulses, which is possible by applying an electric field and/or doping non-radiative recombination centres.

Despite the low conversion efficiency, the work by Corcoran et al. is an interesting observation that offers increased functionality and new opportunities for the fields of

photonic crystals, slow light and silicon photonics. Looking ahead, not only third-harmonic generation but also other various types of wavelength conversion, nonlinear all-optical modulation and switching, formation of optical solitons and so on will be areas worth pursuing. ❏

Toshihiko Baba is at the Department of Electrical and Computer Engineering, Yokohama National University, Yokohama 240-8501, Japan.
e-mail: baba@ynu.ac.jp

References

1. Corcoran, B. *et al. Nature Photon.* **3,** 206–210 (2009).
2. Joannopoulos, J. D., Johnson, S. G., Winn, J. N. & Meade, R. D. *Photonic Crystals Molding the Flow of Light* 2nd edn (Princeton Univ. Press, 2008).
3. Baba, T. *Nature Photon.* **2,** 465–473 (2008).

Nanoscale colour detector

By attaching light-absorbing molecules to carbon nanotube field-effect transistors, scientists in the United States have fabricated nanoscale optoelectronic detectors that are sensitive to different colours of visible light (*Nano Lett.* doi:10.1021/nl8032922; 2009).

Xinjian Zhou and colleagues from Sandia National Laboratories took single-walled carbon nanotubes and functionalized them with azobenzene chromophores to create molecularly engineered photosensitive materials. In the scheme, the chromophores serve as photoabsorbers and the nanotubes act as an electronic read-out system.

The carbon nanotubes had diameters in the range of 0.8–2 nm, and were prepared in a well-dispersed solution and attached to treated silicon wafers. Three different azobenzene-based chromophores having absorption maxima at 467 nm, 381 nm and 342 nm, respectively, were anchored, through strong non-covalent interactions, to the surfaces of the nanotubes, in three separate experiments.

On illuminating the nanotubes with monochromatic light with a wavelength in the visible range of 400–700 nm, the scientists observed shifts in the threshold voltage in the electrical conduction of these nanotube–chromophore hybrid field-effect transistors. The shifts correlated with the absorption spectra of the azobenzene molecules.

Zhou *et al.* confirm that the process of conversion from an optical to an electrical signal is controlled by a dipole change

© 2009 ACS
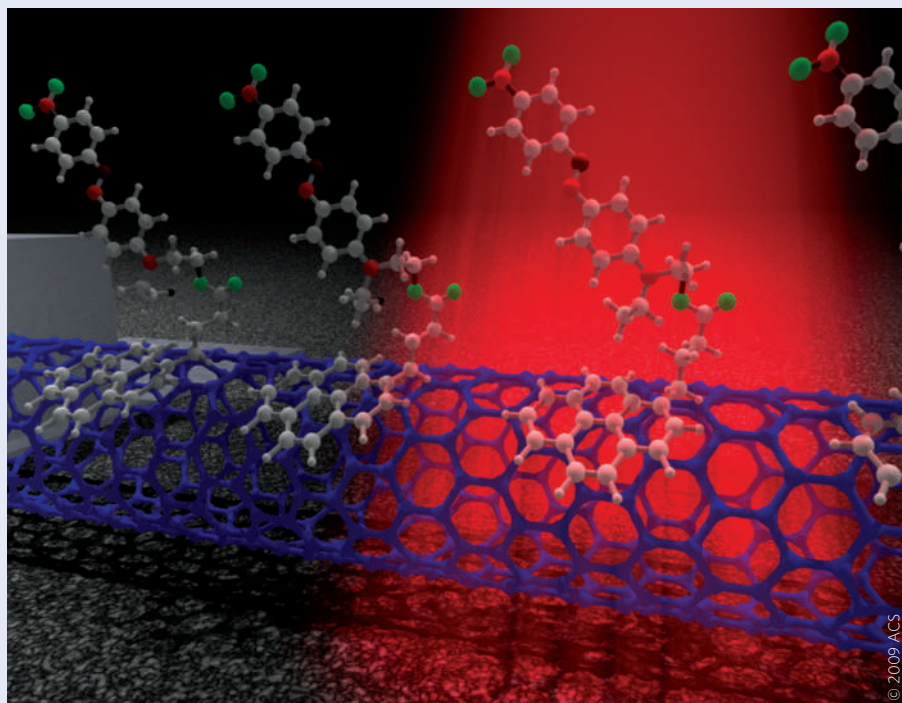
mechanism at the molecular level. When a chromophore absorbs photons, a change in the molecular structure of the azobenzene occurs — so-called photoisomerization — and it transforms from the ground state *trans*-configuration to the metastable excited state *cis*-configuration. This photon-induced isomerization is accompanied by a large change in the electrical dipole moment of the chromophore and modifies the electrostatic potential and thus the threshold voltage of the nanotubes.

Zhou and co-workers' colour detection scheme is not only useful for making colour photodetectors with nanoscale resolution but also gives insights into the molecular interactions between single-walled carbon nanotubes and molecules. Further improvements are expected to allow them to detect single-molecule transformation activities and extend operation to other spectral regions.

RACHEL WON

SILICON PHOTONICS

Slot machine

Ultrafast all-optical computation with silicon photonic devices is still a dream. New research, which combines organic nonlinear polymers with silicon waveguides, is now bringing that dream closer to reality.

Tom Baehr-Jones and Michael Hochberg

All-optical computation has been a goal of the optics community for many years. Today, nearly all data processing occurs in the electronic domain; this is because it is comparatively cheap and easy to create highly nonlinear electronic circuits based on transistors. Because transistors can be printed on a silicon wafer millions at a time, the marginal cost of complexity in electronics is extraordinarily low. But electronic logic has serious limitations: even the fastest transistors rely on changing the local population of carriers using electric fields, and thus far this has limited speeds to around 1 THz.

By contrast, ultrafast optical devices can potentially operate at speeds as high as the optical frequency, in excess of 100 THz. Now, for the first time, it is becoming possible to build printed circuits — in silicon, no less — that offer the tantalizing promise of practical all-optical computing. On page 216 of this issue[1], an intercontinental team of collaborators led by Christian Koos demonstrate all-optical signal processing in a silicon–organic hybrid waveguide at speeds in excess of 100 Gbit s^{-1}. Their work takes advantage of the inherent strengths of both silicon waveguides and advanced, ultrafast organic nonlinear materials, which are directly integrated with these silicon guides. The result is a considerable step towards the goal of all-optical computation.

Koos *et al.* use silicon-on-insulator, which is an extremely versatile platform for integrated optics. In recent years a variety of devices have been demonstrated in this material system, including electro-optic modulators, detectors, all-optical modulators, biosensors and a range of both passive and nonlinear optical devices. The first products to take advantage of the monumental complexity (both optical and electronic) that can be captured on a single silicon chip are just now hitting the market, including a 40-Gbit s^{-1} cable from Luxtera Corporation, which provides electrical input and output at both ends but transmits data optically[2]. This represents a bit rate that is 100 times as fast as the FireWire standard found on most personal computers today.

Silicon provides both a very high index of refraction and low material loss at
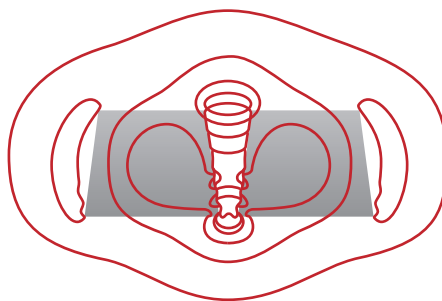
Figure 1 | Slot machine. A contour plot of the horizontal component of the electric field (E_x) in a silicon slot waveguide with an organic cladding, showing that much of the energy is confined in the low-index slot. Note the increased concentration of E_x at the bottom of the trench, where the sloped sidewall results in a narrower gap.

telecommunication wavelengths. Of course, optical circuits fabricated in silicon can also take advantage of an infrastructure that is effectively subsidized by the electronics industry. With proper processing, it is possible to fabricate silicon waveguides with very low losses and couple them to optical fibres. Crucially, waveguides with nanoscale features can be easily constructed. Typical silicon guides have dimensions of around 400 nm × 200 nm, with similar optical mode sizes. For comparison, a single-mode optical fibre for telecommunication wavelengths ($\lambda = 1.55$ μm) usually has a core diameter of about 8 μm.

It turns out that the mode size can be further decreased through the use of a slot waveguide, which is formed by two (or more) strips of silicon or other high-index material in close proximity. It is important to note that a more concentrated optical mode tends to have higher relative nonlinearity, owing to the concentration of optical power. Slot waveguides were first demonstrated by Michal Lipson[3] and colleagues, and their mode-concentrating properties have been used in applications ranging from sensing[4] to modulation[5]. Because the trench is defined lithographically (or, more recently, through deposition), it is possible to create extremely narrow slots; recent work has shown low-loss guides with slots that are only about `10 nm wide[6]. As shown in Fig. 1,

the transverse electric (TE) optical mode (where the electric field is primarily parallel to the plane of the wafer, and orthogonal to the direction of propagation) in a slot waveguide is concentrated in the void region, precisely where it is possible to deposit a cladding material.

The central challenge in achieving all-optical computation has been the fact that optical systems are, for the most part, fairly linear — low nonlinearity and loss are two of the main reasons why optical fibres are such a convenient system for long-distance data communication. To achieve all-optical signal processing in practical devices, we must somehow create nonlinearities that are the dominant effect for even modest powers. This is a considerable challenge; producing large nonlinearities in today's optical systems often requires ultra-high-power pulsed lasers or highly resonant cavities to enhance the nonlinear effects.

Silicon's nonlinear optical properties are well known, and include Raman scattering, two-photon absorption and a relatively weak Kerr effect. These properties are not easy to enhance directly. Furthermore, slow nonlinearities such as free carrier effects have a tendency to swamp the ultrafast effects in silicon guides[7]. Recently, a χ^2 moment has been induced in silicon by breaking the crystal's inversion symmetry using strain[8]. A χ^2 moment corresponds to a material with a dielectric constant that varies linearly in applied field, and the effect can be used to build a number of nonlinear devices, including electro-optic modulators and difference-frequency generators. However, the χ^2 moment achieved in this way is still weak compared with what can be achieved in other nonlinear systems. Because of the overall linearity of silicon, several optical signals with power levels of a milliwatt or more can co-propagate in a nanoscale silicon waveguide with only minimal nonlinear interaction. Although these smaller nonlinearities do present design challenges in some situations, they are not generally strong enough to build practical all-optical computation devices in silicon.

The adoption of nanoscale slot waveguides represents one cornerstone of the work done by Koos *et al.*; the other is the use of organic

nonlinear materials. It turns out that the degree of nonlinearity of these materials (in particular χ^2 nonlinear polymers) has increased exponentially over the past several years, as shown in Fig. 2. This is due to a combination of circumstances, most notably a powerful collaboration among theoretical chemists, synthetic chemists and optical device-oriented groups. Progress has also been seen in χ^3 polymers (a material with a χ^3 moment is characterized by a dielectric constant that has a second-order dependence on the applied electric field, and will therefore show a Kerr coefficient). By using a highly nonlinear χ^3 polymer material called DDMEBT as the cladding for a silicon slot waveguide, Koos et al. are able to surpass the limitations of silicon.

Combining silicon slot and ridge waveguides with organic nonlinear materials is an idea that has been explored for applications ranging from modulation and detection to all-optical signal processing[9]. The work by Koos et al. is, however, the first experimental demonstration in which slot waveguides have been used in conjunction with χ^3 polymers for practical ultrafast signal processing[1]. The silicon–organic hybrid waveguides offer the best of both worlds: they combine the high nonlinearities of organic nonlinear materials with the extraordinary mode field concentrations of silicon waveguides. It is worth noting that these materials can be synthesized and developed with chemical methods in a way that is largely independent of the silicon waveguide system. As a result, progress on new materials could be rapidly incorporated into the device design by simply inserting the latest materials into the device fabrication flow.

Koos and colleagues show that their waveguides can be used to build a system for all-optical signal processing and they demonstrate demultiplexing in particular. Their device consists of a silicon slot waveguide etched into a 220-nm-thick silicon layer. The waveguide and slot are defined using optical lithography, a standard semiconductor fabrication process, and slots 205 nm wide are fabricated in the guides. These devices are coated with the DDMEBT (2-[4-(dimethylamino)phenyl]-3-{[4-(dimethylamino)phenyl] ethynyl}buta-1,3-diene-1,1,4,4-tetracarbonitrile) using a molecular beam deposition technique. Performing the coating in this way promotes the growth of a uniform, amorphous film, minimizing optical losses from scattering.

The experimental set-up for their demultiplexing measurement starts with a 170-Gbit s^{-1} source of randomized bits and a 42.7-Gbit s^{-1} sampler source, which is based on a pair of synchronized mode-locked fibre lasers. By combining the two signals
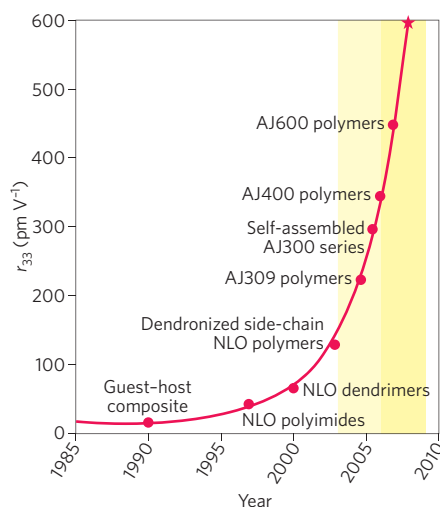
Figure 2 | Nonlinearity of χ^2 organic materials over the past two decades. The r_{33} metric characterizes the nonlinear activity of these polymers. For comparison, lithium niobate has an r_{33} of around 30 pm V^{-1}. AJ600 is a nonlinear polymer synthesized by Alex Jen. Figure courtesy of L. Dalton.

in the slot waveguide through a nonlinear process known as four-wave mixing, and filtering out the input frequencies, the authors are able to show a factor of four demultiplexing of the 170-Gbit s^{-1} signal back to 42.7 Gbit s^{-1}. The results indicate very clean transmission through the waveguide system, demonstrating that the ultrafast nonlinearities, rather than free carrier effects, dominate. (Had free carrier effects been significant, the resulting bandwidth limit would have distorted the output bit patterns.)

The authors characterize nonlinearities in the slot and ridge waveguides to assess the technological benefits of the slot-waveguide geometry. They are able to show, with an elegant measurement of the nonlinear phase dynamics, that the slower nonlinearities (due to two-photon-absorption-induced free carriers) are largely absent in the slot-waveguide geometry. This key observation shows that the new hybrid geometry successfully avoids a significant speed limitation that had been present in silicon integrated optics.

This work represents an important advance in state-of-the-art silicon photonics. It provides the first demonstration that, using slot waveguides to take advantage of very high mode confinement in active cladding materials, it is possible not only to achieve large optical nonlinearity but also to build a practical data communication device. The authors have shown that they can create a highly nonlinear ultrafast system, and then take that system and push bits through it with extraordinary bandwidth and high fidelity.

Silicon photonics offers a platform on which it is possible to scale up system complexity rapidly and to access nanoscale features in production processes. Now it is possible to take advantage of the power of silicon to build practical nonlinear signal-processing devices with bandwidths well in excess of 100 Gbit s^{-1}. The idea of bringing new physics into the silicon system through hybrid materials integration is one that has already provided remarkable results in, for instance, the work by Bowers and colleagues on integrating III/V gain materials in order to make lasers[10]. These results are likely to be only the beginning for the field of hybrid silicon photonics.

We expect that silicon photonic circuits will begin to be used as a 'photonic motherboard', where several different kinds of functionality will be added lithographically, through the integration of different active cladding materials. Over the coming years, we will surely see a proliferation of new devices in the silicon platform made possible by the integration of new materials. For instance, it is reasonable to expect that silicon–polymer systems will provide a vehicle for demonstrating widely tunable optical parametric oscillators, compact high-gain elements, and completely new types of integrated optical sources and detectors. With the ability to integrate high-bandwidth analogue and digital control electronics on-chip, and to tune the nonlinear properties by coupling a variety of different materials to the silicon guides, it will become possible to create tightly controlled, highly stable ultrafast optical systems-on-a-chip. It is reasonable to believe that, in the next few years, all-optical ultrafast transistors will be demonstrated with bandwidths an order of magnitude or greater than can be achieved with electronics alone. Koos and co-workers' paper in this issue is an important milestone on the path towards practical all-optical computers. ❐

Tom Baehr-Jones and Michael Hochberg are at the University of Washington, Seattle, Washington 98195 2500, USA.
e mail: hochberg@washington.edu;
baehrjt@washington.edu

References

1. Koos, C. *et al. Nature Photon*. **3,** 216–219 (2009).
2. http://www.luxtera.com
3. Almeida, V. R., Xu, Q., Barrios, C. A. & Lipson, M. *Opt. Lett.* **29,** 1209–1211 (2004).
4. Barrios, C. A. *et al. Opt. Lett.* **32,** 3080–3082 (2007).
5. Baehr-Jones, T. *et al. Opt. Express* **13,** 5216–5226 (2005).
6. Preston, K. & Lipson, M. *Opt. Express* **17,** 1527–1534 (2009).
7. Dimitropoulos, D., Jhaveri, R., Claps, R., Woo, J. C. S. & Jalali, B. *Appl. Phys. Lett.* **86,** 071115 (2005).
8. Rune, S. *Nature* **441,** 199–202 (2006).
9. Baehr-Jones, T. *et al. J. Phys. Chem. C* **112,** 8085-8090 (2008).
10. Fang, A. W. *et al. Photon. Technol. Lett.* **18,** 1143–1145 (2006).

PHOTOVOLTAICS

Solar-assisted cars

In the same month that Ferrari showed the world that it is going green — with the installation of 1,500 m^2 of solar panels on the rooftop of its production facility in Maranello, Italy, providing 213,985 kW h per year to help power its operations — Toyota revealed that solar panels will adorn the roof of the 2010 model of the Toyota Prius. Meanwhile, after-market manufacturers are providing solar kits for the Prius and other electric–petrol hybrids.

The Prius was launched in Japan in 1997, making it the first mass-produced hybrid vehicle, and was released worldwide in 2001. In May 2008, worldwide sales passed 1,000,000, with more than half of those sales in the United States. The solar panel used by Toyota is reportedly made by Kyocera and is used to power the car's climate control (including the air-conditioning motor), reducing the burden on the battery and petrol motor. The solar cells reportedly supply about 1 kW of power, which is enough to keep things cool, even while the car is parked out in the sunlight with its engine turned off. Additionally, the system

TOYOTA

(which is an optional extra) can be activated remotely from the key fob to start up the air conditioner before you get in the car.

The idea of fitting cars with solar panels is not new, and after-market companies already provide solar kits for various hybrid vehicles including the Prius. For example,

California-based Solar Electric Vehicles (SEV) has offered customized solar panels for the Prius roof since 1994. The panel can generate 215 watts of power and is manufactured from high-efficiency monocrystalline photovoltaic cells. The system, which takes only a few hours to install and has a cost–benefit break-even period of about 2–3 years, ultimately provides about 20 miles per day of electric driving range, resulting in a claimed improvement in fuel efficiency of about 29 per cent (depending on driving habits and conditions). Back in 1984, the founders of SEV actually developed the first car powered exclusively by solar energy with a 1.2-kW solar array, a 1-hp wheel motor and no batteries, which ran at speeds of up to 41 mph.

The new Prius is the first production car whose air conditioning can run on solar power alone. The big question is: will other car manufacturers follow suit, perhaps ultimately resulting in a completely solar-powered production car?

DAVID PILE

IMAGE TRANSMISSION

Looking into a self-distorting world

Imaging through linear media is straightforward, but light beams propagating through nonlinear media become heavily distorted, rendering all usual imaging techniques practically useless. Now, scientists have found a way to recover images transmitted through nonlinear media — by using back-propagation simulations.

Mordechai Segev and Demetrios N. Christodoulides

Light beams, and thus images, passing through nonlinear media are heavily distorted as they propagate because of a complex and dynamic interaction between light and matter. As a result, it is difficult to look through nonlinear media or to extract three-dimensional images from within the media. Is it possible to recover pictorial information transmitted through them? Yes, if information is not lost — radiated away or simply absorbed. Would we be able one day to look through such an environment, which is generically hostile to transmission of structured light beams? Or, better, could we look into such media and

obtain three-dimensional images within the material? Here we describe the issues involved, review the historical evolution of the ideas, discuss the recent success, pose some non-trivial questions, and, we hope, provide some insight into the subject. On page 211 of this issue[1], Jason Fleischer and co-workers at Princeton University demonstrate a computational method of recovering images transmitted through a nonlinear medium. By measuring the output and numerically back-propagating the wave dynamics, they not only show that they can recover the input of two-dimensional spatial beams containing

images, but also reconstruct the light field at intermediate points in the medium.

Nature is inherently nonlinear in its response to beams of light. Take a light beam, launch it through any medium and raise the intensity. At some point the beam will start modifying the properties of the medium, which will, in turn, modify the structure of the beam itself, causing further changes in the medium properties, which again change the beam pattern, in a dynamical fashion. In most material systems, nonlinear optical dynamics can occur by virtue of a variety of physical mechanisms. Examples range from ultrafast
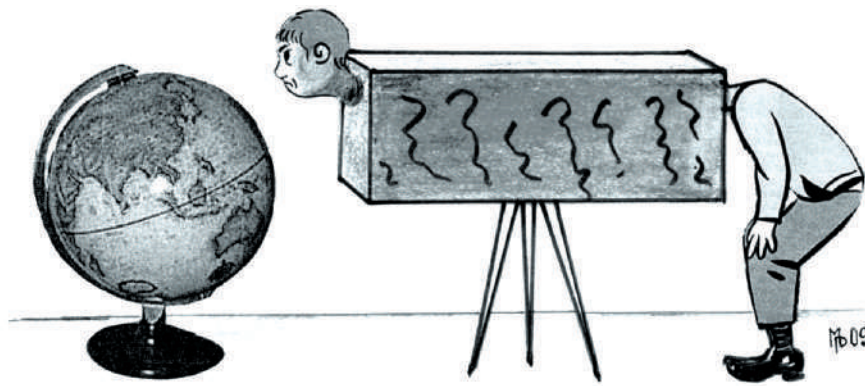
Figure 1 | Princeton scientist peeking through a nonlinear medium.

phenomena such as the optical Kerr effect and two-photon absorption, to fairly slow phenomena such as thermal 'blooming' and photorefractive effects. Some of these nonlinear effects (for example the optical Kerr effect) do not involve loss of optical power, whereas others (such as two-photon absorption) are lossy, causing higher losses in brighter regions with higher light intensity. Some of the effects are local in space, meaning that the change in material properties at any point is a function of the optical field at that point only; others are highly non-local, signifying long-range nonlinear effects. In all such nonlinear media, image-bearing optical beams are greatly distorted when the experimental parameters are deep in the nonlinear regime. For instance, if the medium is of the self-focusing type, brighter spots will become narrower and narrower, and broad regions of high intensity will fragment into pieces. Likewise, nonlinear interactions with noise give rise to a phenomenon known as 'modulation instability', which is essentially the spontaneous formation of patterns — a universal phenomenon that manifests itself very strongly as intricate patterns appear in optical beams. All of these physical mechanisms, and many more, distort optical beams passing through nonlinear media.

The subject of recovering optical information (images) borne on beams propagating in highly nonlinear media has attracted much attention since the early days of the laser, when thermal blooming was found to distort high-power beams. Naturally, one of the ways to avoid signal distortion is simply to reduce the intensity to the level where the medium behaves linearly. However, the truth is that high-intensity light has many advantages and is often desirable: for example, it raises the signal-to-noise ratio in signal propagation. The other argument is that nonlinearities do exist even at low intensities;

they are just weaker. A good measure for identifying cases where nonlinear effects are significant is to calculate the nonlinear phase-shift — the product of vacuum wave number, nonlinear index change and propagation distance. Nonlinear effects become significant when this phase-shift is comparable to π. Hence, if the propagation distance is large enough, nonlinear effects are inevitable even at very low intensities.

Going back to the basic question, is it at all possible to recover optical information borne on beams propagating in highly nonlinear media? Not always. If information is lost, the process becomes irreversible, and one cannot recover the initial data. When the loss is linear, as in simple absorption, information embedded in weak wave components is lost when the intensities of such waves are weaker than the noise from scattering, material imperfections and such like. The problem becomes more severe when loss is nonlinear, for example in two-photon absorption, in which case the loss is greater at brighter spots, and the image will be distorted. Modulational instability is another example of such an irreversible process, as it is 'triggered' from random noise itself. Inherently, reversibility is a prerequisite for complete reconstruction of information. Hence, any process that leads to an irreversible entropy production imposes severe limitations on the ability to reconstruct information.

Historically, the first proposal of a method of transferring pictures through a nonlinear medium was made in 1977 by Yariv[2], who suggested using phase conjugation. A phase-conjugate mirror essentially creates a complete reflection of the optical field, but conjugates the spatial part of the phase. As such, a beam passed through any phase element, be it a simple lens or a complex distortion, then reflected off a phase-conjugate mirror and passed again through the phase element,

would emerge after this round trip with its original information completely restored (provided all elements in the system are reciprocal: no apertures, for example). This idea works well for transmitting pictures through a multimode fibre and/or a reciprocal nonlinear medium without linear or nonlinear loss. Indeed, information retrieval by virtue of phase conjugation was demonstrated by Fischer's team in 1985 (ref. 3). But one could naturally ask: what is this good for, if one must send the information back and forth? Indeed, just for information transmission, the idea, nice as it may be, is of little value. However, using 'passive' (self-pumped) phase-conjugate mirrors in this fashion does provide an excellent system for interferometry and accurate distance sensing through distorting media[3,4]. Likewise, using a phase-conjugate mirror to replace a laser mirror improves the performance of the resonator considerably.

Over the years, there have been several attempts to develop methods for image transmission through nonlinear media. Some ideas have to do with various schemes of forward four-wave mixing[5,6], which are similar to phase conjugation but do not require round-trip propagation. But all these methods offer very limited solutions: either the medium must be 'short' so that the accumulated nonlinear phase shift is small, or the spatial resolution is very limited. Some particular nonlinear systems have been found to be amenable to system-specific solutions, an example being electromagnetically induced transparency[7], albeit thus far with rather limited resolution. But these are all material-specific and cannot solve the general problem of imaging through a nonlinear medium.

In 2001, a more general method was demonstrated, offering a means of transferring images through non-instantaneous nonlinear media[8]. That idea relies on using the image-bearing optical beam to induce a highly multimode incoherent soliton, which contains information related to the image embedded in its modal amplitudes and phases. Alternatively, one can use the multimode waveguide that the soliton induces in the medium, and transmit a weak image-bearing beam through this waveguide, through which the propagation is linear[8]. The idea works, but it requires that the nonlinearity is non-instantaneous (that is, the modal phases fluctuate independently much faster than the response time of the nonlinear medium). As such, this method is not universal. More recently, the transmission of incoherent solitons

in highly non-local yet temporally instantaneous nonlinear media has been demonstrated, and these too can be used to carry pictorial information through nonlinear media[9]. But again, the method is restricted to non-local nonlinearities.

What Fleischer and co-workers demonstrate[1] is a universal method that is not material-specific. It relies on the characterization of the nonlinear medium (form of nonlinearity, parameters, propagation distance and so forth), detection of the amplitude and phase of the light emerging from it, and subsequently simulation of the back-propagated light in the medium and retrieval of the input information. They record the amplitude of the light field containing image information using a CCD (charge-coupled device) and capture the phase based on interference (holographic) measurement. Light propagation is described by the nonlinear (Schrödinger-like) wave equation and beam evolution is calculated numerically by the Fourier split-step method. Clearly, the idea works rather well, leading to a resolution of around 10 μm (50 optical wavelengths within the medium) which is mainly restricted by the non-ideal properties of the nonlinear crystal used. The resolution could be improved in materials that are more homogeneous (without defects or striations) and whose nonlinearity can be better characterized.

This back-propagation method has in fact been demonstrated in the past in a one-dimensional physical setting to recover the structure of ultrashort temporal pulses propagating in optical fibres[10]. More recently, it has successfully been introduced in wavelength-division multiplexing fibre systems used for optical communication, as a means of compensating for undesirable dispersive and nonlinear transmission effects[11]. The computational requirements for post-compensation of distributed nonlinearity were also discussed[11]. Fleischer and colleagues have now introduced the idea into the spatial domain and successfully handled the additional complexity incurred by the higher dimensionality. They extended the method from one-dimensional temporal pulses to two-dimensional pictures and were also able to recover the entire beam dynamics as the beam evolves in the third dimension (the propagation direction).

Clearly, universality is the merit of the approach by Fleischer and co-workers. But from a technological standpoint, it has one important limitation: long computation time, especially in the spatial domain. The computation time for transferring two-dimensional pictures through a nonlinear medium is considerable. It is not obvious whether the method is fast enough to be used for transmitting images at video rates through a fast-responding nonlinearity. Nevertheless, the intrusion of the ideas and algorithms in data processing into the highly nonlinear domain does signify a step forward in image processing. We certainly

envisage that, in the future, it would be possible to transmit pictorial information through nonlinear media at high data rates.

Can such techniques also provide information about evanescent waves that decay, by tracking them through their nonlinear coupling to propagating waves, as suggested by Fleischer and co-workers? That is another question worth pondering, because the nonlinear coupling from evanescent waves to propagating waves would have to dominate over the nonlinear coupling with noise (modulation instability), which is thermodynamically irreversible. On this question, the jury is still out. ❑

Mordechai Segev is at the Physics Department, Technion—Israel Institute of Technology, Haifa 32000, Israel, and Demetrios N. Christodoulides is at the College of Optics and Photonics—CREOL, University of Central Florida, Orlando, Florida 32816, USA.
e-mail: msegev@tx.technion.ac.il

References
1. Barsi, C., Wan, W. & Fleischer, J. W. *Nature Photon.* **3,** 211–215 (2009).
2. Yariv, A. *Opt. Commun.* **21,** 49–50 (1977).
3. Fischer, B. & Sternklar, S. *Appl. Phys. Lett.* **45,** 113–115 (1985).
4. Segev, M. & Yariv, A. *Opt. Lett.* **17,** 146–148 (1992).
5. Fischer, B. *et al. Appl. Phys. Lett.* **41,** 141–143 (1982).
6. Khyzniak, A. *et al. J. Opt. Soc. Am. A* **1,** 169–175 (1984).
7. Firstenberg, O. *et al. Phys. Rev. Lett.* **102,** 042601 (2009).
8. Kip, D. *et al. Opt. Lett.* **26,** 524–526 (2001).
9. Rotschild, C. *et al. Nature Photon.* **2,** 371–376 (2008).
10. Tsang, M., Psaltis, D. & Omenetto, F. *Opt. Lett.* **28,** 1873–1875 (2003).
11. Li, G. *Adv. Opt. Photon.* **1,** 279–307 (2009).

MAGNETO-OPTICS

Hot atoms rotate light rapidly

The ability to harness the Faraday effect on a short timescale in an ensemble of hot atoms may prove useful as a read-out tool for quantum information based on microscale vapour cells.

Robert Löw and Tilman Pfau

"Work. Finish. Publish." This advice from the English physicist and chemist Michael Faraday (Fig. 1) is just as appropriate today as when it was first coined in the nineteenth century. In 1845, his determined research led him to one of his most important discoveries. Faraday observed that a magnetic field could rotate the polarization of light in one of his homemade high-index 'heavy' glasses, and that the magnitude and direction of the rotation were dependent on the strength and direction of the magnetic field respectively.

Today the Faraday effect is a phenomenon routinely used in all optics

laboratories. Crystals such as borosilicate glasses or garnet crystals, which show a strong effect, are commonly used to build diodes for light, called optical isolators. The Faraday effect is also active and well studied in atomic gases. Here the most prominent application is magnetometry[1], where the polarization rotation can be used to measure small magnetic fields with a sensitivity of a few fT Hz$^{-1/2}$ with a measurement bandwidth of up to 1 kHz, sufficient for detecting human cardiomagnetic fields[2]. These gaseous sensors require narrow spectral features for best performance, and ideally one would like to use weakly

interacting laser-cooled atoms to avoid any unwanted broadening effects. As a result, much current research is devoted to studying colder and colder atoms, and narrower and narrower spectral features.

In contrast, on page 225 of this issue Paul Siddons and colleagues from Durham University[3] point out that the Faraday effect is actually a powerful tool in hot atomic gases for applications requiring large measurement bandwidth — that is, for measuring fast dynamics within the gas or the dynamics of external fields. The authors observe large Verdet constants (the measure of the strength of the Faraday

effect in a material) in thermal vapour cells for a spectral range of several gigahertz and response times of a few nanoseconds.

Now, bandwidth is a matter of viewpoint: a gigahertz bandwidth is considered broadband for atomic physicists but narrowband for optical communication applications and solid-state photonics, for example. So what could be interesting applications of broadband atomic physics in hot vapours?

Today's research efforts striving towards gaining quantum control on the single-particle level require fast detection methods to monitor coherent dynamics. The gigahertz-bandwidth Faraday effect demonstrated by Siddons *et al.* might be the right tool to observe and optimize the coherent dynamics in thermal vapour cells.

Extrapolating the observed gaseous Verdet constant to a single atom indicates that even one atom in an ensemble will cause a detectable Faraday rotation. This is also true for a thermal sample where the Faraday probe is detuned by several Doppler linewidths. This downscaling to the single-particle level is demanding but has been observed recently in artificial atoms, namely quantum dots[4]. Here the Faraday effect allowed the detection of the state of a single spin within an ensemble of electrons contained in a quantum dot.

Similarly, the detection of a single atomic state within a larger ensemble should also be possible for thermal atomic gases. In atomic physics it has been proposed to encode quantum information in long-lived collective nuclear spin states[5,6],

Figure 1 | Michael Faraday (1791–1876) with a slab of glass used in his famous discovery in 1845. (Detail of an engraving by Henry Adlard, based on an earlier photograph by Maull and Polyblank *circa* 1857.)
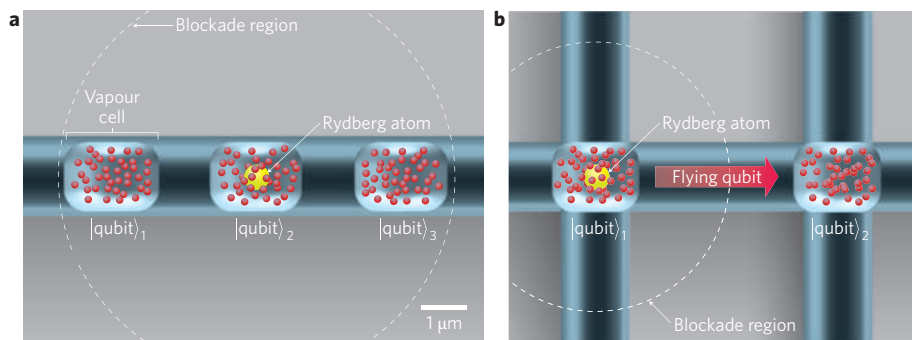
Figure 2 | Hot atoms for quantum computation? **a**, Collective nuclear spin polarization states in a micrometre-sized thermal vapour cell of atoms (red) could act as a representation of a qubit. They can be controlled and entangled by gate operations involving highly excited Rydberg atoms (yellow). **b**, Distant microcells can be interconnected by single photons. Microcells and waveguiding structures could be integrated to form a quantum information device. Broadband Faraday rotation might be a suitable detection tool to observe changes in individual nuclear and electronic spin states.

and the Faraday rotation may prove to be a powerful tool as a state-selective and fast read-out mechanism. A key element in these proposals is the strong interaction among atomic Rydberg states, which serve as a nonlinearity for two-qubit operations. The origin of this large interaction strength can be found in the loosely bound electrons in these high-lying states, which lead to very large polarizabilities.

As a consequence Rydberg atoms can show large dipole moments and van der Waals interaction strengths. The combination of strong interactions and coherent evolution has been recently investigated in an ensemble of frozen Rydberg atoms[7] and very recently also for single atoms[8,9] at ultra-cold temperatures. In these experiments the distance between the Rydberg atoms at which they are still strongly interacting reached several micrometres. In hot gases, despite the Doppler effect, pulsed lasers might enable coherent evolution of spin states at gigahertz frequencies, which requires an equally fast read-out mechanism.

The combination of the gigahertz Faraday effect demonstrated in this issue, together with recently observed coherent control of strongly interacting Rydberg atoms in atomic vapours, may ultimately lead to a new family of integrated quantum devices that operate at room temperature. Imagine the following situation: a set of mesoscopic samples of thermal atoms could be realized by micrometre-sized glass cells filled with hot atomic vapours, which are spaced such that the interaction among the Rydberg states is still effective (Fig. 2a). At moderate temperatures (for example, around 150 °C for rubidium) a mesoscopic number of atoms within a microscopic cell can be reached, in order

to allow collective quantum states[5,6]. The quantum information can now be stored in the hyperfine states of alkalis, which are long-lived owing to the weak coupling of the nuclear spin to its environment, and can show an energy separation much larger than the Doppler broadening.

The key ingredient for quantum information processing is the long-range interaction between the Rydberg atoms, which also penetrates dielectric media. A quantum gate for two neighbouring microcells — each representing a qubit (the digital bit used for quantum computation) — could be realized by state-selective excitation into a Rydberg state. The use of pulsed nanosecond (gigahertz-bandwidth) experiments could freeze out the thermal motion of the atoms, which causes unwanted decoherence. A gate operation depends on the individual qubit states of two neighbouring cells. The strong interaction between Rydberg atoms provides a blockade mechanism that prevents double excitation and ensures that each vapour cell contains only one Rydberg atom. The resulting nuclear spin states of such a gate could then be read out using the Faraday effect. The time resolution demonstrated by Siddons *et al.* would be ideally suited for monitoring the coherent evolution of the atomic ensemble. Such a design could be even scaled up to form a quantum network by connecting numerous micrometre-sized vapour cells by optical waveguides (Fig. 2b).

Each microcell should behave in a similar way to a single semiconductor quantum dot, where only a single exciton can be excited because of strong exciton–exciton interaction. This single excitation can be converted into a single photon, which serves as a 'flying' qubit.

NATIONAL PORTRAIT GALLERY

As microcells are slightly larger than the optical wavelength, the single photons emitted could be directed into optical waveguide structures, and flying qubits could connect distant microcells in a quantum network. The required building blocks for such networks, namely vapour cells and optical waveguides, can be integrated on one chip that operates at room temperature, providing a robust micrometre-scale quantum information device. Of course, to use this concept in real life many issues including confinement and wall-induced effects on the coherence properties will have to be studied and solved. But it looks like the work on the gigahertz Faraday effect presented in this issue may serve as an important read-out tool for quantum information technology based on hot atoms. Scientists working on hot atom quantum devices and networks are now free to follow Faraday's advice of "Work. Finish. Publish." ❐

Robert Löw and Tilman Pfau are at the 5. Physikalisches Institut, Universität Stuttgart, Pfaffenwaldring 57, 70569 Germany.
e-mail: t.pfau@physik.uni-stuttgart.de

References

1. Bloom, A. L. *Appl. Opt.* **1,** 61–68 (1962).
2. Bison, G., Wynands, R. & Weis, A. *Appl. Phys. B* **76,** 325–328 (2003).
3. Siddons, P. *et al. Nature Photon.* **3,** 225–229 (2009).
4. Atatüre, M. *et al. Nature Phys.* **3,** 101–105 (2007).
5. Lukin, M. D. *et al. Phys. Rev. Lett.* **87,** 037901 (2001).
6. Brion, E., Mølmer, K. & Saffman, M. *Phys. Rev. Lett.* **99,** 260501 (2007).
7. Heidemann, R. *et al. Phys. Rev. Lett.* **99,** 163601 (2007).
8. Gaëtan, A. *et al. Nature Phys.* **5,** 115–118 (2009).
9. Urban, E. *et al. Nature Phys.* **5,** 110–114 (2009).

Optomechanics of deformable optical cavities

Ivan Favero[1] and Khaled Karrai[2,3]

Resonant optical cavities such as Fabry–Perot resonators or whispering-gallery structures are subject to radiation pressure pushing their reflecting 'walls' apart. Deformable optical cavities yield to this pressure, but in doing so they in turn affect the stored optical energy, resulting in an optical back-action. For such cavities the optics and the mechanics become strongly coupled, making them fascinating systems in which to explore theories of measurements at the quantum limit. Here we provide a summary of the current state of optomechanics of deformable optical cavities, identifying some of the most important recent developments in the field.

The optomechanics of deformable optical cavities has seen a recent surge of interest. Research in this field, which started about 40 years ago, was and still largely remains driven by questions relating to the physics of measurements at the quantum fundamental limit. Good examples of this are the theoretical proposals formulated in the 1990s to perform quantum non-demolition measurements of the electromagnetic energy contained in a Fabry–Perot resonator by measuring the cavity elastic deformation under the effect of photon pressure. At that time, Braginsky, who pioneered the field, wrote that such a photon pressure probe, owing to "severe technical problems in its realization, is more a thought experiment than a foundation for a real measuring device"[1]. But now, technological advances in making deformable cavities, including nanofabrication techniques and high-quality optical coatings, are on the verge of allowing such a gedanken experiment to be practically explored in the laboratory. Here we present a brief overview of this rapidly evolving field of research.

Optical interferometers are ubiquitously used in length measurements requiring very high precision. When an interferometer is designed in such a way as to deform under the external action of an applied stress, the system is a precision force detector. Such force sensors are used in atomic force microscopy in the form of a deformable miniature Fabry–Perot interferometer[2], and are also at the heart of gravity-wave detectors[3] in the form of a deformable Michelson interferometer for detecting remote cosmic cataclysmic events. A schematic view of a deformable Fabry–Perot force sensor is shown in Fig. 1a: the two mirrors are attached to each other by a spring and the cavity is probed by a laser. In the simplest point of view, a force applied to one of the mirrors modifies the cavity length, which in turn modifies the cavity's optical transmission and reflectivity. A change of optical intensity at the detector, measuring for instance the transmission, is converted into force information. In the lowest level of approximation, light is just used to probe the cavity length changes and acts as a passive spectator. But to appreciate fully the fundamental detection limit of such an idealized force sensor, one needs to include the force added by the photons introduced into the cavity to perform the measurement in the first place. In the next level of approximation, the photons filling the cavity exert a pressure on the mirrors, causing them to displace and in turn detune the cavity with the result of modifying the very density of photons that were pressing against the mirrors to begin with. The mechanics and optics of the cavity are in fact coupled through the back-action of the photons on the mirror position. The
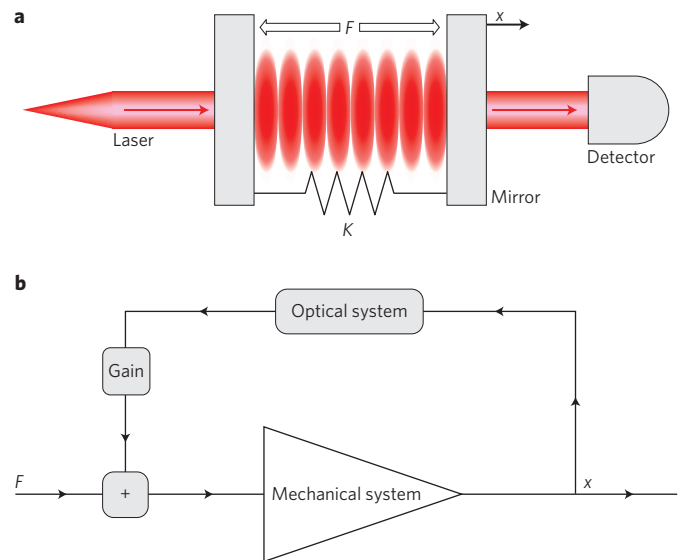
Figure 1 | Generic schematics of optomechanical sensors. a, Fabry–Perot interferometer force sensor. A force F acts on the right mirror (the mechanical system) of mass m, which is mounted on a mechanical spring K, while the laser probes the changes in cavity transmission. **b**, Feedback mechanism in an optomechanical sensor. The mechanical system moves under radiation pressure and fundamental fluctuations, and this displacement x modifies the density of light stored in the optical measuring device (the interferometer), leading to a change in the photo-induced force acting back on the mechanical system. This back-action is intrinsic to the deformable interferometer dynamics ('natural' self-cooling), but can also be externally implemented and amplified ('artificial' cold damping).

theoretical and experimental investigation of this apparently simple problem has recently flared into a number of rich and sometimes unsuspected new results.

The 'photon-spring'

Braginsky and co-workers published in 1970 a paper in which they investigated the effect of microwave power on a cavity with a deformable wall[4]. They provided a pioneering model in which a simple harmonic oscillator describes the mechanics of the deformable wall, laying the foundations of the optomechanics of

[1]Laboratoire Matériaux et Phénomènes Quantiques, Université Paris-Diderot, CNRS, 10 rue Alice Domon et Léonie Duquet, 75013 Paris, France. [2]CeNS, Ludwig-Maximilians Universität, Geschwister Scholl Platz 1, 80539 München, Germany. [3]attocube systems AG, Königinstrasse11a, D-80539 München, Germany. e-mail: ivan.favero@univ-paris-diderot.fr; karrai@lmu.de.

| Gram-scale mirror | Silicon nitride membrane 1 mm | Submillimetre mirror | AFM cantilever mirror | 100-μm silica micro-toroid cavity | 50-μm micro-mirror | 2-μm dwarf micro-mirror | Microwave and nanoresonator |

Diffraction limit barrier

1 cm   Size   100 nm

Figure 2 | Wide range of sizes of optomechanical deformable cavity systems showing self-cooling effects. Images show integrated mechanical systems ranging from centimetre size down to 100 nm. From left to right: a wire-suspended gram-scale mirror about 1 cm in size (image courtesy of MIT); a silicon nitride membrane[30] with ultra-high mechanical-Q (© 2008 NPG); a submillimetre ultra-high-reflectivity mirror (image courtesy of Laboratoire Kastler Brossel); a gold-coated AFM cantilever mirror forming a cavity with a coated optical fibre facet[29]; a high-optical-Q silica micro-toroid cavity[50]; a highly reflective Bragg micro-mirror deposited on a cantilever (image courtesy of Caltech); a metal-coated dwarf mirror at the diffraction limit[42] (© 2007 AIP); and a mechanical nanoresonator integrated in a strip-line microwave resonator[43] (© 2008 NPG).

deformable cavities[5]. Their analysis using Newtonian dynamics predicts that under the back-action of radiation pressure the mechanical oscillator displays an electromagnetically modified elastic spring constant K and a modified damping rate Γ. In short, the presence of radiation in a slightly detuned cavity introduces an added rigidity ∇F (that is, 'photon-spring') because the radiation density in the cavity, and consequently the radiation force F, depends on the oscillator's position. There is one subtlety, however: the photon back-action force acting on the cavity walls is not instantaneous, but is delayed with respect to sudden changes in the cavity size, and this is because the building of a new steady-state radiation density in the cavity requires a finite time-constant τ which is typically the electromagnetic energy storage time for the cavity. Like all retarded effects in dynamics, its contribution is to modify the amount of irreversible energy losses, namely the damping in the mechanics of the system. The net effect of introducing photon back-action is that the mechanical oscillator seems to be described by a shifted resonance frequency with a modified damping rate. In analogy, and in the spirit of modern quantum-optical language, one might say that the mechanical oscillator is 'photon-dressed'. In the limit of a rigid mechanical harmonic oscillator, for which the spring constant K dominates over the photon back-action spring (that is, $\nabla F << K$), the 'dressed' resonance ω and the damping Γ both have approximate analytical expressions in relation to their 'bare' counterparts ω_0 and Γ_0 (ref. 6):
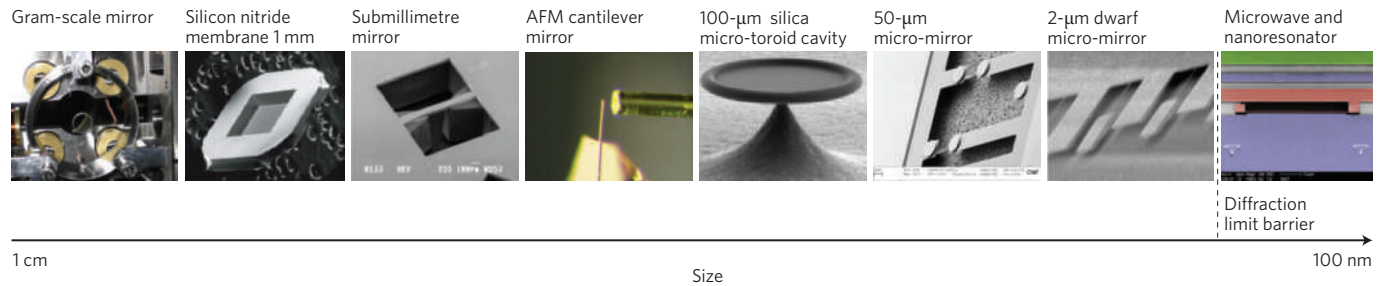
$$\omega \approx \omega_0 \sqrt{1 - \frac{1}{1 + \omega_0^2 \tau^2} \frac{\nabla F}{K}} \qquad (1)$$

$$\Gamma \approx \Gamma_0 \left(1 + Q \, \frac{\omega_0 \tau}{1 + \omega_0^2 \tau^2} \frac{\nabla F}{K} \right) \qquad (2)$$

where $Q = \omega_0/\Gamma$ is the bare mechanical quality factor, which is usually large (that is, $Q >> 1$). The peculiarity of such an optomechanical system is that these contributions to the mechanical resonance and the damping can be tuned to be positive or negative, by choosing the sign of the cavity detuning (that is, the photon-spring constant ∇F can be adjusted to be positive or negative).

The 1970 experimental results of Braginsky and co-workers showed, in the microwave domain, a hint of radiation-induced changes of the mechanical damping[4]. Shortly afterwards, they demonstrated in a beautiful experiment[5,7] that, still in agreement with their prediction[5,8], the resonance frequency of a torsion mechanical oscillator could also be shifted under the effect of radiation pressure in the visible domain. They dubbed their effect "light-rigidity"[5], but it is now better known as the optical spring effect. In 1983, Dorsel and co-workers investigated the strict analogue of Braginsky's

microwave deformable cavity; they conducted an experiment using a deformable optical Fabry–Perot interferometer operating this time in the visible range[9]. Their measurements showed that under intense laser illumination the mechanical rigidity of the interferometer could be optically modified to the point of complete cancellation, leading to sudden mechanical instability in the mirror position. This seminal experiment was followed by a number of theoretical studies relating to gravity-wave antenna from which it emerged that the Braginsky effect was apparently detrimental to optimal gravity-wave sensing, so schemes were essentially proposed to counteract the effect.

The photon back-action in the deformable cavity can be described as a feedback element linking the output to the input of a mechanical system (Fig. 1b). Today, deformable optical cavities exist in various forms of devices, as shown in Fig. 2. In the world of engineering, systems with feedback are very well understood in electronics, as well as in mechanical and electromechanical circuits, and, as is the case for the optomechanical effects investigated by Braginsky[5], the response function of a closed-loop system is generally very different from its open-loop counterpart. Closed-loop circuits involving a mechanical resonator and an optical feedback are, however, less known in device engineering. A nice system of an optomechanical circuit with a light-induced force external feedback was first used in a force detection scheme in atomic force microscopes (AFM)[10] to increase the mechanical damping artificially by optical means.

Laser cooling towards the quantum regime

Not only rigidity and damping but also fluctuations such as Brownian fluctuations are modified by back-action in a closed-loop circuit. In other words, the circuit effective temperature characterizing the system fluctuations can be controlled through back-action.

As early as 1953, the Brownian noise of an electrometer based on a torsion mirror galvanometer was greatly reduced by using a time-delayed electrical feedback acting on the mechanical system[11] prompting the authors to conclude with the visionary words that they had achieved "artificial cold damping to cryogenic temperature level usually only realizable in cryogenic laboratories". The idea of cold damping of fluctuations in the mechanics of a deformable Fabry–Perot cavity using an artificial optical feedback through radiation pressure was proposed and investigated theoretically in 1998 by Mancini and co-workers[12], and soon after was demonstrated in a beautiful experiment by Cohadon and co-workers[13]. In 2002, Braginsky and Vyatchanin[14] proposed to use the photon back-action damping intrinsic to a deformable cavity as a natural feedback mechanism to suppress the Brownian fluctuations in the mirror dynamics. Such a
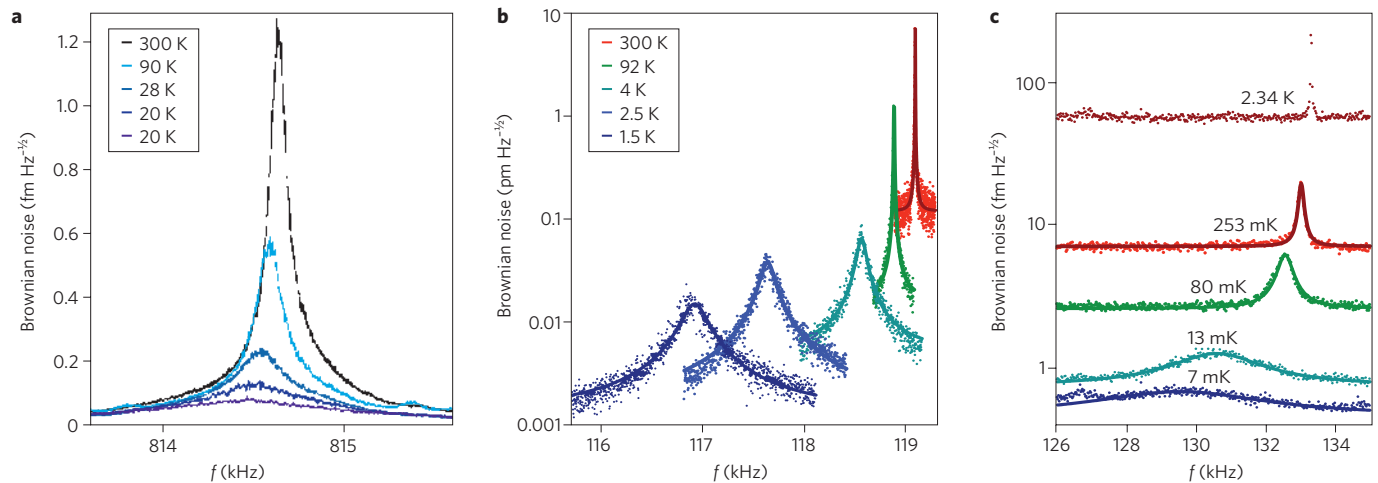
Figure 3 | Optomechanical radiation pressure self-cooling of deformable cavities. The spectra of Brownian fluctuations of various deformable Fabry–Perot cavities are shown for increasing strength of the 'photon-spring' contribution ∇F of radiation pressure (see text) at $\lambda = 1,064$ nm. The area under the curve is proportional to the mechanical oscillator fluctuation effective temperature. **a**, Data from ref. 21 and A. Heidmann et al. (personal communication), showing temperature reduction factor of 15 for $Q = 10,000$ and bath temperature of 300 K. The cavity finesse was ~30,000. **b**, **c**, Data from ref. 30 and J. G. E. Harris et al. (personal communication). The mechanical oscillator is a 1-mm^2 membrane of 50-nm thin silicon nitride placed at 300 K in 10^{-6} mbar vacuum within a high-finesse Fabry–Perot oscillator (finesse ~15,000). In **b**, $Q \approx 10^5$, and in **c**, $Q \approx 10^6$. Owing to lower mechanical dissipation of the oscillator, the cooling effect is increased and leads to a large temperature reduction factor of about 45,000.

'natural cold damping' (better known as self-cooling) turns out to be based on the same physical principles that lie behind laser cooling of ions[15] or vibration modes localized around impurities in semiconductors[16]. In 2004, optical self-cooling of a deformable Fabry–Perot cavity was demonstrated for the first time[6] under the effect of photothermal pressure. The effect showed that the Brownian fluctuations of a silicon microlever mirror could be cooled from 300 K down to 18 K. The prerequisite for self-cooling was first for the researchers to show that under the effect of optical back-action, deformable optical cavities displayed the expected optical control of rigidity and damping[17,18] as well as self-induced mechanical oscillation[19,20], which is the converse effect of self-cooling when the sign of the feedback is reversed. Soon after this, self-cooling of deformable cavities by radiation pressure was demonstrated almost simultaneously in various laboratories[21–24], triggering the race to extend self-cooling down to the quantum limit. An example of such cooling is shown in Fig. 3. Around the same time, there was a resurgence of interest in the method of artificial cold damping. Temperatures in the millikelvin range were achieved[25–27] by using externally amplified feedback, with record temperatures even down to the microkelvin range, in this case using electromechanical feedback[28].

Figure 3 shows the Brownian fluctuation noise spectrum for a few selected examples of cavity self-cooling. Clearly the effect of light back-action is to shift the resonance frequency, a very large modification of the linewidth (that is, damping rate) accompanied by a large change in the area covered by the Brownian resonance peak which provides a direct measurement of the vibrational temperature. For a rigid ($\nabla F << K$) mechanical harmonic oscillator the effective vibrational temperature reached with self-cooling is given[6,14,29] by $T_{eff} = T(\Gamma_0/\Gamma)$ which is minimized for a maximum increase of the 'dressed' damping Γ. What is the lowest temperature that a mechanical harmonic oscillator can reach by optical self-cooling? According to equation (2), the optical back-action on damping is optimized for $\omega_0\tau = 1$, that is, when the delay time constant τ becomes of the order of the mechanical oscillation period at resonance. For such a rigid oscillator, the minimum effective temperature T_{min} reachable by self-cooling is directly related to the bath temperature T, the bare mechanical quality factor Q and the relative shift in

resonance frequency $\Delta\omega/\omega_0$ induced by radiation pressure back-action directly measured in the Brownian noise spectrum:

$$T_{min} \approx \frac{T}{1 - 2Q\,(\Delta\omega\,/\,\omega_0)} \quad (3)$$

This formula is valid in a classical approximation of self-cooling in that it neglects photons quantum fluctuations and is expressed in the rigid harmonic oscillator limit (that is, $\Delta\omega << \omega_0$), which is the usual limit in experiments. It allows a simple and convenient evaluation of the minimal expected reachable temperature by optical self-cooling given the bath temperature T, the mechanical oscillator's 'bare' resonance frequency and the quality factor Q, while the cavity parameters and light intensity are all included in the negative frequency shift $\Delta\omega$ induced by the optical back-action. The quantum limit for the mechanical fluctuation is reached when the average number of vibrational quanta $N = k_B T_{min}/\hbar\omega_0$ becomes close to or even less than unity. For such a rigid oscillator with $\omega_0\tau = 1$ and in the limit of $Q >> 1$, the conditions to be fulfilled for the bath temperature and the related number of initial vibrational quanta N_T are, respectively, $k_B T < 2Q\hbar\Delta\omega$ and $N_T < 2Q\Delta\omega/\omega$.

In the rigid approximation $\Delta\omega << \omega_0$, we see that using a very large mechanical quality factor Q is central to self-cooling towards the quantum limit. Let us illustrate the point quantitatively. In Fig. 3b and c, a mechanical oscillator of high $Q \approx 10^6$ is placed in a high-finesse optical cavity[30]. The effect of photon back-action shifts the vibrational resonance up to $\Delta\omega/2\pi \approx 3$ kHz for a bare resonance of $\omega/2\pi \approx 130$ kHz while reducing the effective vibrational temperature down to ~7 mK from room temperature. Using the relations above, one would need to start ideally with a bath temperature of $T = 50$ mK in order to reach the quantum regime by self-cooling down to an effective temperature of $T_{min} \approx 22$ μK. This assumes, of course, that the light is not turned into heat by absorption in the mechanical resonator and that the condition $\omega_0\tau = 1$ is fulfilled.

Reaching the quantum limit for the vibrational mode of a harmonic mechanical oscillator means that it becomes decoupled from the incoherent thermal fluctuations present in its mass, and the result would be a purely coherent macroscopic state of the mechanical vibration. Its observation would be a good starting-point for studies
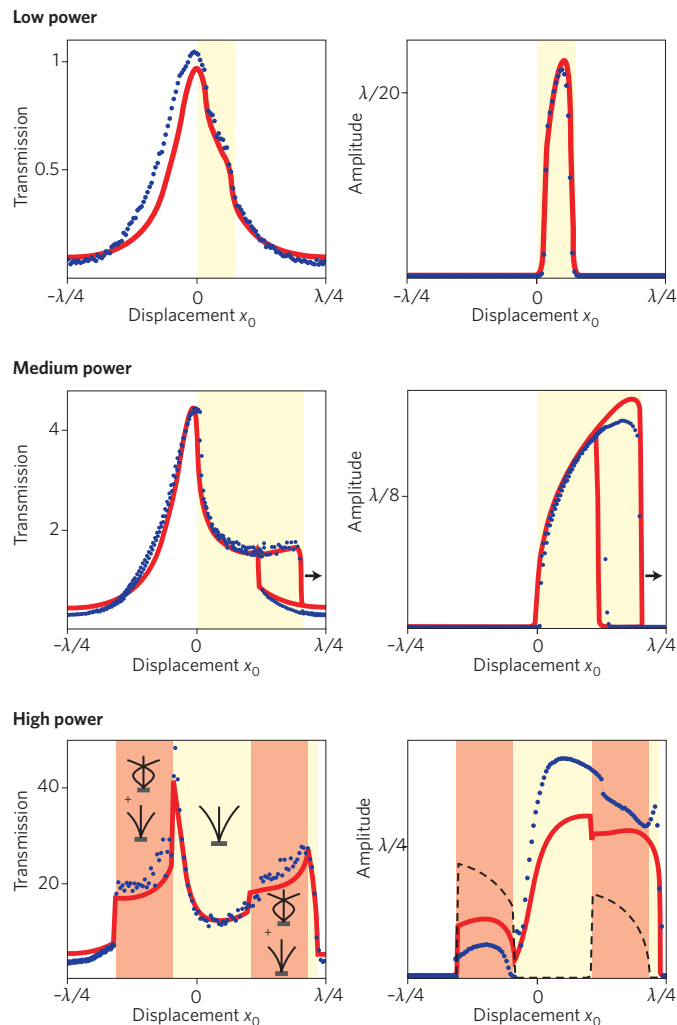
Figure 4 | Nonlinear dynamics of an optomechanical system. Left, optics: transmission of a deformable Fabry–Perot cavity as a function of cavity length variation x. At low optical power, the transmission is close to the transmission resonance of a conventional stiff Fabry–Perot cavity. Increasing the power leads to a complex behaviour, with the appearance of hysteresis and secondary transmission maxima. Right, mechanics: amplitude of the mechanical system self-oscillation driven by the photon back-action force. Reproduced with permission from ref. 46. © 2008 APS.

number of unity at best[36,37]. In the case of optomechanical systems coupled through other optical induced forces such as photothermal effects, the interaction involves a much larger number of degrees of freedom (phonons, electrons) and a Hamiltonian description is not yet available. This also applies to cooling through artificial cold damping, because the optomechanical interaction is mediated through a physical apparatus in the laboratory, which so far involves a quasi-infinite degree of freedom.

Trends

Efforts are currently being devoted to overcoming technical barriers to reaching the quantum regime. One of the challenges is still to design a system that minimizes both optical and mechanical losses. A possible strategy is to separate the functions of the mechanical oscillator from the optical one, allowing independent optimization of each. Thompson and co-workers[30], for instance, introduced a very high-Q thin flexible silicon nitride membrane into an otherwise stiff Fabry–Perot cavity of high finesse[39-40]. Figure 3b and c shows that this approach allows a reduction of the effective temperature down to 7 mK from room temperature. A related approach that has recently been proposed[41] would eventually allow researchers to venture below the diffraction barrier that usually limits optomechanical settings[42] and open the route to the use of nanomechanical objects for which the quantum limit could be reached close to the millikelvin range. In the visible and near-infrared range, subwavelength-sized nanostructures acting as the mechanical resonator introduced into a high-finesse optical cavity forming a coupled nano-optomechanical oscillator[41], are expected to show increased photon back-action. In the same spirit but in very different experiments, cooling of nanostructures by cavity perturbation was recently demonstrated in the microwave regime[43]. Another alternative approach proposed recently was to use the wavelength dependency of periodic structures near their band-stop to amplify laser Doppler cooling of a photonic crystal mounted on a flexible structure[44]. Such a nanophotonic device would also profit from photon back-action if its photonic band structure was tailored appropriately.

Finally, besides self-cooling and artificial cold damping, the strong coupling between optics and mechanics also leads to interesting nonlinear dynamics of the deformable cavity, still comparatively little investigated. Such a regime, first explored by Marquardt and co-workers[45] who predicted a rich phase diagram involving multistability parameter regions, has recently been observed[46], as seen in Fig. 4. Chaotic behaviour was also recently reported in high-finesse micro-toroid cavities[47]. Reducing the size, nano-optomechanical systems integrating extremely low-mass nanomechanical oscillators in a small optical volume should increase the coupling strength and allow exploration of these complex dynamical behaviours more deeply. Hybridized with high-Q optical micro or nanocavities, they could serve as a new platform in future optomechanics experiments.

In conclusion, the technology of optomechanical force sensors has evolved to the point where they are becoming a topic of research to explore their own fundamental quantum limit. They are, for example, viewed as ideal systems in which to verify theories in quantum measurement[1,48,49]. The quantum limit of an optomechanical system has not been reached yet, but the goal seems not too distant, thanks to recent advances in optical cooling methods. Such progress increases the prospect of applications in the field of quantum sensing devices. As yet, we barely know what to expect from such devices, and surprises are probably in store.

of quantum decoherence of massive mechanical systems[31–33], with expected new understanding of the boundary between quantum and classical physics[34]. At the time of writing and to the best of our knowledge, deformable optical cavities have not yet been cooled to their vibrational quantum ground state, but this goal seems in reach. Should they come closer to this limit, a full quantum theory of the optomechanical coupling governing their dynamics and their fluctuations is required, especially as the classical approach leading to equation (3) does not include quantum noise of the radiation, which can counteract self-cooling. In 1995, Law[35] provided a Hamiltonian description of radiation pressure on a moving mirror. This work was the basis for a quantum theory of optomechanical self-cooling in the case of radiation pressure coupling[36,37] as well as a description of optomechanical instability in the quantum regime[38]. The quantum theory of self-cooling by radiation pressure predicts[36,37] that the final vibrational occupation number will become lower than one only when $\omega_0\tau > 1$. The maximum cooling ratio is still obtained for $\omega_0\tau = 1$, but for this case it turns out that the photon fluctuation noise limits optical cooling to a vibrational occupation

References

1. Braginsky, V. B. & Khalili, F. Y. *Quantum Measurement* (Cambridge Univ. Press, 1992).
2. Rugar, D., Mamin, H. J. & Guethner, P. Improved fibre-optic interferometer for atomic force microscopy. *Appl. Phys. Lett.* **55,** 2588 (1989).
3. Reitze, D. Chasing gravitational waves. *Nature Photon.* **2,** 582–585 (2008).

4. Braginsky, V. B., Manukin, A. B. & Tikhonov, M. Yu. Investigation of dissipative ponderomotive effects of electromagnetic radiation. *Sov. Phys. JETP* **31,** 829 (1970).
5. Braginsky, V. B. & Manukin, A. B. *Measurement of Weak Forces in Physics Experiments* (Univ. Chicago Press, 1977).
6. Hohberger Metzger, C. & Karrai, K. Cavity cooling of a microlever. *Nature* **432,** 1002–1005 (2004).
7. Braginsky, V. B., Kuznetsov, V. A. & Rudenko, V. N. *Moscow Univ. Phys. Bull.* **26,** 92 (1971).
8. Braginsky, V. B. & Minakova, I. I. *Vestn. Mosk. Univ. Fiz.* **1,** 69 (1964).
9. Dorsel, A., McCullen, J. D., Meystre, P., Vignes, E. & Walther, H. Optical bistability and mirror confinement induced by radiation pressure. *Phys. Rev. Lett.* **51,** 1550–1553 (1983).
10. Mertz, J., Marti, O. & Mlyneck, J. Regulation of a microlever response by force feedback. *Appl. Phys. Lett.* **62,** 2344 (1993).
11. Milatz, J. M. W., Van Zolingen, J. J. & Van Iperen, B. B. The reduction in the Brownian motion of electrometers. *Physica* **XIX,** 195–207 (1953).
12. Mancini, S., Vitali, D. & Tombesi, P. Optomechanical cooling of a macroscopic oscillator by homodyne feedback. *Phys. Rev. Lett.* **80,** 688–691 (1998).
13. Cohadon, P., Heidmann, A. & Pinard, M. Cooling of a mirror by radiation pressure. *Phys. Rev. Lett.* **83,** 3174–3177 (1999).
14. Braginsky, V. B. & Vyatchanin, S. P. Low quantum noise tranquilizer for Fabry–Pérot interferometer. *Phys. Lett. A* **293,** 228–234 (2002).
15. Wineland, D. J. & Itano, W. M. Laser cooling of atoms. *Phys. Rev. A* **20,** 1521–1540 (1979).
16. Dykman, M. I. Heating and cooling of local and quasi-local vibrations by a nonresonance field. *Sov. Phys. Solid State* **20,** 1306–1311 (1979).
17. Vogel, M., Mooser, C., Karrai, K. & Warburton, R. Optically tunable mechanics of microlevers. *Appl. Phys. Lett.* **83,** 1337 (2003).
18. Sheard, B. S., Gray, M. B., Mow-Lowry, C. M., McClelland, D. E. & Whitcomb, S. E. Observation and characterization of an optical spring. *Phys. Rev. A* **69,** 051801 (2004).
19. Hohberger, C. & Karrai, K. Self-oscillation of micromechanical resonators. *Proc. 4th IEEE Conf. Nanotechnology,* 419–421 (IEEE, 2004).
20. Carmon, T., Rokhsari, H., Yang, L., Kippenberg, T. J. & Vahala, K. J. Temporal behaviour of radiation pressure induced vibrations of an optical microcavity phonon mode. *Phys. Rev. Lett.* **94,** 223902 (2005).
21. Arcizet, O., Cohadon, P. F., Briant, T., Pinard, M. & Heidmann, A. Radiation-pressure cooling and optomechanical instability of a micromirror. *Nature* **444,** 71–74 (2006).
22. Gigan, S. *et al.* Self-cooling of a micromirror by radiation-pressure. *Nature* **444,** 67–70 (2006).
23. Schliesser, A., Del'Haye, P., Nooshi, N., Vahala, K. J. & Kippenberg, T. J. Radiation pressure cooling of a micromechanical oscillator using dynamical backaction. *Phys. Rev. Lett.* **97,** 243905 (2006).
24. Corbitt, T. *et al.* An all-optical trap for a gram-scale mirror. *Phys. Rev. Lett.* **98,** 150802 (2007).
25. Kleckner, D. & Bouwmeester, D. Sub-kelvin optical cooling of a micromechanical resonator. *Nature* **444,** 75–78 (2006).
26. Poggio, M., Degen, C. L., Mamin, H. J. & Rugar, D. Feedback cooling of a cantilever's fundamental mode below 5 mK. *Phys. Rev. Lett.* **99,** 017201 (2007).
27. Mow-lowry, C. M., Mullavey, A. J., Gossler, S., Gray, M. B & McClelland, D. E. Cooling of a gram scale cantilever flexure to 70 mK with a servo modified optical spring. *Phys. Rev. Lett.* **100,** 010801 (2008).
28. Vinante, A. *et al.* Feedback cooling of the normal modes of a massive electromechanical system to submillikelvin temperature. *Phys. Rev. Lett.* **101,** 033601 (2008).
29. Metzger, C., Favero, I., Ortlieb, A. & Karrai, K. Optical self-cooling of a deformable Fabry–Perot cavity in the classical limit. *Phys. Rev. B* **78,** 035309 (2008).
30. Thompson, J. D. *et al.* Strong dispersive coupling of a high-finesse cavity to a micromechanical membrane. *Nature* **452,** 72–75 (2008).
31. Bose, J., Jacobs, K. & Knight, P. L. Preparation of nonclassical states in cavities with a moving mirror. *Phys. Rev. A* **56,** 4175–4186 (1997).
32. Bose, J., Jacobs, K. & Knight, P. L. Scheme to probe the decoherence of a macroscopic object. *Phys. Rev. A* **59,** 3204–3210 (1999).
33. Marshall, W., Simon, C., Penrose, R. & Bouweester, D. Towards quantum superposition of a mirror. *Phys. Rev. Lett.* **91,** 130401 (2003).
34. Leggett, A. J. Testing the limits of quantum mechanics: motivation, state of play, prospects. *J. Phys. Condens. Matter.* **14,** R415–451 (2002).
35. Law, C. K. Interaction between a moving mirror and radiation pressure: a Hamiltonian formulation. *Phys. Rev. A* **51,** 2537–2541 (1995).
36. Wilson-Rae, I., Nooshi, N., Zwerger, W. & Kippenberg, T. J. Theory of ground state cooling of a mechanical oscillator using dynamical backaction. *Phys. Rev. Lett.* **99,** 093901 (2007).
37. Marquardt, F., Chen, J. P., Clerk, A. A. & Girvin, S. M. Quantum theory of cavity-assisted sideband cooling of mechanical motion. *Phys. Rev. Lett.* **99,** 093902 (2007).
38. Ludwig, M., Kubala, B. & Marquardt, F. The optomechanical instability in the quantum regime. *New J. Phys.* **10,** 1–19 (2008).
39. Meystre, P., Wright, E. M., McCullen, J. D. & Vignes, E. Theory of radiation pressure driven interferometers. *J. Opt. Soc. Am. B* **2,** 1830–1840 (1985).
40. Battacharya, M., Uys, H. & Meystre, P. Optomechanical trapping and cooling of partially transparent mirrors. *Phys. Rev. A* **77,** 1–12 (2008).
41. Favero, I. & Karrai, K. Cavity cooling of a nanomechanical resonator by light scattering. *New J. Phys.* **10,** 095006 (2008).
42. Favero, I. *et al.* Optical cooling of a micromirror of wavelength size. *Appl. Phys. Lett.* **90,** 104101 (2007).
43. Regal, C. A., Teufel, J. D. & Lehnert, K. W. Measuring nanomechanical motion with a microwave cavity interferometer. *Nature Phys.* **4,** 555–560 (2008).
44. Karrai, K., Favero, I. & Metzger, C. Doppler optomechanics of a photonic crystal. *Phys. Rev. Lett.* **100,** 240801 (2008).
45. Marquardt, F., Harris, J. G. E & Girvin, S. M. Dynamical multistability induced by radiation pressure in high-finesse micromechanical optical cavities. *Phys. Rev. Lett.* **96,** 103901 (2006).
46. Metzger, C. *et al.* Self-induced oscillations in an optomechanical system driven by bolometric back-action. *Phys. Rev. Lett.* **101,** 133903 (2008).
47. Carmon, T., Cross, M. C. & Vahala, K. J. Chaotic quivering of micron-scaled on-chip resonators excited by centrifugal optical pressure. *Phys. Rev. Lett.* **98,** 167203 (2007).
48. Jacobs, K., Tombesi, P., Collett, M. J. & Walls, D. F. Quantum-nondemolition measurement of photon number using radiation pressure. *Phys. Rev. A* **49,** 1961–1966 (1994).
49. Pinard, M., Fabre, C. & Heidmann, A. Quantum-nondemolition measurement of light by a piezoelectric crystal. *Phys. Rev. A* **51,** 2443–2449 (1995).
50. Schiliesser, A., Riviere, R., Anetsberger, G., Arcizet, O., Kippenberg, T.J. Resolved-sideband cooling of a micromechanical oscillator. *Nature Phys.* **4,** 415–419 (2008)

Acknowledgements

Green light emission in silicon through slow-light enhanced third-harmonic generation in photonic-crystal waveguides

B. Corcoran[1], C. Monat[1]*, C. Grillet[1], D. J. Moss[1], B. J. Eggleton[1], T. P. White[2], L. O'Faolain[2] and T. F. Krauss[2]

Slow light has attracted significant interest recently as a potential solution for optical delay lines and time-domain optical signal processing[1,2]. Perhaps even more significant is the possibility of dramatically enhancing nonlinear optical effects[3,4] due to the spatial compression of optical energy[5-7]. Two-dimensional silicon photonic-crystal waveguides have proven to be a powerful platform for realizing slow light, being compatible with on-chip integration and offering wide-bandwidth and dispersion-free propagation[2]. Here, we report the slow-light enhancement of a nonlinear optical process in a two-dimensional silicon photonic-crystal waveguide. We observe visible third-harmonic-generation at a wavelength of 520 nm with only a few watts of peak power, and demonstrate strong third-harmonic-generation enhancement due to the reduced group velocity of the near-infrared pump signal. This demonstrates yet another unexpected nonlinear function realized in a CMOS-compatible silicon waveguide.

Although silicon has been the material of choice for the CMOS industry and more recently for integrated photonics, its optical properties—for example, light emission—still provide major challenges. In addition to an indirect bandgap and inversion symmetry, its strong absorption in the visible restricts the potential emission window to wavelengths above ~800 nm. Nonlinear optical effects, such as stimulated Raman scattering and third-harmonic generation (THG) offer new 'tricks' for light emission[8], thereby extending the functionality of silicon photonics.

Two-dimensional photonic crystals have recently attracted considerable attention by controlling the propagation of light in unprecedented ways[2,9]. In particular, they can produce slow light[1,2] with the ability to dramatically enhance nonlinear optical phenomena[3,4,7]. However, although nonlinear optical processes have been widely demonstrated in silicon nanowires[2,8,10,11], corresponding demonstrations in silicon photonic crystals—especially with slow light—have been elusive, only having been reported in the context of the electro–optic coefficient[12].

Here, we report visible (green light) THG in slow-light silicon photonic-crystal waveguides through end-fire coupling of near-infrared pulses with ~10 W peak pump power. This power is five to six orders of magnitude lower than that of earlier THG demonstrations in bulk silicon[13-16] and arises from a combination of extreme mode confinement by the photonic-crystal waveguide, slow-light enhancement and extraction of the visible light through the photonic-crystal lattice.

The generation of third-harmonic light (electric field intensity $I_{3\omega}$, frequency 3ω) from a fundamental pump beam (I_ω, ω)

propagating in a lossless homogeneous waveguide of length L is given by[17]

$$I_{3\omega} = (3\omega)^2 \left(\frac{2\pi}{nc}\right)^4 I_\omega^3 L^2 (\chi^{(3)})^2 \mathrm{sinc}^2 \left[\frac{\Delta k(\omega)L}{2}\right] f(A_\omega, A_{3\omega}) \quad (1)$$

where $\chi^{(3)}$ and n are the third-order nonlinear susceptibility and refractive index of silicon, respectively, $\Delta k = k_{3\omega} - 3k_\omega$ is the phase mismatch between the fundamental mode and the third-harmonic wavevectors and $f(A_\omega, A_{3\omega})$ accounts for the spatial overlap between the two modes. For perfect phase matching ($\Delta k = 0$) and maximum mode overlap ($f = 1$), equation (1) primarily reflects the THG cubic dependence on I_ω, which arises from the basic nature of the THG process—that is, converting three ω photons into a single 3ω photon (Fig. 1a). Clearly, then, increasing I_ω within the nonlinear material is crucial to enhancing the THG efficiency. This has been achieved in the past by using ultrahigh-Q, small-modal-volume silica microtoroids[18], although these tend to yield narrow bandwidth and dispersive features. Another approach has been to make use of the high density of states at the band-edge of periodic structures in various materials and geometries, such as Bragg gratings in porous silicon[19,20], two-dimensional GaN photonic crystals[21] and three-dimensional polystyrene photonic crystals[22]. These schemes generally involve a free-space configuration (reflection or diffraction surface probe experiments) where the lack of optical confinement limits the potential enhancement of I_ω, thus requiring megawatt peak pump powers.

Combining optical confinement and dispersion engineering through the use of optimized two-dimensional photonic-crystal waveguides[23-25] is highly promising because I_ω is related to the peak power (P_ω) through

$$I_\omega \propto \frac{P_\omega}{A_\omega} \cdot \frac{n_g}{n} \quad (2)$$

where A_ω and n_g are the effective area and group index of the fundamental mode, respectively. Hence, by using the extreme concentration of optical energy afforded by (i) the tight confinement of light within the high-index, sub-micrometre-scale ($A_\omega \approx 0.4\ \mu m^2$) silicon photonic-crystal waveguides and (ii) spatial pulse compression in the slow light ($v_g = c/40$) regime, we significantly reduce the peak pump power required to observe THG to 10 W. In addition, the photonic crystal structure provides a mechanism for light extraction at a wavelength that would otherwise be strongly
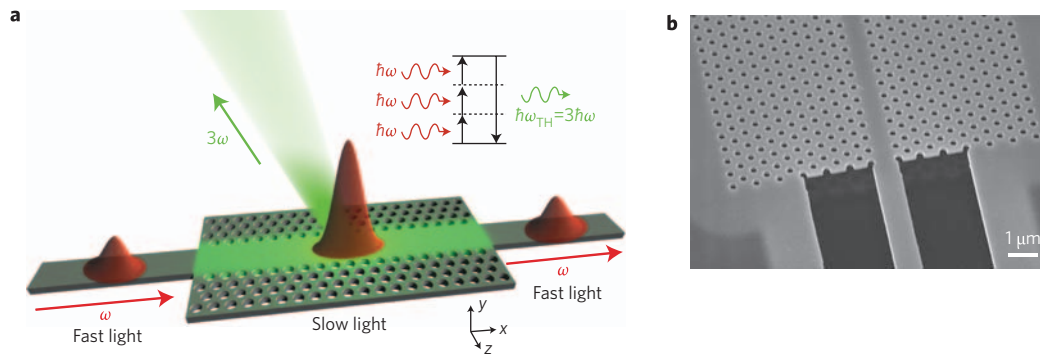
Figure 1 | Green light emission through third-harmonic generation (THG) in a slow-light photonic-crystal waveguide. a, Schematic of slow-light enhanced THG. The fundamental pulse at frequency ω (energy $\hbar\omega$) is spatially compressed in the slow-light photonic-crystal waveguide, increasing the electric field intensity, while the third-harmonic signal, at frequency $\omega_{TH} = 3\omega$, is extracted out-of-plane by the photonic crystal with a specific angle off the vertical direction. **b**, Scanning-electron-microscope (SEM) image of the tapered ridge waveguide connected to the photonic-crystal waveguide etched in a thin silicon membrane. Scale bar, 1 μm.
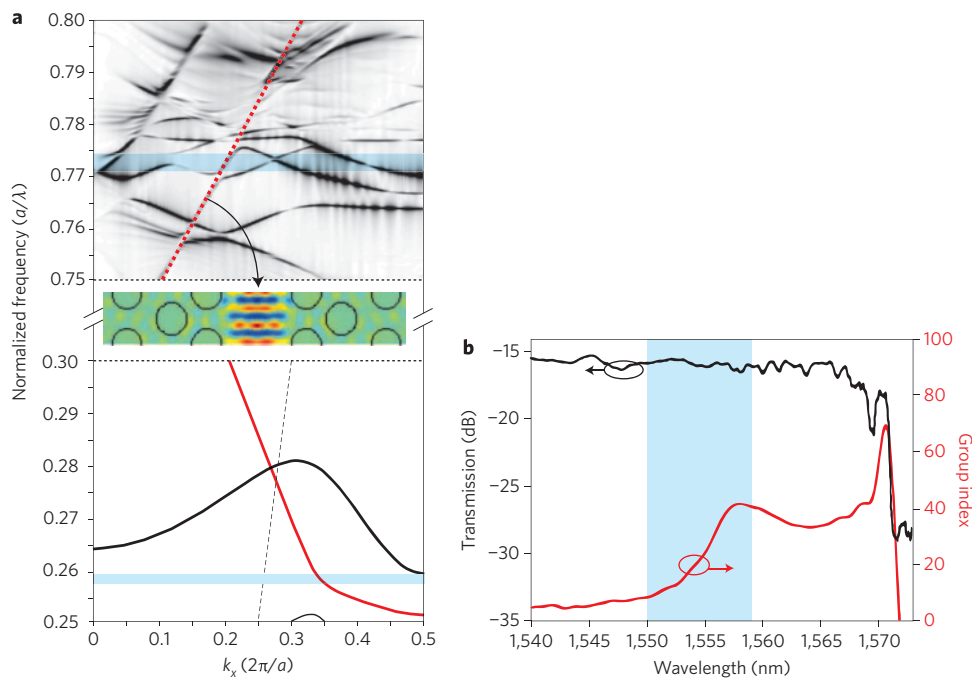
Figure 2 | Photonic-crystal waveguide dispersion. a, Two-dimensional finite-difference time-domain (FDTD) band structure calculated around 1,550 nm ($a/\lambda = 0.258$) and 520 nm ($a/\lambda = 0.77$). Only symmetric modes are displayed in the upper frequency window, with the dotted red line highlighting the fundamental refractive-like mode folded back into the first Brillouin zone (H_y mode profile in the inset) that can sustain the third harmonic. The black dashed line in the lower frequency window represents the light line, with the upper frequency region lying entirely above the light line. a is the lattice constant of photonic crystal and k_x is the wavevector in the x-axis. **b**, Measured transmission and group index of the photonic-crystal waveguide. The blue areas highlight the probed fundamental and third-harmonic spectral regions.

absorbed, thereby opening the spectral emission window of silicon to the visible.

Our device consists of an 80-μm-long W1 photonic-crystal waveguide in a 220-nm-thick air-suspended silicon slab, coupled to two tapered ridge waveguides (Fig. 1a,b). Unlike the highly dispersive slow-light mode associated with the band edge of typical photonic-crystal waveguides[26,27], here the fundamental mode is engineered to display both low group velocity and low dispersion[24] (Fig. 2a,b). Large dispersion typically broadens and distorts short pulses, which tends to compromise the benefits of slow light for nonlinear applications. In our case, however, we focus on the spectral window (1,550–1,559 nm) where the measured group velocity of the fundamental mode[28] varies almost linearly by a factor of 4 from $c/10$ to $c/40$ (Fig. 2b), enabling us to investigate the effect of group velocity.

When launching a near-infrared 1.5-ps pulse train (4 MHz) into the photonic-crystal waveguide, we observe green light emitted from the surface of the chip by eye (Fig. 3a). The emission is directional, being at an angle ∼10° from the vertical, in the backward direction, as indicated by the schematic in Fig. 1a. Imaging the emission onto a calibrated linear charge-coupled-device (CCD) camera using a microscope objective with a numerical aperture (NA) of 0.25 reveals that it is localized above the photonic-crystal waveguide and decays exponentially along its length (Fig. 3b). The total emitted green power (integrated spatially over the CCD image, Fig. 4) shows a cubic dependence on the coupled pump power of up to ∼65 μW, and is verified to have a wavelength of 520 ± 5 nm using bandpass filters, both of which are expected for a THG process driven by a 1,560-nm pump. At higher pump powers,

Figure 4 | Power dependence of the green light emission. The left axis (black circles) represents the measured visible green power as a function of the average near-infrared power coupled into the waveguide at 1,556.5 nm. The black solid line represents a cubic fit. The error bars are derived from noise estimation on the CCD. The right axis (red crosses) represents the transmitted average near-infrared power through the waveguide structure at 1,556.5 nm.
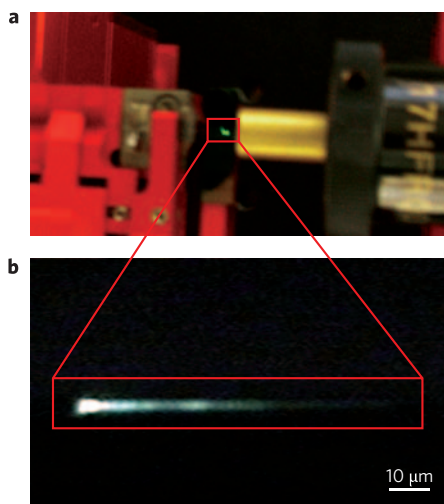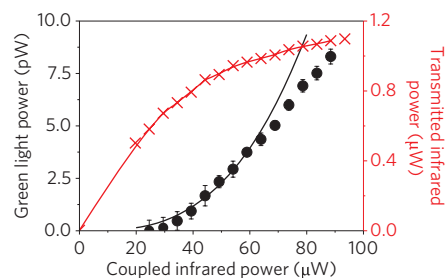

Figure 3 | Observation of green light. a, Visible green emission from the surface of the chip as seen by eye. **b**, Emission captured by a 0.25 NA microscope objective and imaged onto the CCD camera, with the enclosed box indicating the relative position of the photonic-crystal waveguide; the pump is injected from the left-hand side. Note that the green light emission starts at the entrance of the slow-light photonic-crystal section (after the first 10 photonic-crystal periods stretched to enhance coupling; see Methods) and decays exponentially along the photonic-crystal waveguide length.

a slight saturation occurs in the fundamental power transmission (see Fig. 4) due to two-photon and subsequent free-carrier absorption. We observe a maximum THG output of $\sim$10 pW for 80 μW (10 W) average (peak) pump power.

In general, there are a number of effects that can contribute to a variation in the THG efficiency along the waveguide, including group velocity dispersion (GVD) and nonlinear absorption, both of which degrade the fundamental pulse intensity along the photonic-crystal waveguide. It potentially also includes phase matching between the fundamental and third-harmonic modes, although here the extremely short ($\sim$1 μm) absorption length of the third-harmonic light in silicon damps this effect (see Methods). In order to minimize these effects and determine the dependence of the THG efficiency solely on group velocity, we therefore restricted our measurements to a region within 5 μm of the photonic-crystal waveguide entrance, which is much smaller than the dispersion length associated with the GVD, even in the 'fast light' regime (see Methods).

Figure 5a,b shows that the observed THG power displays a clear enhancement for pump wavelengths near 1,557 nm where the group velocity is lowest. Equation (1) predicts a cubic dependence on n_g of the THG power obtained at a fixed pump power. However, to minimize the nonlinear loss saturation effect discussed above at all wavelengths, we chose instead to plot on Fig. 5c,d the input power density P_ω/A_ω required to produce a constant (and sufficiently low) THG output power ($\sim$0.2 pW) as the wavelength (hence group index n_g) is varied. By plotting the power density P_ω/A_ω rather than power P_ω, we factor out the spectral dependence of A_ω and focus on the variation due solely to group index (see Methods). The results show very good agreement with a $1/n_g$ variation, as expected from equation (2); $P_\omega/A_\omega \propto I_\omega/n_g$ when considering a constant intensity I_ω responsible for a given THG signal. Note that both the trend and the variation in enhancement are well accounted for using only the experimentally measured group velocity dispersion of Fig. 2b. It is clear, then, that any contribution from other effects would cause a discrepancy with experiment, even if (by coincidence) its wavelength dependence happened to be identical to that of n_g. Hence, we believe these results conclusively demonstrate direct slow-light enhancement of this nonlinear process.

Our experiments were performed with $\sim$10 W peak pump powers, corresponding to a reduction of five to six orders of magnitude compared to previous reports[13–16] of THG in silicon. Even more significantly, this work represents a nearly 100-fold reduction in pump power relative to fully phase-matched THG in periodically-poled lithium niobate (PPLN)/potassium titanyl phosphate (KTP) waveguides[29]. Although a comparable power density ($\sim$GW cm^{-2}) has been achieved in ultrahigh-Q ($>1 \times 10^7$) cavities[18], the advantage of the photonic-crystal waveguide approach is that the full bandwidth of short optical pulses can be accommodated. We estimate our conversion efficiency η to be $\sim$1 $\times$ 10^{-7} (or 5 $\times$ 10^{-10} for 1 W of peak pump power), which represents an increase of five orders of magnitude over that reported in three-dimensional polystyrene photonic crystals ($\eta \approx 1 \times 10^{-15}$ for 1 W peak pump power as inferred from the quoted value of $\eta \approx 1 \times 10^{-5}$ at $P_\omega = 10$ MW; ref. 22). This efficiency could be further improved, for example, by decreasing the effective area ($\eta \propto 1/A_{eff}^3$) or the group velocity ($\eta \propto n_g^3$). A group velocity of $c/80$ can be reasonably well achieved with this photonic-crystal waveguide design[24]; this would provide an order of magnitude improvement in η. Efficiency could also be improved at high pump powers by reducing nonlinear losses (in particular due to free carriers) through techniques such as ion implantation.

As well as tight optical confinement and slow light, the two-dimensional photonic-crystal geometry offers additional versatility to improve the efficiency of the generation and extraction of third-harmonic light. In periodic structures, the phase-matching condition, $\Delta k = 0$, is relaxed to $\Delta k = \pm mG$, where mG can be any reciprocal lattice wavevector, increasing the possibilities for phase matching (see Methods). Perhaps more importantly in our case, because the absorption length at 3ω is extremely short (3 dB μm^{-1} absorption loss at 520 nm in silicon[30]), the photonic crystal also provides a suitable platform for extracting light by coupling to surface radiating modes above the light line. The directive nature of the emission ($\sim$10°) as well as the absence of green emission from the access waveguides, suggests that a component of the third-harmonic Bloch mode in the photonic crystal lies above the light line, as illustrated by the band structure in Fig. 2a. This provides a mechanism for the THG to be extracted out of plane. However, because the 3ω Bloch mode also contains harmonic components well confined in the photonic-crystal slab below the light line, the measured picowatt level of green emission is expected to be significantly lower than the total THG power generated in the photonic-crystal waveguide. The conversion efficiency reported above is therefore a conservative estimate. In addition, the photonic-crystal waveguide geometry was not optimized for third-harmonic extraction in this study, so modification may well increase overall
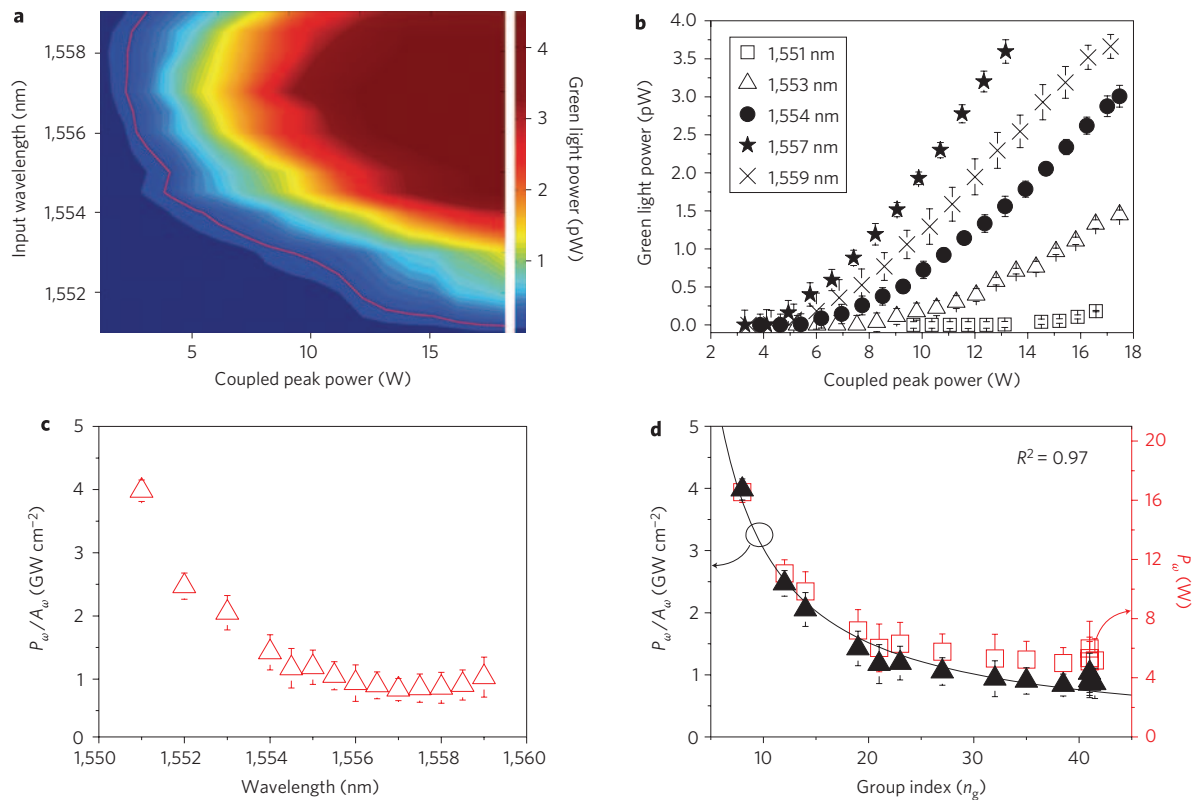
Figure 5 | Slow-light enhancement of green light emission. a,b, Green light power as a function of coupled near-infrared peak power (P_ω) for varying pump wavelengths. The constant power contour used for Fig. 5c,d appears as the dashed red line in **a**. **c,d**, Coupled peak power density (P_ω/A_ω) of the pump needed to observe a constant third-harmonic power of 0.2 pW as a function of the pump wavelength (**c**) and group index n_g (**d**). The error bars are derived from noise estimation on the CCD. The solid line in **d** represents a $1/n_g$ fit expected from the n_g-enhancement of the optical energy density. R^2 is a measure of goodness-of-fit.

device efficiency. Finally, we note that the optimization of all of these processes can be done across a wide range of frequencies, allowing one to address the entire visible spectrum, or to extend the THG to other spectral windows.

In conclusion, we report optical THG of visible (green) light, enhanced by a reduction in the group velocity, or slow light in two-dimensional silicon photonic-crystal waveguides. We observe visible green emission for only ∼10 W peak pump powers due to both the tight light confinement within the photonic-crystal waveguide and the energy density enhancement provided by the slow-light mode. Following recent observations of other nonlinear effects, such as efficient Raman amplification and four-wave mixing, the THG observed here further highlights the rich photonic functionality available with the silicon photonics platform.

Methods

Device structure and fabrication. The two-dimensional photonic-crystal structure consisted of a triangular lattice of air holes with lattice constant $a = 414$ nm and hole radius 118 nm ($0.286a$) etched into a 220-nm-thick silicon suspended membrane. A W1 waveguide was introduced by omitting a single row of holes along the ΓK direction to form a linear defect. The total photonic crystal length was 80 µm, and the lattice period of the first and last 10 periods was increased to 444 nm parallel to the waveguide to enhance coupling to the slow-light mode[31]. The dispersion of the photonic-crystal waveguide was engineered by shifting the first two rows of holes adjacent to the guide perpendicular to the direction of propagation[24]. For the waveguide used in this experiment, the first and second rows were shifted 52 nm away from and 12 nm toward the axis of the waveguide, respectively. Light was coupled in and out of the photonic-crystal waveguide through 2-mm-long ridge access waveguides with widths tapered from 3 to 0.7 µm over 200 µm close to the photonic-crystal waveguide, to improve coupling to the photonic crystal. The GVD β_2 for the engineered photonic-crystal guided mode ranged between 3×10^{-21} to 2.5×10^{-20} s² m⁻¹ for the spectral window of interest, providing an associated dispersion length for 1.5 ps pulses from 90 to 750 µm. This is longer than the entire photonic-crystal waveguide length

and much longer than the small 5 µm region considered in Fig. 5, and so we expect the effects of dispersion on our measurements to be negligible.

Note that this device was not optimized in terms of losses, which were dominated by coupling losses. There are several obvious routes to further improve this, for example, through the use of inverse tapers at the end-facets. The loss of 17 dB extracted from Fig. 4 comprises out-coupling losses (typically ∼10 dB and measured to be at best ∼8 dB), propagation loss in the ridge and nanowire segments (∼2–3 dB), scattering loss at the nanowire/photonic crystal interface (<1 dB) and the propagation losses in the photonic-crystal waveguide in the slow-light regime (2–3 dB).

The device was fabricated from a SOITEC silicon-on-insulator wafer by electron-beam lithography (hybrid ZEISS GEMINI 1530/RAITH ELPHY) and reactive ion etching using a CHF_3/SF_6 gas mixture. The silica layer under the photonic-crystal slab was selectively under-etched using a HF solution to leave the photonic crystal section in a suspended silicon membrane. More details of the procedure are given in ref. 32.

Transmission experiment. The device was probed using a polarization-controlled, near transform-limited, figure-of-eight fibre laser, tunable over the C-band. The pulses were sech²-shaped, ∼1.5 ps long, with a spectral full-width at half-maximum of ∼2 nm, and were amplified through an erbium-doped fibre amplifier. The pulses were launched into the transverse electric (TE)-like mode of the waveguide, using lensed fibres with a 2.5-µm focal spot diameter. To calculate the coupled power in Figs 4 and 5 from the power launched into the input lensed fibre, we estimated an in-coupling insertion loss of 8 dB. This is a typical value obtained from independent self-phase-modulation measurements on the same waveguide. Because this coupling loss is nonetheless the lowest typically measured, our estimation of the THG efficiency represents a low, or conservative, limit of the third-harmonic efficiency.

Green light measurement. The linearized, fixed-gain, CCD camera (Cohu 4910) was calibrated using a doubled Nd:YAG laser diode with a low relative intensity noise (RIN) with the power externally controlled by an attenuator assembly and monitored with a thermopile detector (Coherent PS10 and PowerMax meter).

Calculations. The band structures in Fig. 2a were calculated with a two-dimensional finite-difference time-domain (FDTD) method using effective material indices of 2.81 and 4.1 at the fundamental (∼1,550 nm) and third-harmonic (∼520 nm)

wavelengths, respectively, to account for the effects of confinement by the slab and the material dispersion of silicon[30]. Calculations were performed for a lattice period of $a = 414$ nm and hole radius $r = 0.286\, a$, given by the experimental parameters. The calculated dispersion curves for the fundamental mode at 1,550 nm were redshifted by less than 4% relative to the experimental measurements in Fig. 2b. The band structure shows that several symmetric modes (H_y symmetric across the waveguide, like the fundamental mode) exist at wavelengths close to 520 nm that can sustain the THG emission. We believe that the third-harmonic light is most likely coupled to the refractive-like mode highlighted by the dotted red line of Fig. 2a, which has the same symmetry as, and significant overlap with, the fundamental mode at 1,550 nm. Observation also yields an exit angle for the third-harmonic light at ~10° from the normal, which is reasonably consistent with coupling to this mode. We observed no noticeable change in exit angle with pump wavelength over the 10-nm wavelength range near 1,560 nm studied here, leading us to believe that there is no significant change in the third-harmonic mode over this range.

The effective mode field area (A_ω) of the fundamental mode was calculated using a three-dimensional plane wave method (PWM) and the equation

$$A_\omega = \frac{1}{a} \cdot \frac{(\int_{\mathrm{Vol}} |E|^2 \mathrm{d}V)^2}{\int_{\mathrm{Vol}} |E|^4 \mathrm{d}V}$$

where E is the electric field amplitude of the mode and Vol is the volume of a unit cell of length a associated with the photonic-crystal waveguide. This yields an increase of A_ω from 0.4 to 0.6 μm^2 for increasing wavelength over the range studied.

Phase-matching considerations. One might expect that because the fundamental wavevector varies by ~10% as the wavelength is tuned over a 10-nm range near 1,560 nm, it may influence the wavelength variation of the THG efficiency through the phase-matching term. In order to shed some light on the conclusion of our work that the observed enhancement in THG efficiency over the wavelength range studied is solely due to the group index $1/n_g$, we find it useful to compare characteristic length scales in our device. In periodic structures, the phase mismatch Δk between the fundamental and the third-harmonic modes is defined at $\pm mG$, where mG can be any reciprocal lattice wavevector. Therefore, $\Delta k < \pi/a$ (where a is the photonic-crystal lattice constant) and the associated coherence (or beating) length between the two modes L_{coh}, is thus always $>2a$ (~0.83 μm). From the specific band structure of Fig. 2a we further expect the coherence length to be above 2 μm. In silicon, because the absorption length of the third-harmonic light at 520 nm is ~1 μm < L_{coh}, the influence of phase-matching variation on the THG efficiency in our device is expected to be negligible. Further, notwithstanding this argument or the experimental evidence, we investigated the wavelength dependence of phase matching in our device by calculating it from the band structure, based on coupling to the third-harmonic mode discussed above, and assuming no losses at the third-harmonic wavelength, and we found that it was quite different to what was observed. Hence, for all of these reasons we believe these results conclusively demonstrate direct slow-light enhancement of this nonlinear process.

References

1. Krauss, T. F. Why do we need slow light? *Nature Photon.* **2**, 448–449 (2008).
2. Baba, T. Slow light in photonic crystals. *Nature Photon.* **2**, 465–473 (2008).
3. Soljacic, M. *et al.* Photonic-crystal slow-light enhancement of nonlinear phase sensitivity. *J. Opt. Soc. Am. B* **19**, 2052–2059 (2002).
4. Bhat, N. A. R. & Sipe, J. E. Optical pulse propagation in nonlinear photonic crystals. *Phys. Rev. E* **64**, 0566041 (2001).
5. Settle, M. D. *et al.* Flatband slow light in photonic crystals featuring spatial pulse compression and terahertz bandwidth. *Opt. Express* **15**, 219–226 (2007).
6. Krauss, T. F. Slow light in photonic crystal waveguides. *J. Phys. D* **40**, 2666–2670 (2007).
7. McMillan, J. F., Yang, X. D., Panoiu, N. C., Osgood, R. M. & Wong, C. W. Enhanced stimulated Raman scattering in slow-light photonic crystal waveguides. *Opt. Lett.* **31**, 1235–1237 (2006).
8. Jalali, B. Teaching silicon new tricks. *Nature Photon.* **1**, 193–195 (2007).
9. Vlasov, Y. A., O'Boyle, M., Hamann, H. F. & McNab, S. J. Active control of slow light on a chip with photonic crystal waveguides. *Nature* **438**, 65–69 (2005).
10. Bogaerts, W. *et al.* Nanophotonic waveguides in silicon-on-insulator fabricated with CMOS technology. *J. Lightwave Technol.* **23**, 401–412 (2005).
11. Lin, Q., Painter, O. J. & Agrawal, G. P. Nonlinear optical phenomena in silicon waveguides: Modeling and applications. *Opt. Express* **15**, 16604–16644 (2007).
12. Jacobsen, R. S. *et al.* Strained silicon as a new electro-optic material. *Nature* **441**, 199–202 (2006).
13. Wynne, J. J. Optical third-order mixing in GaAs Ge Si and InAs. *Phys. Rev.* **178**, 1295–1303 (1969).
14. Wang, C. C. *et al.* Optical third harmonic generation in reflection from crystalline and amorphous samples of silicon. *Phys. Rev. Lett.* **57**, 1647–1650 (1986).
15. Moss, D. J., Van Driel, H. M. & Sipe, J. E. Third harmonic generation as a structural diagnosis of ion-implanted amorphous and crystalline silicon. *Appl. Phys. Lett.* **48**, 1150–1152 (1986).
16. Moss, D. J., Van Driel, H. M. & Sipe, J. E. Dispersion in the anisotropy for optical third harmonic generation in Si and Ge. *Opt. Lett.* **14**, 57–59 (1989).
17. Boyd, R. *Nonlinear Optics*, Ch. 2 (Academic Press, 1992).
18. Carmon, T. & Vahala, K. J. Visible continuous emission from a silica microphotonic device by third-harmonic generation. *Nature Phys.* **3**, 430–435 (2007).
19. Martemyanov, M. G. *et al.* Third-harmonic generation in silicon photonic crystals and microcavities. *Phys. Rev. B* **70**, 073311 (2004).
20. Dolgova, T. V., Maidykovski, A. I., Martemyanov, M. G., Fedyanin, A. A. & Aktsipetrov, O. A. Giant third-harmonic in porous silicon photonic crystals and microcavities. *JETP Lett.* **75**, 15–19 (2002).
21. Coquillat, D. *et al.* Enhanced second- and third-harmonic generation and induced photoluminescence in a two-dimensional GaN photonic crystal. *Appl. Phys. Lett.* **87**, 101106 (2005).
22. Markowicz, P. P. *et al.* Dramatic enhancement of third-harmonic generation in three-dimensional photonic crystals. *Phys. Rev. Lett.* **92**, 083903 (2004).
23. Frandsen, L. H., Lavrinenko, A. V., Fage-Pedersen, J. & Borel, P. I. Photonic crystal waveguides with semi-slow light and tailored dispersion properties. *Opt. Express* **14**, 9444–9450 (2006).
24. Li, J., White, T. P., O'Faolain, L., Gomez-Iglesias, A. & Krauss, T. F. Systematic design of flat band slow light in photonic crystal waveguides. *Opt. Express* **16**, 6227–6232 (2008).
25. Kubo, S., Mori, D. & Baba, T. Low-group-velocity and low-dispersion slow light in photonic crystal waveguides. *Opt. Lett.* **32**, 2981–2983 (2007).
26. Notomi, M. *et al.* Extremely large group-velocity dispersion of line-defect waveguides in photonic crystal slabs. *Phys. Rev. Lett.* **87**, 2539021 (2001).
27. Engelen, R. J. P. *et al.* The effect of higher-order dispersion on slow light propagation in photonic crystal waveguides. *Opt. Express* **14**, 1658–1672 (2006).
28. Gomez-Iglesias, A., O'Brien, D., O'Faolain, L., Miller, A. & Krauss, T. F. Direct measurement of the group index of photonic crystal waveguides via Fourier transform spectral interferometry. *Appl. Phys. Lett.* **90**, 261107 (2007).
29. Rusu, M. *et al.* Efficient generation of green and UV light in a single PP–KTP waveguide pumped by a compact all-fiber system. *Appl. Phys. Lett.* **88**, 121105 (2006).
30. Green, M. A. & Keevers, M. J. Optical properties of intrinsic silicon at 300 K. *Progr. Photovoltaics Res. Appl.* **3**, 189–192 (1995).
31. Hugonin, J. P., Lalanne, P., White, T. P. & Krauss, T. F. Coupling into slow-mode photonic crystal waveguides. *Opt. Lett.* **32**, 2638–2640 (2007).
32. O'Faolain, L. *et al.* Low-loss propagation in photonic crystal waveguides. *Electron. Lett.* **42**, 1454–1455 (2006).

Additional information

Reprints and permission information is available online at http://npg.nature.com/reprintsandpermissions/. Correspondence and requests for materials should be addressed to C.M.

Imaging through nonlinear media using digital holography

Christopher Barsi[1], Wenjie Wan[1] and Jason W. Fleischer[1,2]*

It is well known that one cannot image directly through a nonlinear medium, as intensity-dependent phase changes distort signals as they propagate. Indirect methods can be used[1-6], but none has allowed for the measurement of internal wave mixing and dynamics. Recently, the reconstruction of nonlinear pulse propagation in fibres was demonstrated by generalizing the techniques of digital holography[7,8] to the nonlinear domain[9]. The method involves two steps: (1) recording the total field (both amplitude and phase) exiting a nonlinear medium and (2) numerically back-propagating the wavefunction. Here, we extend this process to two-dimensional spatial beams and experimentally demonstrate it in a self-defocusing photorefractive crystal, giving examples in soliton formation, dispersive radiation and imaging. For known nonlinearity, the technique enables reconstruction of wave dynamics within the medium and suggests new methods of super-resolved imaging, including subwavelength microscopy and lithography. For unknown nonlinearity, the method facilitates modelling and characterization of the optical response.

Image transmission through nonlinear materials has been studied for over thirty years[1]. Early methods sought to transmit images through turbulent/nonlinear media by means of phase conjugation and four-wave mixing[2-5]. However, backward geometries require a round trip in the nonlinear material[2,3], and forward geometries compete with other nonlinear processes, such as self-focusing, and often require extra processing to remove distortions[4,5]. More recently, incoherent solitons have been used as multimode waveguides[6], but their image quality is limited by intermodal dispersion[1]. Furthermore, all of these techniques obey imaging conditions that ignore (or compensate for) beam propagation within the volume of the medium. These restrictions are unfortunate, as observations of this evolution are vital to understanding the dynamical effects of nonlinearity, such as mode coupling, new frequency generation and modifications to the signal phase. In terms of imaging, this means that all internal wave mixing must be inferred from only the initial and final profiles, where linear optics can be used. Typically, theories of nonlinear beam propagation are tested experimentally in just this fashion: varying known input parameters and comparing measured outputs. With an accurate model of the underlying beam dynamics, however, this process can be reversed, using the measured output and numerically back-propagating the wave dynamics to recover the (unknown) input[9]. In addition, one can image the nonlinear evolution to an arbitrary axial position inside the material and thus reconstruct the field at any intermediate point.

As in linear digital reconstruction[8], the method requires knowledge of the full complex field exiting the sample. The amplitude can be recorded directly in a camera, but the phase requires an interference (holographic) measurement. In the experiments discussed below, the phase was captured with a standard phase-shifting
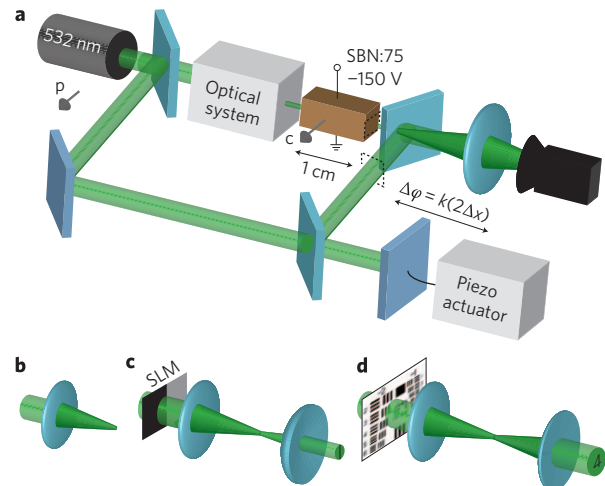
Figure 1 | Experimental set-up. Laser light (532 nm), polarized along the crystalline c-axis, is split into two beams. **a**, The object (upper) beam passes through the 'optical system' to generate the input waveform, which is projected onto the crystal. The reference (lower) beam is incremented in phase steps of $\Delta\varphi = \pi/2$; both beams are imaged onto the CCD camera (object planes indicated by dotted lines). **b–d**, Different optical systems are used, including a plano-convex lens creating a Gaussian beam (**b**), a spatial light modulator (SLM) producing a π-stripe (black, 0 rad; grey, π rad) (**c**), and a USAF 1951 resolution chart (**d**).

algorithm[10]. For a known propagator, this complex field can then be integrated numerically forwards or backwards. In the linear regime, for example, the field may be reconstructed simply by implementing the Fresnel transformation integral. For nonlinear propagation, this kernel is modified by an intensity-induced change to the phase.

For concreteness, we consider the simplest case of a scalar field undergoing paraxial dynamics. In this approximation, the propagation can be described by the nonlinear Schrödinger equation:

$$\frac{\partial \psi}{\partial z} = \left[i \frac{1}{2k} \nabla_\perp^2 + i\Delta n(|\psi|^2) \right] \psi \equiv \left[D + N(|\psi|^2) \right] \psi \qquad (1)$$

where $\psi(x,y,z)$ is the slowly varying envelope of the field, $k = 2\pi n_0/\lambda$, λ is the free-space wavelength, n_0 is the medium's base index, $\Delta n(|\psi|^2)$ is the nonlinear index change, and D and N are the linear and nonlinear operators, respectively. A typical choice for $\Delta n(|\psi|^2)$ is the cubic Kerr nonlinearity, with $\Delta n = \gamma |\psi|^2$ where γ is the non-linear coefficient. For any nonlinearity, however, issues of invertibility, integrability, vector decoupling and so on, must be considered. Noise and nonlinear instabilities must be examined as well.

[1]Department of Electrical Engineering, Princeton University, Princeton, New Jersey 08544, USA, [2]Program in Applied and Computational Mathematics, Princeton University, Princeton, New Jersey 08544, USA. *e-mail: jasonf@princeton.edu

Figure 2 | Nonlinear digital reconstruction of a self-defocused Gaussian beam. Left panels: intensity measurements. Right panels: phase measurements, modulo 2π. For both phase and intensity panels: top row, linear measurements; second row, nonlinear measurements; bottom row, numerical reconstructions. From left to right, each column represents 0, 5 and 10 mm distances. Scale bars, 50 μm.

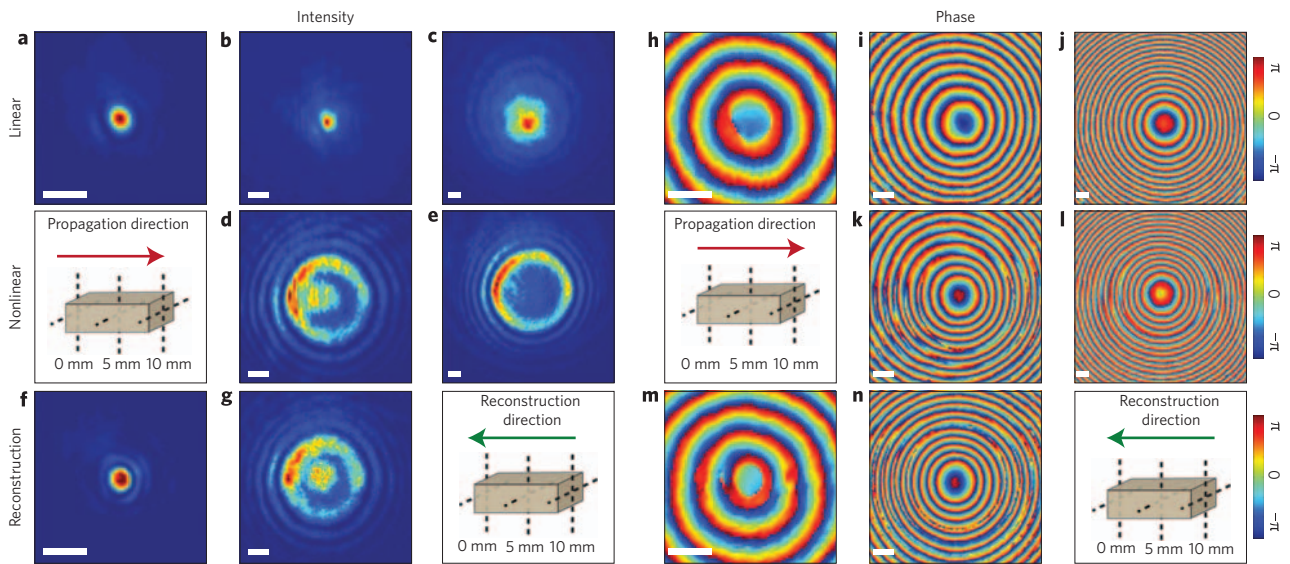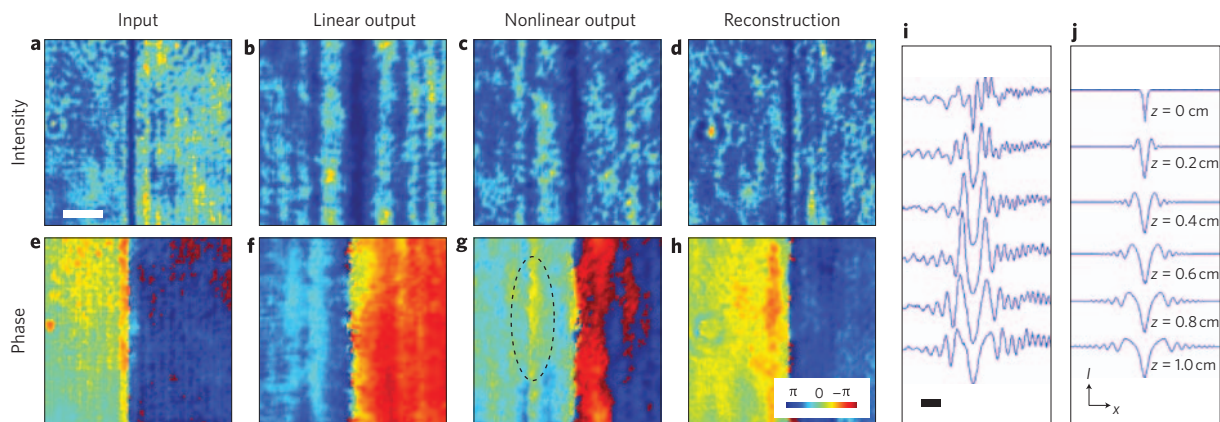**Figure 3 | Nonlinear reconstruction of evolution of a dark stripe. a–h,** Intensity and phase measurements: experimental input (**a,e**), linear output (**b,f**), nonlinear output (**c,g**), numerically reconstructed input (**d,h**). Top row: intensity profile. Bottom row: phase profile, modulo 2π. Scale bar, 50 μm. The dotted oval in **g** indicates appearance of $\pi/2$ discontinuity that is successfully eliminated upon reconstruction (**h**). **i,** Reconstruction cross-sections using a backwards propagation algorithm of the internal dynamics of the dark stripe. **j,** Simulation of evolution with 5% intensity noise. Scale bar, 50 μm.

The beam evolution can be calculated numerically using the Fourier split-step method, in which the linear and nonlinear operators act individually for each increment of propagation distance $\mathrm{d}z$:

$$\psi(z + \mathrm{d}z) \approx e^{\mathrm{d}z \cdot D} e^{\mathrm{d}z \cdot N(\psi)} \psi(z) \qquad (2)$$

Inverting the equation, that is, applying $\exp(-\mathrm{d}z \cdot N)\exp(-\mathrm{d}z \cdot D)$ to both sides, one can calculate the field at some location z_i given the field farther along the sample at location $z_f > z_i$:

$$\psi(z_i) \approx e^{-\mathrm{d}z \cdot N(\psi)} e^{-\mathrm{d}z \cdot D} \psi(z_f = z_i + \mathrm{d}z) \qquad (3)$$

This back-propagation is essentially an initial-value problem, in which the output is the starting point, and thus will work in situations where inverse scattering may fail, such as media with non-integrable nonlinearities. The method was first demonstrated for one-dimensional pulses in fibre[9] and has undergone much progress in the temporal domain[11,12]. Here, we extend the technique to

two-dimensional spatial beams containing image information, emphasizing that the higher dimensionality adds considerable complexity to the inversion, for example, by introducing degenerate solutions or an anisotropic response.

Experiments were performed using a $2 \times 5 \times 10$ mm³ photore-fractive strontium barium niobate (SBN:75) crystal with a self-defo-cusing nonlinearity, produced by applying an electric field of -750 V cm⁻¹ along the crystalline axis. As illustrated in Fig. 1, different extraordinarily polarized waveforms were projected onto the input face of the crystal, and the complex field at both the input and output faces was measured. The output field was then numerically back-propagated using equation (3) and compared with the measured input field. Technically, the photorefractive screening nonlinearity of this crystal is saturable, with a response $\Delta n \propto r_{ij} \bar{I}/(1 + \bar{I})$, where $\bar{I}$ is the intensity $I = |\psi|^2$, normalized to a background (dark current) intensity, and r_{ij} is the appropriate electro-optic coefficient[13,14]. However, recent experiments have shown that for the defocusing parameters considered here, the simpler Kerr nonlinearity $\Delta n = -|\gamma| I$ proves sufficient for
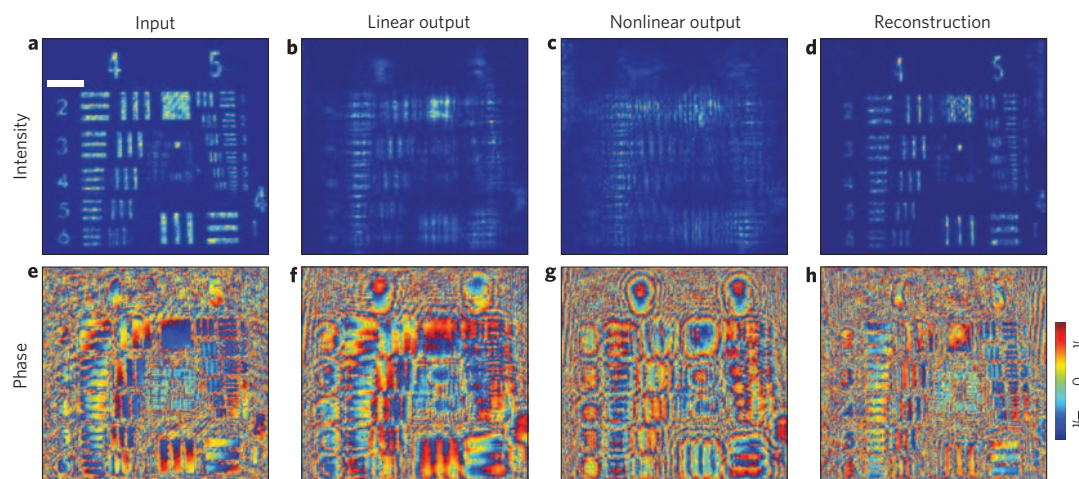
Figure 4 | Nonlinear digital reconstruction of a self-defocused USAF 1951 resolution chart. a–h, Intensity and phase measurements: experimental input (**a,e**), linear output (**b,f**), nonlinear output (**c,g**), numerically reconstructed input (**d,h**). Top row: intensity profile. Bottom row: phase profile, modulo 2π. Scale bar, 200 µm. Note that the ambiguity that leads to the random phase distribution in the dark regions is caused by the undefined phase there.

modelling[15]. Similarly, loss has been ignored, although the inclusion of linear operators such as absorption should not affect the reconstruction process[9]. On the other hand, the uniaxial nature of the crystal did introduce a slight anisotropy in the nonlinear response; our correction for this is discussed in the Methods section.

To calibrate the algorithm, we first focused a Gaussian beam of ~10 µW onto the input face of the crystal (Fig. 2a,h). Linear diffraction is shown in Fig. 2b,c,i,j, and nonlinear evolution in Fig. 2d,e,k,l. The dramatically different output in the nonlinear case, particularly after 10 mm of propagation (roughly three diffraction lengths), is shown in Fig. 2e. In particular, the nonlinear beam has a depleted central region and high-frequency fringes at the edges, a profile that cannot occur in the linear case (in which a Gaussian beam stays Gaussian). These features result from wavebreaking of the central portion of the beam into its own tails and are similar to the optical shocks demonstrated in other works[15,16]. This output field was back-propagated numerically to reconstruct the measured input, adjusting the nonlinear coefficient γ until the sum-of-squares error between the two profiles was minimized. As shown in Fig. 2f,m there is very good agreement in both phase and intensity with the experimental input. As a check, the experiment was then repeated with the shorter (5 mm) side of the crystal. As shown in Fig. 2d,k and 2g,n, the measured output after 5 mm of propagation matches the reconstruction resulting from back-propagating the 10 mm output halfway. The agreement is particularly pronounced in the asymmetry of the central portion of the beam, which is slightly left of centre. The nonlinear coefficient that was used to generate this reconstruction was then fixed and used for all subsequent experiments.

Although the expanding Gaussian beam experiences significant changes in both intensity and phase, other nonlinear structures, such as solitons, maintain constant-intensity profiles and acquire only an overall phase change upon propagation. Normally, experimental observations of these structures follow from launching a beam close to the initial soliton profile; confirmation is then reported by comparing the original input to the nonlinear output after several diffraction lengths. This observation method, however, says little about evolution towards a steady-state profile, especially for initial conditions far from the soliton existence curve. Cut-back methods provide volumetric information but require crystal damage or special geometry[17]. Other methods, such as near-field probes[18] and scattered-light measurements[17], are similarly direct but work well only for one-dimensional solitons and cross-sections. In contrast, the technique here allows

reconstruction, and thus effective imaging, of the beam dynamics all along its propagation, without relying on coupling mechanisms or material modification.

Figure 3 shows such evolution for a dark stripe (generated by a π-shift phase discontinuity) that is initially too narrow, for its intensity, to be a dark soliton. In the linear case (Fig. 3b), the stripe expands to roughly three times its original size. In the nonlinear case (Fig. 3c), the output stripe width has narrowed by ~30%. Numerical calculations show that this width coincides with the dark soliton width for the experimental parameters, but standard experimental techniques can say nothing more about the beam dynamics. In other words, without showing invariant propagation, the existence of a soliton could not be proved. Here, we use nonlinear digital holography to reconstruct the entire dynamics along the propagation path. As before, the first step is to reconstruct the input (Fig. 3d,h). Note that a phase defect at the output (Fig. 3g) has been eliminated successfully in the reconstruction. In Fig. 3i, we show several cross-sections of the reconstruction at intermediate distances within the crystal. As the beam propagates, the stripe widens to a dark soliton profile, radiating energy as it adjusts. The evolution is complex: the initial noise smoothens, owing to the defocusing nonlinearity, the beam profile becomes more symmetric, diffraction of the central dark stripe is arrested, and the radiated waves self-steepen and form dispersive shock waves[15,16]. Similar profiles have been observed in fibre solitons[19] but have not been demonstrated in the spatial case. Here, we reconstruct the entire dynamics, showing that the central profile settles into its dark soliton form at about 5 mm, whereas the tails need a longer propagation distance to relax. This semi-empirical reconstruction compares favourably with the ideal simulated case, shown in Fig. 3j.

A more complex example is provided by the nonlinear evolution of an Air Force 1951 resolution chart (Fig. 4). In the linear case, the input (Fig. 4a,e) has diffracted considerably (Fig. 4b,f), but the characters are still recognizable. After nonlinear propagation (Fig. 4c,g), however, the original intensity profile has been obliterated almost completely, especially for the numerical symbols, and the phase profile is severely blurred. Nevertheless, there is very good agreement between experimental and reconstructed phase and intensity. There is thus much potential in this technique for physical encryption. As with the dark soliton (Fig. 3f), the reconstruction of the phase is particularly well defined. This is both surprising and fortunate, because the phase is a much more sensitive quantity and typically carries more information[20]. Indeed, from Fig. 4h, it is possible
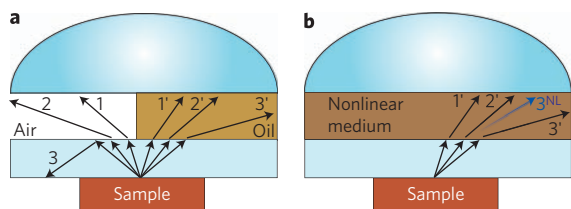
213

Figure 5 | Schematic for nonlinear holographic microscopy. a, Standard linear microscopy cannot capture rays 2 or 3. Index-matching between the sample slide and lens, through oil immersion, for example, allows detection of ray 2′, but ray 3′ still escapes. **b**, With immersion in a nonlinear medium, rays 3′ and 2′ can couple, generating a new (sum) wave, 3^{NL}, which can be detected. (The difference wave and similar coupling to ray 1′ are not shown.) Through nonlinear digital holography, the original wave 3′ can be reconstructed from the measured ray 3^{NL}, giving a higher effective numerical aperture.

to resolve the 10 μm bars of the chart, a resolution limited mainly by the non-ideal properties (defects and striations) of the crystal.

The sharpness of the reconstruction highlights an irony inherent in self-defocusing media: nonlinear mode-coupling of high spatial frequencies can lead to focusing effects[21–23]. (Although focusing nonlinearities can also couple these modes, noise-induced instabilities can dominate the signal and may limit the ability to invert equation (2).) The end results are larger effective numerical apertures and finer spatial resolution[24], so that the technique naturally leads to nonlinear extensions of digital microscopy. A simple ray-tracing schematic of this application, in transmission geometry, is shown in Fig. 5. Rays not captured by linear techniques (Fig. 5a) are still not captured in the nonlinear method (Fig. 5c), but information about them can be obtained through their daughter waves. Here, the super-resolution effect results from knowledge of the nonlinear propagation kernel. This allows reconstruction of the dynamics, deconvolution of the wave mixing, and therefore recovery of the underlying (missing) spatial features.

Theoretically, this method can be extended to near-field, subwavelength reconstructions as well. In this case, nonlinear wave mixing would couple evanescent waves with propagating ones (although a more accurate model than equation (1) would be necessary). This method has potential to work follows from recent observations of the Goos–Hänchen effect[25], in which a totally internally reflected beam is spatially translated from the incident beam. This translation, owing to phase shifts of evanescent waves at the interface[26], is normally on the order of a wavelength but can be enhanced significantly by nonlinearity[27–29]. Combined with the reconstruction algorithm, this coupling of near-field behaviour with far-field propagation could be extended to imaging. Moreover, unlike traditional point-by-point scanning techniques[30], the nonlinear digital holography presented here is an inherently wide-angle, far-field form of microscopy. From the opposite perspective, such nonlinear wave mixing could allow subwavelength lithography with super-wavelength-scale initial patterns.

The limits on resolution depend on the underlying nature of the nonlinearity, the quality of the medium and the effects of noise. For example, the photorefractive crystal used above is a poor choice for high-resolution experiments, because the charge transport of its material response is inherently nonlocal. The most serious obstacle is noise, both as a detriment to the signal and as an irreversible source of instability. For example, nonlinear coupling can lead to modulation instabilities, even in defocusing media[21]. On the other hand, we note that nonlinearity leads naturally to optical squeezing, and with the hope that quantum optics can improve upon the classical ideas presented here. The ultimate resolution limits of the technique, therefore, remain to be determined.

In conclusion, we have successfully carried out the digital reconstruction of optical spatial beams propagating in a nonlinear medium. This should prove useful both for basic studies of coupled wave dynamics and for new methods of image/signal processing.

Methods

To create the input, a wide, collimated beam from a 532 nm Coherent Verdi laser was split into two parts, as shown in Fig. 1. The lower, unmodified beam acted as a plane-wave reference, which was reflected from a mirror with a longitudinal position controlled by a piezo-electric actuator. The upper beam was passed through a different optical system for each of the above experiments to create different object signals. The input/output object beam was combined with the reference beam using a beamsplitter, and the total field was then imaged onto a charge-coupled-device (CCD) camera (520 × 492 array with a pixel size of 9.9 μm). The image was magnified approximately four times with a lens to better resolve the features of the field. To shift the reference beam, the piezo-actuated mirror was stepped in increments of $\lambda/4 \pm 5$ nm. Note that although the imaging lens itself gives rise to a quadratic phase factor, because both reference and object beams are imaged together, no extraneous fringes in the interference pattern are produced.

Details of the object beam generation for each experiment are as follows. For the Gaussian-shock example in Fig. 2, the beam was simply focused onto the input face of the crystal using a 20 cm plano-convex lens. The narrow dark stripe in Fig. 3 was created by imprinting a phase discontinuity onto the object beam with a phase-only spatial light modulator. It was imaged and demagnified eight times with a 4f system. Finally, the resolution chart in Fig. 4 was imaged with a 4f system as well, with unity magnification.

For the digital reconstruction, the frames recorded by the camera were cropped horizontally, and padded with zeros vertically to create 512 × 512 pixel frames. In this way, the beam propagation code could best make use of the fast Fourier transform (FFT) algorithm in the linear step. The numerical pixel size was matched with the effective (demagnified) camera pixel size, 2.5 μm, and the propagation step size was 65 μm. A decrease in the step size to 20 μm showed no appreciable change in the reconstruction, confirming that numerical convergence had been achieved. Note that, in order to yield the circularly symmetric beam of Fig. 2f, a small anisotropic correction of 7% was included for the index of refraction in the x-direction for the linear propagator, that is, in the Fourier domain

$$e^{-i\frac{\lambda\Delta z}{4\pi}\left(\frac{k_x^2}{n_0}+\frac{k_y^2}{n_0}\right)} \rightarrow e^{-i\frac{\lambda\Delta z}{4\pi}\left(\frac{k_x^2}{n_0(1+\delta)}+\frac{k_y^2}{n_0}\right)} \tag{4}$$

where $\delta = 0.07$ and k_x and k_y are the wavevectors for the x- and y-axis. δ was held constant, although functional dependence on the intensity did not change the result. This numerical solution affected the Gaussian beam at its focus only. Furthermore, it did not affect the other reconstructions. Therefore, we suspect that this modification becomes necessary for high-intensity, focused beams. Other, more complex, models of the photorefractive nonlinearity that include charge transport and saturation effects were not as successful at recovering the input.

References

1. Yariv, A. Three-dimensional pictorial transmission in optical fibers. *Appl. Phys. Lett.* **28,** 88–89 (1976).
2. Yariv, A. Compensation for atmospheric degradation of optical beam transmission by nonlinear optical mixing. *Opt. Commun.* **21,** 49–50 (1977).
3. Fischer, B., Cronin-Golomb, M., White, J. O. & Yariv, A. Real-time phase conjugate window for one-way optical field imaging through a distortion. *Appl. Phys. Lett.* **13,** 141–143 (1982).
4. Khyzniak, A. et al. Phase conjugation by degenerate forward four-wave mixing. *J. Opt. Soc. Am. A* **1,** 169–175 (1984).
5. Jones, D. C., Lyuksyutov, S. F. & Solymar, L. Three-wave and four-wave forward phase-conjugate imaging in photorefractive bismuth silicon oxide. *Opt. Lett.* **15,** 935–937 (1990).
6. Kip, D., Anastassiou, C., Eugenieva, E., Christodoulides, D. & Segev, M. Transmission of images through highly nonlinear media by gradient-index lenses formed by incoherent solitons. *Opt. Lett.* **26,** 524–526 (2001).
7. Schnars, U. & Jüptner, W. Direct recording of holograms by a CCD target and numerical reconstruction. *Appl. Opt.* **33,** 179–181 (1994).
8. Schnars, U. & Jüptner, W. P. O. Digital recording and numerical reconstruction of holograms. *J. Meas. Sci. Technol.* **13,** R85–R101 (2002).
9. Tsang, M., Psaltis, D. & Omenetto F. Reverse propagation of femtosecond pulses in optical fibers. *Opt. Lett.* **28,** 1873–1875 (2003).
10. Yamaguchi, I. & Zhang, T. Phase-shifting digital holography. *Opt. Lett.* **22,** 1268–1270 (1997).

11. Goldfarb, G. & Li, G. Demonstration of fibre impairment compensation using split-step infinite-impulse-response filtering method. *Electron. Lett.* **44,** 814–815 (2008).

12. Mateo, E., Zhu, L. & Li, G. Impact of XPM and FWM on the digital implementation of impairment compensation for WDM transmission using backward propagation. *Opt. Express* **16,** 16124–16137 (2008).

13. Segev, M., Valley, G. C., Crosignani, B., Diporto, P. & Yariv, A. Steady-state spatial screening solitons in photorefractive materials with external applied field. *Phys. Rev. Lett.* **73,** 3211–3214 (1994).

14. Christodoulides, D. N. & Carvalho, M. I. Bright, dark and gray spatial soliton states in photorefractive media. *J. Opt. Soc. Am. B* **12,** 1628–1633 (1995).

15. Wan, W., Jia, S. & Fleischer, J. W. Dispersive, superfluid-like shock waves in nonlinear optics. *Nature Phys.* **3,** 46–51 (2007).

16. Ghofraniha, N., Conti, C., Ruocco, G. & Trillo, S. Shocks in nonlocal media. *Phys. Rev. Lett.* **99,** 043903 (2007).

17. Shih, M. *et al*. Two-dimensional steady-state photorefractive screening solitons. *Opt. Lett.* **21,** 324–326 (1996).

18. Linzon, Y. *et al*. Near-field imaging of nonlinear pulse propagation in planar silica waveguides. *Phys. Rev. E* **72,** 066607 (2005).

19. Krökel, D., Halas, N. J., Giuliani, G. & Grischkowsky, D. Dark-pulse propagation in optical fibers. *Phys. Rev. Lett.* **60,** 29–32 (1988).

20. Oppenheim, A. V. & Lim, J. S. The importance of phase in signals. *Proc. IEEE* **69,** 529–541 (1981).

21. Agrawal, G. P. Modulation instability induced by cross-phase modulation. *Phys. Rev. Lett.* **59,** 880–883 (1987).

22. Stentz, A. J., Kauranen, M., Maki, J. J., Agrawal, G. P. & Boyd, R. W. Induced focusing and spatial wave breaking from cross-phase modulation in a self-defocusing medium. *Opt. Lett.* **17,** 19–21 (1992).

23. Hickmann, J. M., Gomes, A. S. L. & de Araújo, C. B. Observation of spatial cross-phase modulation effects in a self-defocusing nonlinear medium. *Phys. Rev. Lett.* **68,** 3547–3550 (1992).

24. Jia, S., Wan, W. & Fleischer, J. W. Forward four-wave mixing with defocusing nonlinearity. *Opt. Lett.* **32,** 1668–1670 (2007).

25. Goos, F. & Hänchen, H. Ein neuer und fundamentaler versuch zur totalreflexion. *Ann. Phys.* **1,** 333–346 (1947).

26. Artmann, K. Berechnung der seitenversetzung des totalreflektierten strahles. *Ann. Phys.* **2,** 87–102 (1947).

27. Tomlinson, W. J., Gordon, J. P., Smith, P. W. & Kaplan, A. E. Reflection of a Gaussian beam at a nonlinear interface. *Appl. Opt.* **21,** 2041–2051 (1982).

28. Emile, O., Galstyan, T., Le Floch, A. & Bretenaker, F. Measurement of the nonlinear Goos–Hänchen effect for Gaussian optical beams. *Phys. Rev. Lett.* **75,** 1511–1513 (1995).

29. Jost, B. M., Al-Rashed, A.-A. R. & Saleh, B. E. A. Observation of the Goos–Hänchen effect in a phase-conjugate mirror. *Phys. Rev. Lett.* **81,** 2233–2235 (1998).

30. Ash, E. A. & Nicholls, G. Super-resolution aperture scanning microscope. *Nature* **237,** 510–512 (1972).

Author contributions

All authors have contributed to this paper and agree to its contents.

Additional information

Reprints and permission information is available online at http://npg.nature.com/reprintsandpermissions/. Correspondence and requests for materials should be addressed to J.W.F.

All-optical high-speed signal processing with silicon–organic hybrid slot waveguides

C. Koos[1†], P. Vorreau[1], T. Vallaitis[1], P. Dumon[2], W. Bogaerts[2], R. Baets[2], B. Esembeson[3], I. Biaggio[3], T. Michinobu[4], F. Diederich[4], W. Freude[1*] and J. Leuthold[1*]

Integrated optical circuits based on silicon-on-insulator technology are likely to become the mainstay of the photonics industry. Over recent years an impressive range of silicon-on-insulator devices has been realized, including waveguides[1,2], filters[3,4] and photonic-crystal devices[5]. However, silicon-based all-optical switching is still challenging owing to the slow dynamics of two-photon generated free carriers. Here we show that silicon–organic hybrid integration overcomes such intrinsic limitations by combining the best of two worlds, using mature CMOS processing to fabricate the waveguide, and molecular beam deposition to cover it with organic molecules that efficiently mediate all-optical interaction without introducing significant absorption. We fabricate a 4-mm-long silicon–organic hybrid waveguide with a record nonlinearity coefficient of $\gamma \approx 1 \times 10^5$ W^{-1} km^{-1} and perform all-optical demultiplexing of 170.8 Gb s^{-1} to 42.7 Gb s^{-1}. This is—to the best of our knowledge—the fastest silicon photonic optical signal processing demonstrated.

Silicon processing technology has developed to the extent that millimetre-scale devices are routinely fabricated with nanometre precision in modern high-volume complementary metal-oxide–semiconductor (CMOS) lines. This mature technology has now also made silicon-on-insulator (SOI) an attractive platform for photonic integration. Being transparent at infrared telecommunication wavelengths, silicon is suitable for use in passive linear devices. For active devices, such as on-chip lasers and amplifiers, the indirect bandgap of silicon presents an obstacle and has to be overcome, either by making use of Raman amplification[6,7] or by bonding III–V heterostructures onto SOI waveguides. The latter technique enables fabrication of electrically pumped amplifiers[8], continuous-wave (c.w.) lasers[9,10], mode-locked lasers[11] and photodetectors[12].

However, there are other optical functionalities, in particular nonlinear ones, that cannot be realized easily when relying only on the intrinsic properties of silicon. Second-order optical nonlinearities are absent in unstrained bulk silicon because of its centrosymmetry, so recent high-speed modulators are based on free-carrier injection, allowing for transmission speeds of up to 40 Gb s^{-1} (ref. 13). Third-order nonlinearities, which enable all-optical switching and wavelength conversion, are present in silicon, but functionality is limited by two-photon absorption (TPA) and speed limitations due to TPA-induced free-carrier absorption (FCA). Maximum data rates of 10 Gb s^{-1} have been demonstrated in bare silicon waveguides[14], and 40 Gb s^{-1} have been achieved[15] by using a reverse-biased p–i–n diode for removing the generated carriers.

To achieve higher processing speeds, silicon may be combined with another material that has a fast electronic third-order

nonlinearity. Located just above silicon on the periodic table is the carbon atom, which can generate a multitude of compounds characterized by large delocalized electron systems. Pioneering experiments[16] have shown that optical polymers allow single-frequency modulation speeds in the terahertz range. However, the coexistence of slow and fast nonlinear dynamics has hindered ultrafast processing of broadband communication signals up to now.

Here we present the first experimental proof of ultrafast communication signal processing using silicon-based devices for transmission speeds above 100 Gb s^{-1}. The inherent limitations of silicon are overcome by using a silicon–organic hybrid (SOH) approach. In particular, we demonstrate an ultrahigh nonlinearity coefficient $\gamma \approx 1 \times 10^5$ W^{-1} km^{-1} in slotted SOH waveguides, confirming experimentally, for the first time, the record values predicted by theory[17]. We are also able to prove that FCA losses do not arise in SOH waveguides and therefore do not impose a speed limitation. The concept of SOH integration can also be applied to electro–optic devices[18–21].

The SOH waveguide structure is shown in Fig. 1a. It consists of a silicon slotted waveguide that is filled and surrounded by a nonlinear organic cladding[21,22]. Key to the device's highly nonlinear ultrafast performance is a combination of three unique advantages. First, the organic material can be developed independently from the silicon waveguide to obtain optimum nonlinear optical properties. It can be highly $\chi^{(3)}$-nonlinear without suffering from TPA and associated FCA. Second, the silicon waveguide can be optimized essentially independently from the organic material. A slotted geometry can be chosen to provide maximum electric field magnitude inside the slot. Third, using quasi-transverse-electric (quasi-TE) polarization, the electric field is enhanced in the organic material owing to the electromagnetic boundary conditions at the interface between the high-refractive-index silicon and the low-refractive-index organic. The enhancement of the horizontal field (E_x) is equal to a factor $(n_{Si}/n_{organic})^2 = 4$ for $n_{organic} = 1.8$ and $n_{Si} = 3.5$ (see Fig. 1a).

To maximize the nonlinearity coefficient $\gamma = (n_2 k_0)/A_{eff}^{(3)}$, where k_0 is the free-space wavenumber and n_2 the nonlinear refractive index (optical Kerr coefficient) of the cladding, the smallest possible effective area of nonlinear interaction $A_{eff}^{(3)}$ is required. Calculations[17] show that $A_{eff}^{(3)}$ can be smaller than 0.1 μm^2 for our cladding material with refractive indices $n_{organic} < 2$. Waveguides consisting only of the low-index organic material would be much more difficult to fabricate and cannot provide a comparable field concentration.

The SOH structure was obtained by first producing the SOI slot waveguide and then covering it by vapour deposition of highly nonlinear organic molecules. The slotted waveguides were produced on a 200-mm CMOS line using 193-nm deep-ultraviolet (DUV)

[1]Institute of Photonics and Quantum Electronics, University of Karlsruhe, 76131 Karlsruhe, Germany, [2]Photonics Research Group, Ghent University – IMEC, B-9000 Gent, Belgium, [3]Department of Physics and Center for Optical Technologies, Lehigh University, Bethlehem, Pennsylvania 18015, USA, [4]Laboratorium für Organische Chemie, ETH Zürich, Hönggerberg, HCI, CH-8093 Zürich, Switzerland. [†]Present address: Carl Zeiss AG, Corporate Research and Technology, 73447 Oberkochen, Germany. *e-mail: w.freude@ipq.uka.de; j.leuthold@ipq.uka.de
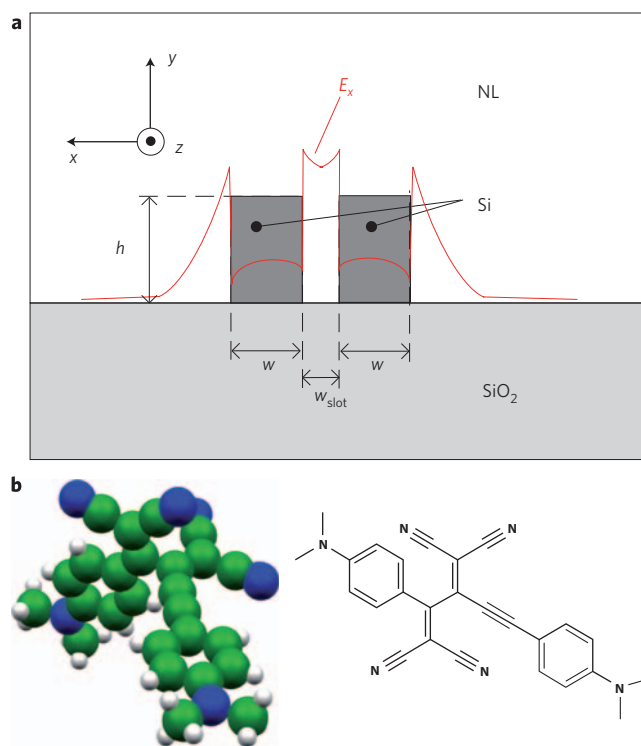
Figure 1 | Structure and organic molecule of a SOH slot waveguide.
a, Schematic of the waveguide cross-section comprising two silicon ribs on a silicon dioxide buffer layer covered by a nonlinear optical organic material (NL). The quantities w and h denote the width and the height of the ribs, and w_{slot} is the slot width. For the fundamental quasi-TE mode, the dominant (horizontal) electric field component E_x (depicted in red) is strongly enhanced within the low-index material filling the slot. **b**, Molecular structure of the vapour-deposited small molecule DDMEBT[23].

lithography and chlorine-based reactive ion etching[4]. The thickness of the SOI device layer (waveguide height) was $h = 220$ nm, and the buried oxide was 2 μm thick.

To deposit the organic cladding material, spin-coating can be used[18]. However, for third-order nonlinear interaction, the propagation loss is crucial to the functionality of the device, so it is of paramount importance to homogeneously fill the narrow slot with the organic material. We therefore used molecular beam deposition of a small molecule, DDMEBT[23] (2-[4-(dimethylamino)phenyl]-3-{[4-(dimethyl-amino)phenyl]ethynyl}buta-1,3-diene-1,1,4,4-tetracarbonitrile) to fabricate the organic cladding. The DDMEBT molecule has a non-planar geometry (shown in Fig. 1b) that promotes the formation of an amorphous supramolecular assembly without any grains or inhomogeneities. DDMEBT is part of a family of molecules with a third-order polarizability that is extraordinarily large in relation to the size of the molecule[23–25]. The organic film was ~950 nm thick, flat to the nanometre scale, and featured a large isotropic, off-resonant Kerr coefficient $n^2 \approx (1.7 \pm 0.8) \times 10^{-17}$ m^2 W^{-1} at a wavelength of 1.5 μm (ref. 23). The linear refractive index was $n = 1.8 \pm 0.1$. As can be seen in Fig. 2a, the cover layer homogeneously surrounds the waveguides, and perfectly fills the slot without forming any voids. This is probably due to the mobility of the molecules on the substrate during deposition. The high optical quality of the organic cladding is confirmed by the fact that it does not significantly affect the linear propagation loss of SOH waveguides. (See Methods for more details.)

The nonlinearity parameter γ of the SOH waveguide was obtained by measuring the conversion efficiency $\eta \propto (\gamma L_{eff})^2$ of partially degenerate four-wave mixing with a c.w. pump and signal. The quantity L_{eff} is the effective waveguide length accounting for both linear waveguide loss and group-velocity dispersion. For different samples
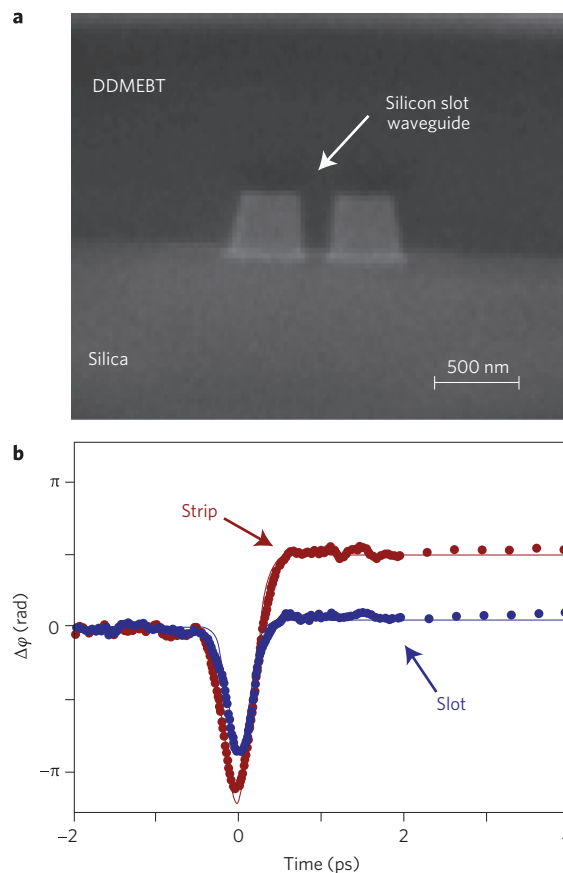

Figure 2 | Scanning electron microscope (SEM) image of the SOH waveguide and nonlinear waveguide dynamics. a, SEM image of the cross-section of the vapour-deposited organic film covering the silicon waveguide. The ability of the organic material to homogeneously fill the slot between the waveguides is a key feature of the organic cover layer and of its deposition process. **b**, Nonlinear phase dynamics of the SOH slot waveguide and of a SOH strip waveguide. The slot waveguide has an ultrafast response, whereas the strip waveguide shows the slow phase dynamics caused by TPA-generated free carriers. Dots represent measured values; thin solid line is fitted.

with nominally identical geometry, we measured[26] values between $\gamma = 104,000$ and $83,000$ W^{-1} km^{-1}, which is much larger than for holey fibres[27] ($\gamma = 1,860$ W^{-1} km^{-1}) and larger than for silicon–polymer strip waveguides[16] ($\gamma = 40,000$ W^{-1} km^{-1}) or chalcogenide fibres[28] ($\gamma = 68,000$ W^{-1} km^{-1}). (See Methods for more details.)

The nonlinear organic cladding in SOH shows an instantaneous Kerr-type response without impairment by TPA and FCA. To prove this, we compared the SOH slot waveguide of Fig. 1a with a simple DDMEBT-covered silicon strip, in which the quasi-TE mode is concentrated in the silicon core. With heterodyne pump-probe measurements[29,30] we showed that SOH slot waveguides are indeed dynamically superior to SOH strip waveguides (see Methods). Figure 2b shows the ultrafast phase response of the SOH slot waveguide, and for the SOH strip a slowly decaying phase shift of opposite sign. This is due to TPA-generated free carriers with a carrier lifetime of ~1.2 ± 0.1 ns. Although bare silicon strip waveguides can exhibit strong nonlinearities[14,17] ($\gamma > 100,000$ W^{-1} km^{-1}), free-carrier dynamics on this timescale lead to severe pattern effects in high-speed signal processing.

Finally, to prove the viability of SOH slot waveguides for all-optical processing of broadband telecommunication signals by four-wave mixing (FWM), we demonstrate demultiplexing of a 170.8 Gb s^{-1} return-to-zero (RZ) datastream to a bit rate of
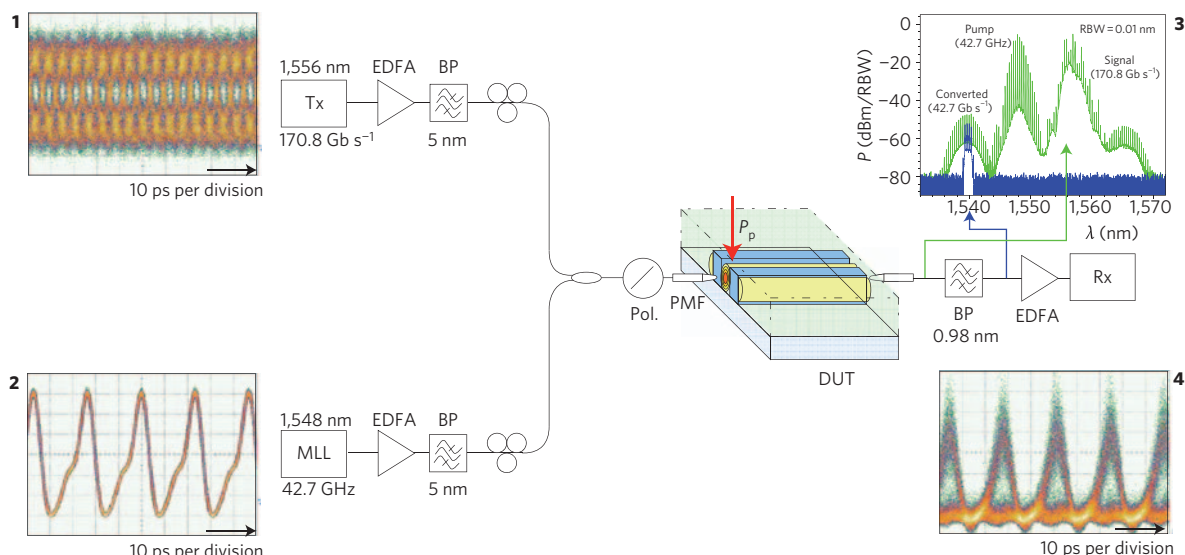
Figure 3 | Experimental set-up of the all-optical demultiplexing by four-wave mixing. Tx indicates a 170.8 Gb s^{-1} transmitter, comprising a 42.7 GHz mode-locked laser, a data modulator, an optical time-division multiplexer, and an optical delay line for synchronization. MLL indicates a mode-locked laser, EDFA an erbium-doped fibre amplifier, BP an optical bandpass filter, Pol a polarizer, PMF a polarization-maintaining fibre, DUT a device under test, Rx a receiver comprising a 120 GHz photodiode and a digital communication analyser, and RBW the resolution bandwidth. Insets: **1**, eye diagram of the 170.8 Gb s^{-1} data signal; **2**, eye diagram of the 42.7 GHz pump; **3**, the spectrum at the output of the DUT (green) and after bandpass-filtering (blue); **4**, eye diagram of the demultiplexed 42.7 Gb s^{-1} signal.

42.7 Gb s^{-1}. The set-up of Fig. 3 comprises two synchronized mode-locked fibre lasers for data and pump, both operating at repetition rates of 42.7 GHz and emitting pulses of ~3 ps full-width at half-maximum (FWHM). The 170.8 Gb s^{-1} data stream is generated by modulating the 42.7 GHz pulse train with a pseudo-random bit sequence ($2^{31} - 1$ bit), and by subsequent optical time-division multiplexing; see inset 1, Fig. 3 (eye diagram). Owing to the limited electronic receiver bandwidth, the eye diagram is distorted. Signal and pump (inset 2, Fig. 3) are amplified and coupled into an SOH slot waveguide (height $h = 220$ nm, strip width $w = 212$ nm, slot width $w_{slot} = 205$ nm, length $L = 4.0$ mm). The output signal is bandpass-filtered at the converted wavelength, amplified and detected; see inset 3, Fig. 3, for the optical spectra. There is no leakage through the filter at the pump and signal wavelengths; see Methods. Inset 4, Fig. 3 depicts the demultiplexed signal's eye diagram for an average on-chip pump power of $P_p = 16.6$ dBm (48 mW). (See Methods for more details.)

In summary, we have fabricated and characterized SOH slot waveguides using DUV lithography, standard CMOS processing, and organic molecular beam deposition. We obtained record non-linearities of about 1×10^5 W^{-1} km^{-1} in the 1.55 µm telecommunication window. By using FWM we demultiplexed a 170.8 Gb s^{-1} telecommunication signal to 42.7 Gb s^{-1}. In view of the potential for improving fibre-chip coupling as well as waveguide loss and waveguide geometry, this is a key step towards complex silicon-based photonic integrated circuits.

Methods

Waveguide fabrication. DUV lithography at 193 nm was performed on an ASML PAS5500/1100 stepper. The organic cladding was deposited in high vacuum at a pressure of 10^{-6} mbar. Powder made of the organic material was heated to 130 °C to generate a molecular beam directed onto the substrate. The growth rate amounted to ~1 nm per minute.

Using atomic force microscope (AFM) scans of the surface, we found that it was flat to the nanometre scale over micrometre lengths[23]. In addition, we took a series of SEM images while slicing the slot waveguide with a Carl Zeiss CrossBeam (focused-ion beam, FIB) system at several positions parallel and perpendicular to the waveguide axis (a perpendicular cut similar to that in Fig. 2a). No grains or voids were found.

For characterization of the slot waveguides, TE-polarized light (the dominant electric field component parallel to the substrate plane) was launched to and detected from the cleaved waveguide facets using polarization-maintaining lensed fibres. A cut-back method was applied to measure the wavelength-dependent loss of the slot waveguides and the fibre-to-chip coupling loss. For a waveguide of height $h = 220$ nm, width $w = 216$ nm and a slot width of $w_{slot} = 157$ nm, the propagation loss was $\alpha_{dB} = 1.6$ dB mm^{-1} ($\alpha = 0.37$ mm^{-1}) at a wavelength of 1,550 nm, and the corresponding fibre-to-chip coupling loss was $a_{cp} = 6.2$ dB per facet. For a reference waveguide with identical geometry but covered with SiO$_2$, the propagation loss was 1.2 dB cm^{-1} and was therefore only slightly smaller than for the DDMEBT-covered waveguide. The absence of strong scattering loss confirmed the good optical homogeneity of the DDMEBT film.

Characterization of nonlinearities. For a waveguide of geometrical length L and nonlinearity parameter γ, the conversion efficiency for degenerate FWM with c.w. signal and pump waves is given by

$$\eta = \exp(-\alpha L)\left(\gamma P_p L_{eff}\right)^2 \qquad (1)$$

where P_p denotes the on-chip pump power just after the input facet of the waveguide and α is the linear propagation loss coefficient. The effective waveguide length $L_{eff} < L$ accounts for both linear propagation loss and group velocity dispersion (GVD) and is given by

$$L_{eff} = \sqrt{1 + \exp(-2\alpha L) - 2\exp(-\alpha L)\cos(\Delta\beta L)}/\sqrt{\alpha^2 + \Delta\beta^2}$$

$$\Delta\beta = \pi c D_2 \Delta\lambda^2 / 2\lambda_p^2, \quad \Delta\lambda = |\lambda_s - \lambda_c|, \quad 2\lambda_p^{-1} = \lambda_s^{-1} + \lambda_c^{-1} \qquad (2)$$

The quantity $\Delta\beta$ represents the phase mismatch between signal wave (wavelength λ_s) and converted wave (wavelength λ_c) owing to GVD parameter D_2, c is the speed of light in vacuum, and λ_p is the wavelength of the pump. By fitting these relations to the measured data, both γ and D_2 can be extracted.

The heterodyne pump-probe set-up is described in more detail in ref. 29. The measurement relies on a Spectra Physics OPAL optical parametric amplifier, which is synchronously pumped at a repetition rate of 80.42 MHz by a Tsunami Ti:sapphire mode-locked femtosecond laser. The pulses have a FWHM duration of 120 fs and a centre wavelength of 1,550 nm. Pump, probe and reference pulses are co-polarized (TE); probe and reference pulses are marked by distinct frequency offsets using acousto-optic modulators. After having passed the waveguide, the probe and the reference pulses are superimposed, and the beat signal is detected by a lock-in amplifier, hence revealing the pump-induced phase change $\Delta\varphi$ of the probe pulses.

In the measurements of Fig. 2b, a slot waveguide with height $h = 220$ nm, width $w = 216$ nm and slot width $w_{slot} = 157$ nm was used, whereas the strip waveguide

had a height $h = 220$ nm and width $w = 375$ nm. Both waveguides had a length $L = 4$ mm, and the average on-chip pump power was -1.2 dBm. For a waveguide of length L the phase change $\Delta\varphi$ is related to the pump-induced effective refractive index change Δn_e by $\Delta\varphi = -\Delta n_e 2\pi L/\lambda$. For the ultrafast Kerr responses shown in Fig. 2b (slot), the refractive index increased ($\Delta\varphi < 0$), whereas for the strip waveguide the presence of free carriers led to a pronounced slowly decaying decrease of the effective refractive index ($\Delta\varphi > 0$). The slow effect was barely visible in the case of the slot waveguide, because it was suppressed in two ways. First, because the light is confined to the cladding material of the slot waveguide, the number of TPA-generated free carriers is much smaller than in the strip waveguide. Second, the overlap of the slot waveguide mode with the silicon core is much smaller than for the strip waveguide—only 26% of the total optical power propagates within the silicon core, whereas 60% is guided in the nonlinear cladding and 14% in the silica buffer layer. The slot mode is hence only weakly affected by the carrier-induced decrease of the refractive index in the silicon core.

It can further be confirmed that the absence of slow carrier dynamics for the SOH slot waveguides is not caused by increased surface recombination owing to a larger surface-to-volume ratio. All waveguides were produced side by side on the same chip, and hence had identical recombination rates of free carriers at the surfaces. If d is the average distance that a carrier has to diffuse (random walk) until it reaches the surface, then the effective carrier lifetime is proportional to d^2. For the strip waveguide (width 375 nm) a carrier lifetime of $\sim$1.2 ns was measured. To a first approximation, the carrier lifetime of the slot waveguide (width 216 nm) should then be 1.2 ns/$(375^2/216^2) \approx 0.4$ ns, which would be clearly visible as a slowly decaying response in Fig. 2b. As this is not the case, we conclude that, indeed, the ultrafast nonlinear response originates from the nonlinear cladding.

Transmission experiment. For the transmission experiment, two synchronized Calmar mode-locked fibre lasers were used. The optical signals were detected with a u^2t 120 GHz photodiode, and the eye diagrams were recorded with an Agilent Infiniium digital communication analyser (DCA). Except for the intrinsic low-pass behaviour of the detector and the DCA, no further filtering of the electrical signal was performed for generating the eye diagrams in Fig. 3. The slot waveguide used for the demultiplexing experiment (height $h = 220$ nm, strip width $w = 212$ nm, slot width $w_{slot} = 205$ nm) had a propagation loss of $\alpha_{dB} = 1.5$ dB mm^{-1} and a fibre-chip coupling loss of $a_{cp} = 4.1$ dB per facet at 1,550 nm. The wavelength conversion efficiency in the present experiment was approximately -32 dB. There is still a huge potential for improvement by reducing the waveguide loss and by further increasing the nonlinearity of the waveguide[17].

The eye diagram of the converted wave disappears if either the pump or the signal wavelengths are blocked at the input of the device. By varying the delay between the pump and the signal, different tributaries of the optical time-division multiplexed (OTDM) data can be demultiplexed. Similar performance is found for the different tributaries. This confirms again that the recorded eye diagram is not caused by leakage through the filters. The extinction ratio of the demultiplexed eye diagram was $\sim$7.7 dB.

The noise in the converted eye diagram is predominantly caused by amplified spontaneous emission. It can be expected that the converted signal experiences retiming due to the periodic pump pulse sequence. The FWM demultiplexing scheme preserves both phase and amplitude information and is therefore transparent with respect to the modulation format.

References

1. Tsuchizawa, T. *et al.* Microphotonics devices based on silicon microfabrication technology. *IEEE J. Sel. Top. Quantum Electron.* **11**, 232–240 (2005).
2. Lipson, M. Guiding, modulating, and emitting light on silicon—challenges and opportunities. *J. Lightwave Technol.* **23**, 4222–4238 (2005).
3. Popović, M. A. *et al.* Hitless-reconfigurable and bandwidth-scalable silicon photonic circuits for telecom and interconnect applications. Optical Fiber Communincation Conference (OFC'08), paper OTuF4 (OSA, 2008).
4. Bogaerts, W. *et al.* Compact wavelength-selective functions in silicon-on-insulator photonic wires. *IEEE J. Sel. Top. Quantum Electron.* **12**, 1394–1401 (2006).
5. Vlasov, Y. A., O'Bolye, M., Hamann, H. F. & McNab, S. J. Active control of slow light on a chip with photonic crystal waveguides. *Nature* **438**, 65–69 (2005).
6. Rong, H. *et al.* Low-threshold continuous-wave Raman silicon laser. *Nature Photon.* **1**, 232–237 (2007).
7. Espinola, R. L. *et al.* Raman amplification in ultrasmall silicon-on-insulator wire waveguides. *Opt. Express* **12**, 3713–3718 (2004).
8. Park, H. *et al.* A hybrid AlGaInAs–silicon evanescent amplifier. *IEEE Photon. Technol. Lett.* **19**, 230–232 (2007).
9. Fang, A. W. *et al.* Electrically pumped hybrid AlGaInAs–silicon evanescent laser. *Opt. Express* **14**, 9203–9210 (2006).
10. Van Thourhout, D. *et al.* A photonic interconnect layer on CMOS. European Conference on Optical Communications (ECOC'07), paper 6.3.1 (2007).
11. Koch, B. R., Fang, A. W., Cohen, O. & Bowers, J. E. Mode-locked silicon evanescent lasers. *Opt. Express* **15**, 11225–11233 (2007).
12. Park, H. *et al.* A hybrid AlGaInAs–silicon evanescent waveguide photodetector. *Opt. Express* **15**, 6044–6052 (2007).
13. Liao, L. *et al.* 40 Gbit/s silicon optical modulator for high-speed applications. *Electron. Lett.* **43**, 1196–1197 (2007).
14. Salem, R. *et al.* Signal regeneration using low-power four-wave mixing on silicon chip. *Nature Photon.* **2**, 35–38 (2008).
15. Kuo, Y.-H. *et al.* Demonstration of wavelength conversion at 40 Gb/s data rate in silicon waveguides. *Opt. Express* **14**, 11721–11726 (2006).
16. Hochberg, M. *et al.* Terahertz all-optical modulation in a silicon-polymer hybrid system. *Nature Mater.* **5**, 703–709 (2006).
17. Koos, C., Jacome, L., Poulton, C., Leuthold, J. & Freude, W. Nonlinear silicon-on-insulator waveguides for all-optical signal processing. *Opt. Express* **15**, 5976–5990 (2007).
18. Baehr-Jones, T. W., *et al.* Optical modulation and detection in slotted silicon waveguides. *Opt. Express* **13**, 5216–5226 (2005).
19. Hochberg, M. *et al.* Towards a millivolt optical modulator with nano-slot waveguides. *Opt. Express*, **15**, 8401–8410 (2007).
20. Brosi, J.-M. *et al.* High-speed low-voltage electro-optic modulator with a polymer-infiltrated silicon photonic crystal waveguide. *Opt. Express* **16**, 4177–4191 (2008).
21. Baehr-Jones, T. W. and Hochberg, M. J. Polymer silicon hybrid systems: A platform for practical nonlinear optics. *J. Phys. Chem. C* **112**, 8085–8090 (2008).
22. Almeida, V. R., Xu, Q., Barrios, C. A. & Lipson, M. Guiding and confining light in void nanostructure. *Opt. Lett.* **29**, 1209–1211 (2004).
23. Esembeson, B. *et al.* A high optical quality supramolecular assembly for third-order integrated nonlinear optics. *Adv. Mater.* **20**, 4584–4587 (2008).
24. Michinobu, T. *et al.* A new class of organic donor–acceptor molecules with large third-order optical nonlinearities. *Chem. Commun.* 737–739 (2005).
25. May, J. C., Biaggio, I., Bures, F. & Diederich, F. Extended conjugation and donor–acceptor substitution to improve the third-order optical nonlinearity of small molecules. *Appl. Phys. Lett.* **90**, 251106 (2007).
26. Koos, C. *et al.* Highly-nonlinear silicon photonics slot waveguide. Optical Fiber Communications Conference (OFC'08), postdeadline paper PDP25 (2008).
27. Leong, J. Y. Y. *et al.* A lead silicate holey fiber with $\gamma = 1860$ W^{-1} km^{-1} at 1550 nm. Optical Fiber Communications Conference (OFC'05), postdeadline paper PDP22 (2005).
28. Mägi, E. C. *et al.* Enhanced Kerr nonlinearity in sub-wavelength diameter As$_2$Se$_3$ chalcogenide fiber tapers. *Opt. Express* **15**, 10324–10329 (2007).
29. Vallaitis, T. *et al.* Slow and fast dynamics of gain and phase in a quantum dot semiconductor optical amplifier. *Opt. Express* **15**, 170–178 (2007).
30. Vallaitis, T. *et al.* Highly nonlinear silicon photonic slot waveguides without free carrier absorption related speed-limitations. Proc. 34rd European Conference on Optical Communication (ECOC'08), paper Th.2.D.6 (2008).

Acknowledgements

Additional information

Reprints and permission information is available online at http://npg.nature.com/reprintsandpermissions/. Correspondence and requests for materials should be addressed to W.F. and J.L.

Heat-assisted magnetic recording by a near-field transducer with efficient optical energy transfer

W. A. Challener*, Chubing Peng, A. V. Itagi, D. Karns, Wei Peng, Yingguo Peng, XiaoMin Yang, Xiaobin Zhu, N. J. Gokemeijer, Y.-T. Hsia, G. Ju, Robert E. Rottmayer, Michael A. Seigler and E. C. Gage

Although near-field microscopy has allowed optical imaging with sub-20 nm resolution, the optical throughput of this technique is notoriously small. As a result, applications such as optical data storage have been impractical. However, with an optimized near-field transducer design, we show that optical energy can be transferred efficiently to a lossy metallic medium and yet remain confined in a spot that is much smaller than the diffraction limit. Such a transducer was integrated into a recording head and flown over a magnetic recording medium on a rotating disk. Optical power from a semiconductor laser at a wavelength of 830 nm was efficiently coupled by the transducer into the medium to heat a 70-nm track above the Curie point in nanoseconds and record data at an areal density of $\sim$375 Tb m^{-2}. This transducer design should scale to even smaller optical spots.

Light can be focused by conventional far-field optics to a spot that is limited by diffraction to $\sim$0.5 λ/NA where λ is the wavelength and NA is the numerical aperture of the lens. The near-field scanning optical microscope[1], on the other hand, can achieve a resolution of 100 nm or better. Near-field microscopy typically uses either tapered optical fibres or hollow silicon cantilevers with a very small aperture that is scanned across the sample, but the optical throughput[2,3] is in the order of 1×10^{-4} to 1×10^{-5}. Using concentric grooves around an aperture in an aluminium film can substantially enhance the throughput; this has recently been used to expose marks in photoresist with a linewidth of 80 nm (ref. 4). Apertureless microscopy has achieved sub-20-nm optical resolution[5] by focusing a laser beam onto a sharp metallic tip, which concentrates the optical field onto the sample.

The storage density of hard disk drives has doubled every three years since their introduction in 1955. Several major technology advances, including the development of thin-film media and recording heads, giant magnetoresistive readers, and perpendicular recording, have enabled the current areal density of 750 Tb m^{-2}, which is about half the theoretical limit for conventional magnetic recording materials. As the magnetic grain size is reduced to increase the storage density, the grains may become superparamagnetic and their magnetic state thermally unstable[6]. Materials with a large magnetic anisotropy, such as L1$_0$ FePt (ref. 7), can support grains as small as 2 to 3 nm in diameter and storage densities[8] up to 155 Pb m^{-2}. However, the coercivity of high-anisotropy materials is greater than the magnetic field that can be generated by a recording head.

Heat-assisted magnetic recording (HAMR) overcomes this problem by heating the medium above its Curie point during recording to reduce its coercivity to zero[8]. Optical energy must be efficiently delivered and confined to a spot in the medium that is much smaller than the diffraction limit so that neighbouring tracks are not heated. Heating and cooling of the medium must occur within $\sim$1 ns in order to achieve the necessary data rates, to generate a large thermal gradient for sharp bit edge definition, and to ensure that the recorded data are thermally stable during cooling to ambient.

A planar solid immersion mirror (PSIM) is a parabolically shaped waveguide with a NA much larger than 1 that can focus light to $\sim$$\lambda$/4 (ref. 9). HAMR has been demonstrated with PSIMs in integrated recording heads at storage densities of $\sim$230 Tb m^{-2} at a wavelength of 488 nm (refs 10 and 11), and at densities of $\sim$80 Tb m^{-2} at a wavelength of 830 nm. Nevertheless, much smaller optical spots are necessary for HAMR to exceed the current storage densities.

Results

The near-field transducer. Surface plasmons (SPs) are collective oscillations of surface charge that are confined to an interface between a dielectric and a metal. When SPs are resonantly excited by an external optical field, the field amplitude in the vicinity of the surface may be orders of magnitude greater than that of the incident field. Moreover, the region of enhanced field may be tightly confined to a spot much smaller than the incident wavelength. Gold is a suitable plasmonic material for wavelengths longer than $\sim$700 nm as it is chemically inert with a relatively high melting point. At shorter wavelengths the electronic d-band transitions damp the SP effect.

A gold near-field transducer (NFT) that is excited at a SP resonance can couple light even more efficiently into a nearby medium by including a sharp tip in its design to take advantage of the lightning rod effect[12,13]. The electric field can also be enhanced in a narrow gap between two resonant nanoparticles[14,15]. A NFT design[16] that combines these enhancement mechanisms is shown in Figs 1a and 4a and is called a 'lollipop' transducer for obvious reasons. The NFT is located at the focus of a PSIM as shown in Fig. 1b, and at resonance the surface charge oscillates along the length of the lollipop peg to generate an electric field at the tip of the peg that couples energy into the medium. The peg provides the lightning rod effect for field confinement. A plasmonic metal beneath the recording layer acts as both a heat sink and an image plane for the electric field. The recording layer is effectively within the gap of two nanoparticles, the NFT and its image, resulting in a substantial enhancement in coupling efficiency and further confinement of the electric field.
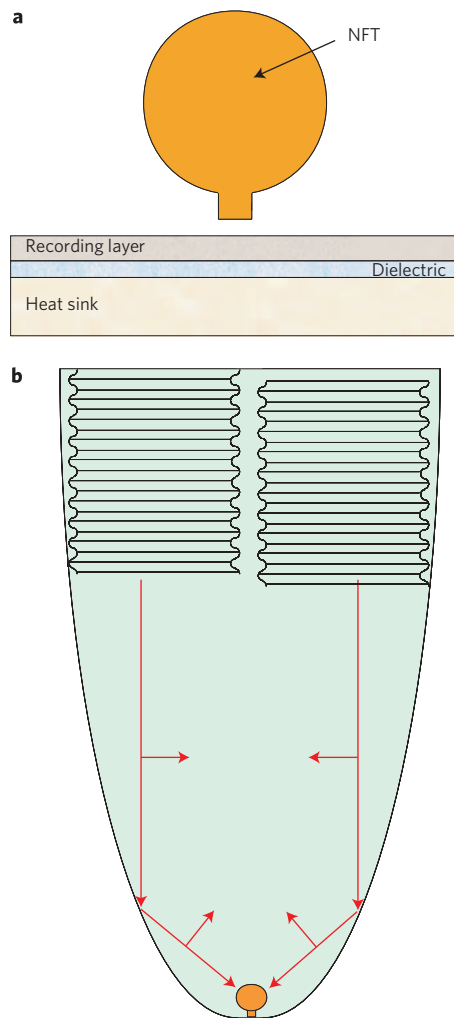
Seagate Technology, 1255 Waterfront Place, Pittsburgh, Pennsylvania 15222, USA. *e-mail: william.a.challener@seagate.com

Figure 1 | Diagram of the NFT and its position in the PSIM. a, Expanded
view of the NFT showing its vertical position with respect to the recording
medium. The medium is modelled as 12.5 nm Fe, 5 nm MgO and 50 + nm
Cu. The 7.5-nm gap between the NFT and the medium is modelled with an
effective index slightly greater than air to include the effect of the lubricant
and carbon overcoats. **b,** A planar solid immersion mirror with a dual offset
grating used to focus a waveguide mode onto the lollipop NFT. The electric
field for the TE mode is shown, which generates a longitudinal (vertical)
field at the focus.

The incident light must be polarized along the vertical axis of the
NFT to excite the proper SP resonance. The coupling grating at the
top of the PSIM is divided into two halves that are vertically offset by
half a period with respect to each other. There is a π-phase shift
between the transverse electric (TE) waveguide modes launched
on either side of the PSIM. When the modes combine at the
focus, the net field is longitudinally polarized as shown in Fig. 1b.
This grating/PSIM is the planar equivalent of radially polarized
light, for which a longitudinal field is also obtained at the focus[17,18].

Theoretical optimization of the transducer. NFTs have been
theoretically characterized in the literature in a variety of different
ways. Because a metallic medium in proximity to a NFT can
strongly affect its resonant behaviour, it is essential that the
medium be included in the model. A NFT that exhibits a large
field enhancement or throughput in free space may nevertheless
perform quite poorly as a HAMR NFT[19]. An appropriate figure of
merit (FOM) for theoretically optimizing the NFT design is the
fraction of total incident focused optical power that is dissipated

within a specific region of the medium. A 70×70 nm^2 region in
the recording layer is chosen for our finite-difference time-
domain (FDTD) simulations[20–22].

The lollipop NFT is a composite design obtained by combining a
circular disk with a peg. The disk dimensions are optimized to func-
tion as an antenna for the incident light, resonating at the chosen
wavelength while funnelling energy into the peg for confined trans-
fer to the recording medium. The composite lollipop NFT is about
four times more efficient than a straight peg NFT by itself.

A rather complex optimization process is required to find the size
and position of the lollipop NFT within the waveguide that maxi-
mizes the FOM. The field intensity within the medium decays expo-
nentially as the distance to the NFT increases (see Supplementary
Fig. S1). The gap between the bottom of the NFT and the top of
the recording layer for our simulations is 7.5 nm, consistent with
read back signal requirements at storage densities of 1.5 Pb m^{-2}
(1 Tb in^{-2}). The best coupling at a wavelength of 870 nm occurs
for our waveguide when the NFT is placed about 20 nm outside
the core. In this case, the peak field intensity in the gap is ∼2,000
times larger than that of the incident focused field intensity, as
shown in Fig. 2c, and is ∼4% larger at the edges of the peg than
under the centre of the peg. The peak FOM for a NFT that is
30 nm thick is ∼8%, as shown in Fig. 2a, and is orders of magnitude
greater than the coupling efficiency of simple apertures with diam-
eters of the same dimensions as the peg. The simulated field intensity
in the centre layer of the recording medium, which is proportional to
the dissipated power in the medium, is shown in Fig. 2b.

As the peg width is reduced, the optical spot size in the medium
is also reduced and the peak field intensity within the medium
increases. Therefore, this NFT should perform even better at
higher storage densities and smaller optical spots.

In conventional disk drives the head-to-medium spacing is con-
trolled by localized electrical heating of the recording head. This
causes differential thermal expansion of the head (see
Supplementary Fig. S2). In a HAMR head, the additional heat
from absorbed laser light causes the NFT to protrude towards the
surface of the disk during recording by several nanometres[8]. The
protrusion increases the coupling efficiency, but it must be carefully
controlled so that the NFT does not contact the disk surface. The
surface roughness of the recording medium must also be sufficiently
small not to cause significant variations in coupling efficiency.

The edge of a recorded mark occurs at that point on the track in
the medium between the NFT and the recording pole for which
the applied magnetic field equals the coercivity of the medium at
the local temperature. Owing to the aggressive heat sinking of the
medium, the mark edge is located closer to the NFT than to the
recording pole. Therefore, the magnitude of the magnetic field at
the recording position is smaller than the field at the edge of the
pole. Reducing the spacing between the NFT and recording pole
can increase the magnetic field within the hot spot, but this also
reduces the NFT efficiency as the proximity of the lossy metallic
pole damps the NFT resonance.

Fabrication of the recording head. An integrated recording head is
shown in Fig. 3. The complete optical system includes two coupling
gratings at the top of the device to insert a free-space laser beam into
both sides of the PSIM waveguide, a PSIM to focus the TE
waveguide mode onto the NFT, and the lollipop NFT itself. The
input coupling grating has a groove depth of ∼60 nm with a
period of 750 nm for efficiently coupling[23] of a 35-μm-diameter
incident optical spot at a wavelength of 830 nm and an angle of
incidence of 40°. A gold reflector beneath the lower cladding layer
of the waveguide enhances the efficiency of the grating by
reflecting the incident beam back to the grating for a second pass.
The lower cladding thickness of 790 nm ensures the correct phase
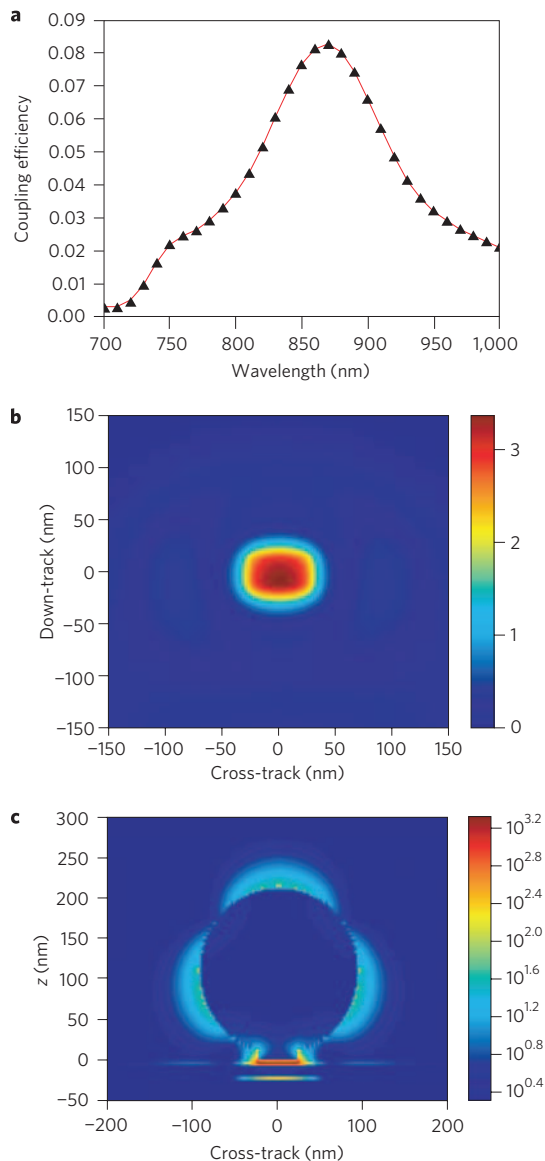of the reflected beam at the grating. Approximately 50% of the

Figure 2 | NFT coupling efficiency and field intensity. a, Coupling efficiency of the lollipop NFT versus wavelength into a 70×70 nm^2 region of an Fe-like medium. **b,** Profile of $|E|^2$ field intensity within the centre of the recording layer at the resonance wavelength. **c,** Profile of the $|E|^2$ field intensity through a cross-section of the NFT.

Figure 3 | Integrated recording head. a, Schematic of the integrated recording head incorporating the HAMR optics: a grating coupler, a PSIM waveguide and a lollipop NFT, as well as the magnetic components including the recording pole and TMR reader. **b,** Optical image of the recording head pressed against the glass slide. Scale bar, 50 μm.

incident light is coupled into the planar waveguide, which is composed of a 125-nm core of Ta$_2$O$_5$ with index 2.15, surrounded by an Al$_2$O$_3$ cladding with index 1.65. The effective index of the TE mode in the waveguide is 1.80. The diameter of the lollipop disk is ~200 nm, the thickness of the disk and peg ~22 nm, the length of the peg ~15 nm and the width of the peg ~50 nm. The imaginary part of the refractive indices for the waveguide layers must be less than ~1×10^{-5} to ensure minimal energy loss of the propagating beam.

The lollipop NFT was integrated with a recording pole and a tunnelling magnetoresistive reader on a recording head with a patterned air bearing surface designed so the head would fly over the surface of the magnetic recording disk rotating at 2,700 rpm or a linear speed of 7.2 m s^{-1}. The reader had a physical width of 55 nm. A lithographically defined gold lollipop NFT is shown in Fig. 4a and the air bearing surface of the recording head in the region of the NFT and recording pole is shown in Fig. 4b. The NFT-to-pole spacing was ~40 nm. The

width of the recording pole on the side next to the NFT was ~310 nm. As seen in Fig. 4b, the peg of the NFT was not centred below the recording pole due to lithographic misalignments during fabrication, but the relatively large width of the recording pole ensures that the applied field is present in the region of the medium heated by the NFT.

Most of the NFT dimensions are determined by thin-film deposition or lithographic processes and can be controlled with high precision. The diameter of the disk in the lollipop or the refractive index of the surrounding dielectric can be reduced to shift the resonance to shorter wavelengths. The length of the peg of the lollipop is also affected by the lapping process and must be controlled to within ± 10 nm to ensure an adequate coupling efficiency and optical spot size.

Fabrication of the recording medium

The recording medium was a 7.5-nm layer of FePt with a coercivity of 20.2 kOe, which was too large for a conventional perpendicular recording head to switch. Various underlayers were deposited on the substrate for epitaxial growth of the magnetic grains in the recording layer in the L1$_0$ crystalline structure. The medium did

Figure 4 | SEM images of the NFT. a, SEM image of the gold lollipop NFT with a 50-nm peg width. The disk diameter in this image is ∼350 nm. The distance between the dashed lines is 0.050 nm. **b**, SEM image of the NFT peg cross-section (small rectangle) and recor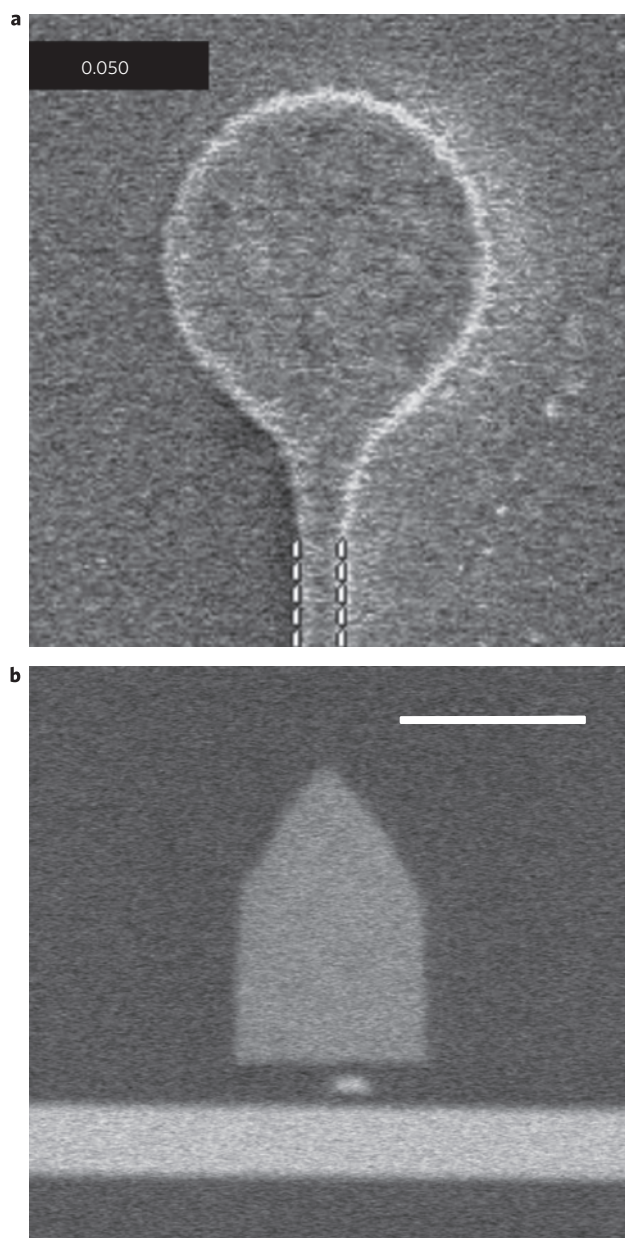ding pole (trapezoid) from the air-bearing surface. The horizontal white band is the 125-nm Ta_2O_5 core. The peg width is ∼60 nm and the thickness ∼22 nm. Scale bar, 300 nm.

not incorporate a plasmonic image plane layer, thereby somewhat reducing the coupling efficiency, broadening the optical spot, and shifting the resonance peak to slightly shorter wavelengths from the modelled results. The surface of the disk had an r.m.s. roughness substantially less than 0.5 nm and was coated with a proprietary liquid lubricant with a decomposition temperature above 670 K.

Recording results. During recording, a constant 80 mW of laser power at a wavelength of 830 nm was incident upon the coupling grating, and the electrical heater current was adjusted to maintain a constant head-to-medium spacing of ∼15 nm. This spacing corresponded to a physical air gap of ∼2 nm between the bottom of the carbon overcoat on the recording head and the top of the lubricant on the disk. Differential thermal expansion from laser
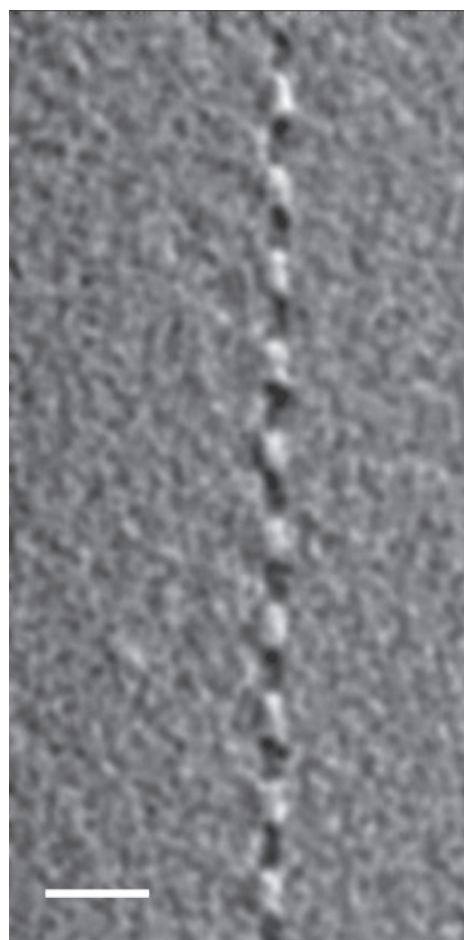
Figure 5 | MFM image of a recorded track. The track width is ∼70 nm. Scale bar, 300 nm.

heating may have also caused a small protrusion of the NFT, reducing the NFT-to-medium spacing during recording as previously described. The coils around the recording pole were driven with 59 mA of current that was modulated at the data rate.

A magnetic force microscope (MFM) image of a recorded track is shown in Fig. 5. Because the recording layer is so thin, the magnetic field is very small and the image is rather noisy. The cross track signal for three adjacent recorded tracks with separations of 80 nm is shown in Fig. 6. An autocorrelated signal-to-noise ratio (ACSN) for a pseudo-random bit sequence, in which the background electronic noise was removed by averaging, was 15.5 dB for a full-width at half-maximum (FWHM) track width of 74 nm and a down track linear density of 36 nm per flux change. This track width is much smaller than the region of the medium that experiences the full applied magnetic field from the 310-nm-wide recording pole, and is consistent with a track squeeze experiment on a different head and recording medium as shown in Supplementary Fig. S3. In that experiment, the ACSN of a central recorded track was measured as neighbouring tracks were recorded on either side of it with varying offsets from the central track. Not until the track offset dropped below 80 nm was a sudden drop in ACSN measured. Therefore, it is reasonable to estimate an areal density of ∼375 Tb m^{-2} for these HAMR results by multiplying the measured FWHM track width by the minimum bit length for which an acceptable signal-to-noise ratio of at least 15 dB was obtained.

The HAMR heads had lifetimes of up to several tens of track recordings. Thermal modelling indicates that the NFT temperature

Figure 6 | Cross track scan of recorded data. Three tracks are recorded with an 80-nm offset.

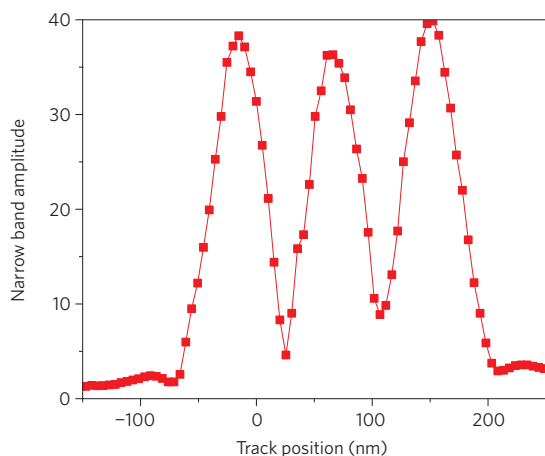may rise by several hundred degrees, but it remains well below the melting point of gold. The failure mode may be repeated thermal cycling of the NFT, the surrounding dielectrics and the recording medium. Appropriate materials engineering and thermal heat sinking can address this issue.

Discussion

A NFT has been designed that can efficiently couple optical energy into an absorptive medium in a region much smaller than the diffraction limit. The NFT has been demonstrated by incorporating it into a recording head to enable recording onto high-coercivity FePt media on a rotating disk. The recorded track width of ~70 nm was comparable to the width of the NFT peg and much narrower than either the recording pole or the wavelength of the incident laser beam, confirming the operation of the NFT. The Curie point of the medium was 650 K. Therefore, the medium was heated by ~350 °C or more within ~1 ns, evidence of the high coupling efficiency. The arrangement of the rotating disk at high speed with an air gap also confirms that there was no thermal transport by contact between the NFT and the medium. Future devices will include narrower pegs and additional optimization of both the NFT and the medium. It is estimated that the spot size can be reduced by up to 50% with improved coupling efficiency by including a copper heat sink in the recording medium. The gap between the NFT and the recording layer must also be reduced at higher storage densities to obtain a sufficient read back signal, and this smaller gap will significantly improve the efficiency of the NFT. Improving the thermal design of the recording medium and the coupling efficiency of the grating can also reduce the optical power required for recording, although the laser power used for this demonstration is already substantially less than that used in high-speed CD-R/RW disk drives. Other engineering challenges include thermal management of the head, lubricant and medium, acceptable process tolerances for high manufacturing yields, and further reduction in the magnetic grain size. However, these initial results show that it is possible to deliver optical energy to a metallic medium with relatively high efficiency in the near field confined to spot sizes an order of magnitude or more below the wavelength of light, and suggest that HAMR will provide the future technology for continued increases in magnetic disk drive storage density.

References

1. Betzig, E., Trautman, J. K., Harris, T. D., Weiner, J. S. & Kostelak, R. L. Breaking the diffraction barrier: Optical microscopy on a nanometric scale. *Science* **251,** 1468–1470 (1991).
2. Ohtsu, M. & Hori, H. *Near-Field Nano-Optics* 129 (Kluwer, 1999).
3. Minh, P. N., Ono, T., Tanaka, S. & Esashi, M. High throughput aperture near-field scanning optical microscopy. *Rev. Sci. Instrum.* **71,** 3111–3117 (2000).
4. Srituravanich, W. *et al.* Flying plasmonic lens in the near field for high-speed nanolithography. *Nature Nanotech.* **3,** 733–737 (2008).
5. Sánchez, E. J., Novotny, L. & Xie, X. S. Near-field fluorescence microscopy based on two-photon excitation with metal tips. *Phys. Rev. Lett.* **82,** 4014–4017 (1999).
6. Lu, P. L. & Charap, S. H. Magnetic viscosity in high-density recording. *J. Appl. Phys.* **75,** 5768–5770 (1994).
7. Weller, D. & Moser, A. Thermal effect limits in ultrahigh-density magnetic recording. *IEEE Trans. Magn.* **35,** 4423–4439 (1999).
8. Kryder, M. H. *et al.* Heat assisted magnetic recording. *Proc. IEEE* **96,** 1810–1835 (2008).
9. Challener, W. A., Mihalcea, C., Peng, C. & Pelhos, K. Miniature planar solid immersion mirror with focused spot less than a quarter wavelength. *Opt. Exp.* **13,** 7189–7197 (2005).
10. Peng, C., Mihalcea, C., Büchel, D., Challener, W. A. & Gage, E. C. Near-field optical recording using a planar solid immersion mirror. *Appl. Phys. Lett.* **87,** 151105 (2005).
11. Seigler, M. A. *et al.* Heat assisted magnetic recording with a fully integrated recording head. *Proc. SPIE* **6620,** 66200P (2007).
12. Liao, P. F. & Wokaun, A. Lightning rod effect in surface enhanced Raman scattering. *J. Chem. Phys.* **76,** 751–752 (1982).
13. Martin, Y. C., Hamann, H. F. & Wickramasinghe, H. K. Strength of the electric field in apertureless near-field optical microscopy. *J. Appl. Phys.* **89,** 5774–5778 (2001).
14. Aravind, P. K., Nitzan, A. & Metiu, H. The interaction between electromagnetic resonances and its role in spectroscopic studies of molecules adsorbed on colloidal particles or metal spheres. *Surf. Sci.* **110,** 189–204 (1981).
15. Moskovits, M. Surface-enhanced spectroscopy. *Rev. Mod. Phys.* **57,** 783–826 (1985).
16. Challener, W. A. Transducer for heat assisted magnetic recording. US patent 7,272,079 (2007).
17. Quabis, S., Dorn, R., Eberler, M., Glöckl, O. & Leuchs, G. Focusing light to a tighter spot. *Opt. Commun.* **179,** 1–7 (2000).
18. Scully, M. O. & Zubairy, M. S. Simple laser accelerator: Optics and particle dynamics. *Phys. Rev. A* **44,** 2656–2663 (1991).
19. Challener, W. A., Gage, E., Itagi, A. & Peng, C. Optical transducers for near field recording. *Jpn J. Appl. Phys.* **45,** 6632–6642 (2006).
20. Taflove, A. & Hagness, S. C. *Computational Electrodynamics: the Finite-Difference Time-Domain Method* (Artech House, 2000).
21. Kunz, K. S. & Luebbers, R. J. *The Finite Difference Time Domain Method for Electromagnetics* (CRC Press, 1993).
22. Challener, W. A., Sendur, I. K. & Peng, C. Scattered field formulation of finite difference time domain for a focused light beam in dense media with lossy materials. *Opt. Exp.* **11,** 3160–3170 (2003).
23. Peng, C. & Challener, W. A. Input-grating couplers for narrow Gaussian beam: influence of groove depth. *Opt. Exp.* **12,** 6481–6490 (2004).

Additional information

Supplementary Information accompanies this paper at www.nature.com/naturephotonics. Reprints and permission information is available online at http://npg.nature.com/reprintsandpermissions/. Correspondence and requests for materials should be addressed to W.A.C.

A gigahertz-bandwidth atomic probe based on the slow-light Faraday effect

Paul Siddons*, Nia C. Bell, Yifei Cai, Charles S. Adams and Ifan G. Hughes

The ability to probe quantum systems on short timescales is central to the advancement of quantum technology. Here we show that this is possible using an off-resonant dispersive probe. By applying a magnetic field to an atomic vapour the spectra of the group index for left and right circularly polarized light become displaced, leading to a slow-light Faraday effect that results in large dispersion and high transmission over tens of gigahertz. This large frequency range opens up the possibility of probing dynamics on a nanosecond timescale. In addition, we show that the group index enhances the spectral sensitivity of the polarization rotation, giving large rotations of up to 15π rad for continuous-wave light. Finally, we demonstrate dynamic broadband pulse switching by rotating a linearly polarized nanosecond pulse by $\pi/2$ rad with negligible distortion and transmission close to unity.

The phenomenon of reduced optical group velocity (slow light) is a topic of burgeoning interest[1]. In a slow-light medium, the group refractive index n_g (the ratio of the speed of light *in vacuo* to the pulse velocity) is many orders of magnitude larger than the phase index n. An optical pulse therefore propagates much more slowly than a monochromatic light beam. Large group indices of $\sim 1 \times 10^7$ are achievable in resonant optical processes such as electromagnetically induced transparency (EIT), accompanied by a refractive index that is of the order of unity[2]. Slow light has also been studied in off-resonant optical systems, using Doppler-broadened absorption resonances[3–5]. In such systems, group indices of $\sim 1 \times 10^3$ are achievable, with gigahertz pulse bandwidths. This broad bandwidth allows large fractional pulse delays of up to 80 (ref. 4). Delaying pulses by more than their widths has applications in data synchronization and qubit operations for quantum computing[6]. Other interesting applications of slow light include light storage[7–9] and interferometry. Slow-light interferometry has been demonstrated using both monochromatic light sources[10,11], where the large dispersion associated with a slow-light medium results in greater phase sensitivity, and polychromatic light, where the large pulse delays can increase the resolution of a Fourier transform interferometer by orders of magnitude[12].

For the case of off-resonant atomic systems (where detuning from resonance is more than twice the resonance linewidth, including inhomogeneous broadening), dispersive effects dominate over absorption. This arises because the real part of the susceptibility is inversely proportional to detuning, whereas the imaginary part is inversely proportional to the square of detuning. The frequency dependence of the dispersion also means that, in general, a large bandwidth is available for dispersive effects, and consequently off-resonance dispersive probes can achieve a fast time response. Many experiments in quantum information currently call for faster probes, such as fast quantum gates based on Rydberg atoms[13,14]. Off-resonant dispersion probing also has the advantage of being less invasive than resonant absorption, leading to the possibility of a 'weak' measurement[15,16].

One example of a dispersive response is the Faraday effect, in which a magnetic field applied parallel to the direction of light propagation induces the medium to respond differently to left and right circularly polarized light (circular birefringence), leading to the
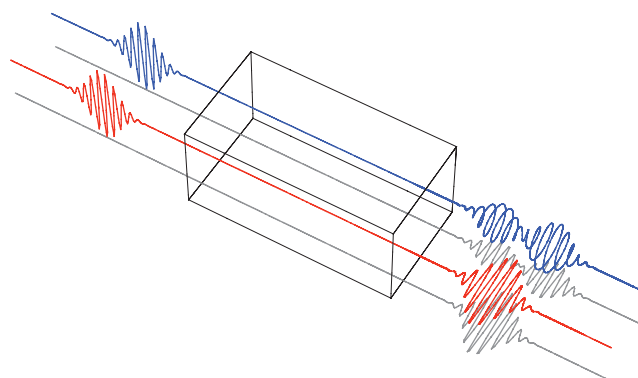
Figure 1 | Illustration of the Faraday effect for pulsed light. A representation of two pulsed electric fields, propagating from left to right along the z-axis. The other axes show the electric field magnitudes E_x and E_y. The box marks the position of the vapour cell where the magneto-optical effect occurs. Both input beams are linearly polarized along the vertical axis. The two cases correspond to different values of either the detuning, magnetic field or atomic density. The red beam remains linear as its polarization angle is rotated on exiting the medium, but the blue beam is split into two pulses of left and right circular polarization.

rotation of the linearly polarized input beam. Circular birefringence produces a relative phase shift, $\Delta\phi$, between circular field components, with spectral dependence $d(\Delta\phi)/d\omega$ (see Methods). The shift and its spectral dependence are due to the differential phase and group refractive indices, respectively, that is, the difference between the indices of σ^+ and σ^- transitions. The effect of a relative phase shift is to rotate the polarization angle of the linear input by an amount $\theta = \Delta\phi/2$. The resonant Faraday effect and magneto-optical effects have been studied extensively over the past century[17]. In this paper, we combine the large bandwidth of off-resonance slow-light media with the Faraday effect, providing a high-bandwidth dispersive probe for atomic systems. Although the off-resonant Faraday effect has been used to probe semiconductor spin ensembles[18] and quantum dots[19], in atomic systems it has mainly been studied in the context of narrowband filtering[20]. We begin by examining the

Department of Physics, Durham University, South Road, Durham DH1 3LE, UK. *e-mail: paul.siddons@durham.ac.uk

225

Figure 2 | Schematic of the experimental apparatus. The output of an external cavity diode laser (ECDL) is split by a polarization beamsplitter (PBS), providing both c.w. (blue) and pulsed (red) light. Optical pulses are generated using a Pockels cell (PoC). The c.w. light is attenu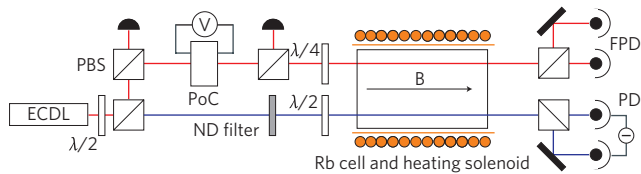ated with a neutral density (ND) filter. Waveplates (λ/2 and λ/4) control the polarization of both beams before they pass through the vapour cell. The two orthogonal linear components of the pulse are collected on separate fast photodiodes (FPD), and the two components of the c.w. beam are collected on a differencing photodiode (PD).

behaviour of light in regimes of high and low dispersion, experimentally measuring optical pulse propagation and splitting. Next we show the increased spectral sensitivity of the Faraday effect, owing to the use of a slow-light medium, and finally we demonstrate controlled rotation of a nanosecond pulse.

Results

Propagation of optical pulses. The effects of the slow-light Faraday effect on pulse propagation are illustrated in Fig. 1. For a small relative group index the pulse retains its shape, with its linear polarization rotated by an amount dependent on the relative phase index. If the relative group index is larger, the pulse splits into two spatially (and temporally) separated circular components of opposite chirality. By varying the relative refractive indices it is possible to switch dynamically between split or rotated pulses (and also control the magnitude of this rotation). We show that this is possible by changing a single experimental parameter.

The experimental setup used to demonstrate the slow-light Faraday effect is shown in Fig. 2 and described in the Methods. We begin by showing the absorption spectrum of a vapour cell over a broad frequency range for a few temperatures in Fig. 3a. At room temperature four absorption lines are seen, corresponding to the Rb D_1 hyperfine transitions $F = 2 \rightarrow F' = 1, 2$ and $F = 1 \rightarrow F' = 1,$ 2 for the lower/higher frequency features, respectively. Owing to Doppler broadening, at higher temperatures each pair of lines merges into one. The third line arises owing to the presence of ^{85}Rb in the cell; at a concentration of 1% it is much weaker than the ^{87}Rb transitions and hence not visible at room temperature. The dispersion spectrum corresponds to a sum of Doppler-broadened dispersion lineshapes associated with each absorption line. The group index is given by the derivative of the refractive index. In the wings of the resonance (detuning of order 10 Doppler widths) the group index is $\sim 1 \times 10^2$ at 150 °C and is highly sensitive to changes in temperature or frequency.

The slow-light effect is illustrated in Fig. 3b, where a pulse centred between two absorption lines is delayed by more than its width, as has been observed in earlier works[3-5]. A far off-resonant pulse is shown in Fig. 3c–e. In Fig. 3d is shown the effect of applying a magnetic field along the propagation direction. In this case the pulse is split into a double pulse. By using a λ/4 waveplate it is possible to observe the magneto-optic effect on the $\sigma^{\pm}$ transitions individually (Fig. 3e). Comparison of Fig. 3d and e shows that the linearly polarized pulse is split into its two circular component (illustrated schematically in Fig. 1). This effect was first observed by Grischkowsky[21] in a 1-m-long cell at 140 °C with an 8.5 kG pulsed magnetic field, in which a time separation of 26 ns was recorded, with a σ^- velocity of $c/9$ (compared with our observations of 3.5 ns and $c/37$, respectively). Although Grischkowsky achieved significant pulse separation (using a much longer cell
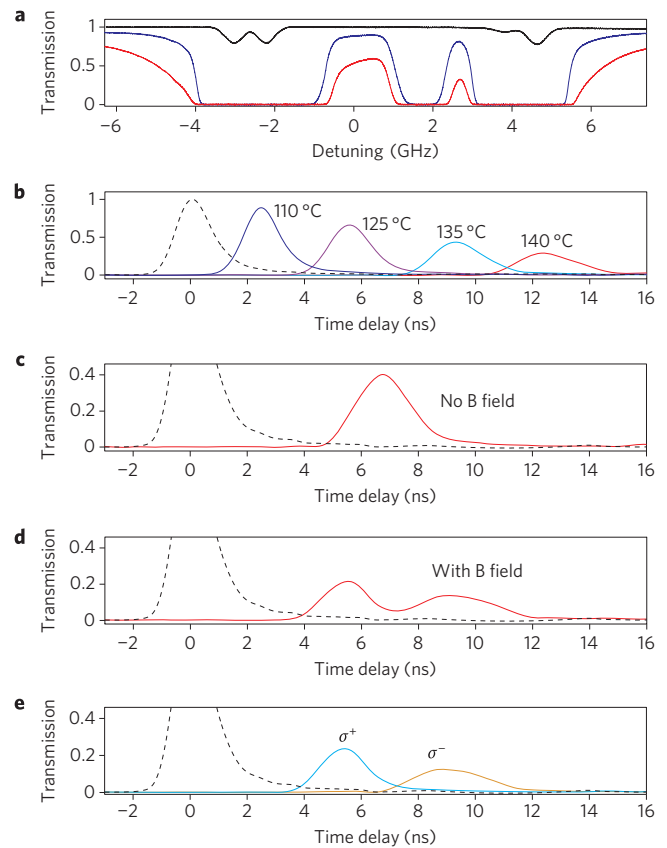

Figure 3 | Optical pulse propagation in a slow-light medium.
a, Transmission as a function of detuning from D_1 line-centre[22] for a c.w. beam through a vapour cell at room temperature (black curve), 115 °C (blue) and 150 °C (red). **b–e**, Propagation of an input 1.5-ns pulse. Transmission/delay are relative to a non-interacting reference pulse (dashed). Pulse form (**b**) at various temperatures for a pulse centred at zero detuning. Pulse (**c**) detuned to ~-6 GHz at a temperature of ~165 °C. A magnetic field of ~360 G is applied to the linearly polarized pulse in plots **d** and **e**. Noise in the data is reflected by the line thickness. B field is magnetic field.

and higher field than our experiment) he did not investigate Faraday rotation of the pulses. Later in this article we demonstrate that the large bandwidth available to the off-resonant Faraday effect enables the rotation of broadband pulses (as shown by the red beam in Fig. 1).

Spectral dependence of polarization rotation. The effect of an applied magnetic field on c.w. spectroscopy is as dramatic as the effect on pulse propagation. In Fig. 4a the conventional Doppler-broadened transmission signal is seen to oscillate between zero and the zero-field transmission when a modest field is applied. This is a consequence of polarization rotation due to the Faraday effect. Large rotations of greater than π rad are seen close to resonance, and even at detunings of many gigahertz the difference in transmission is noticeable. The rapid oscillation in the polarization as a function of frequency has a number of applications, such as a polarization switch, optical isolator or narrowband filter[20]. By using isotopically pure Rb cells one could realize a device that rotates the polarization for light of a particular frequency that is in the absorption wings of one isotope, but is resonant with the other. For example, using a ^{85}Rb vapour cell one can produce a Faraday rotator that works at the resonance frequency of ^{87}Rb or vice versa. Such applications will be the focus of future work. The experimental data are compared to the predictions of a theoretical model presented in ref. 22 in Fig. 4b.
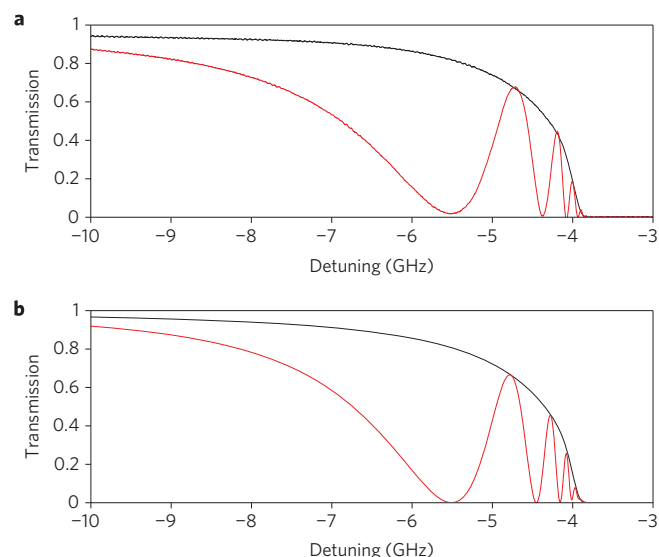
Figure 4 | Continuous-wave propagation in a slow-light medium.
Transmission of the horizontal component of the c.w. beam through the vapour cell at 136 °C. The black curve is for zero applied magnetic field and the red for a field of ∼50 G. **a**, Experimentally measured data. **b**, Results from theoretical model.

The theoretical model assumes a linear Zeeman response to the applied field. In this regime the model predicts both the Doppler-broadened lineshape, and the number and positions of the magneto-optically induced oscillations.

Refractive-index measurements. As the magnetic field of the cell is increased further, the number of oscillations increases rapidly. Figure 5 shows experimental data collected using a balanced polarimeter (see Methods), where the difference signal of vertical and horizontal polarizations is recorded. In this case over 30 oscillations are observed before one reaches a detuning sufficiently small that the medium is optically thick. These large rotations are useful for applications where a high sensitivity is required.

The large number of oscillations observed in Fig. 5 arises from the same phenomenon that enhances the spectral response in a slow-light interferometer[10] (see Methods). A powerful property of the polarimetry signal is that it allows a direct readout of the differential refractive and group indices. The signal tends to be zero at large negative detuning (not shown) and each subsequent zero corresponds to a π phase shift between the left and right circular components. This phase difference, $\Delta\phi$, is plotted in Fig. 5b. Note that the first zero crossing (corresponding to a $\pi/2$ rotation) occurs at a detuning of ∼−10 GHz where the absorption is less than 1%. At temperatures of order 200 °C, the first zero shifts out to beyond −50 GHz, that is, ∼100 Doppler linewidths. The phase obtained from the zero crossing is used to determine the differential index, which is plotted in Fig. 5c. Similarly, the differential group index is determined by the frequency spacing of the zero crossings and is shown in Fig. 5d.

Broadband pulse rotation. It can be seen in Fig. 5b that far from resonance the relative phase evolves slowly with detuning, in particular for detunings greater than −8 GHz, where $|\Delta\phi| < 2\pi$. For a linearly polarized pulse centred in this region with gigahertz bandwidth, the phase variation across its spectrum is sufficiently low that the polarization of the pulse as a whole can be rotated by a large angle. This broadband rotation is demonstrated in Fig. 6, where a 1-GHz-bandwidth pulse polarized in the x-direction is rotated into the y-direction by increasing an applied magnetic field from zero to 230 G. This high-fidelity $\pi/2$ rotation is accompanied by low
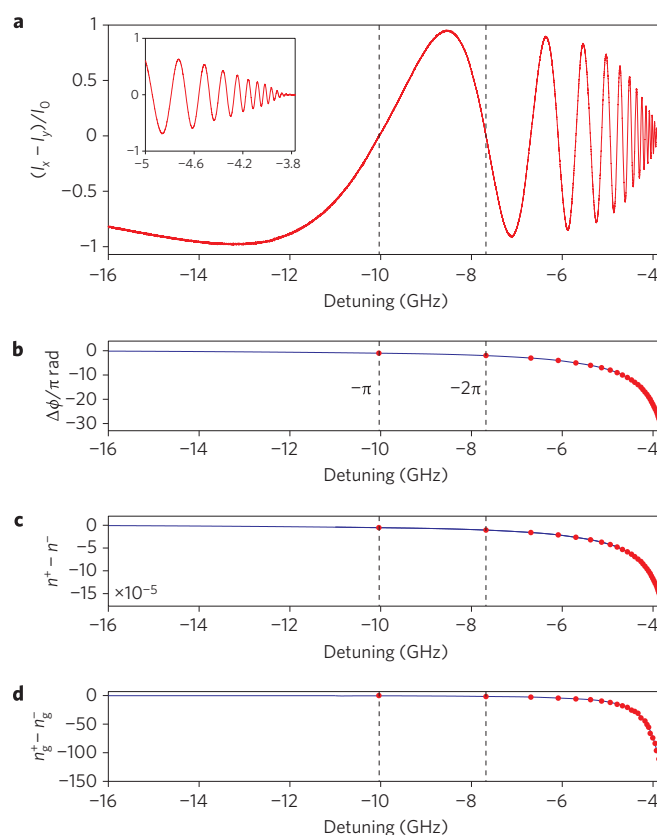

Figure 5 | Determination of relative phase and refractive indices using a c.w. beam. a, The difference signal obtained by subtracting the two orthogonal linear polarizations for an input polarization orientated at $\pi/4$ rad to the horizontal, for a vapour temperature of 135 °C and applied magnetic field of 230 G. The signal is normalized to the total intensity of the input. The inset shows a smaller range of detuning. **b**, The relative phase determined from the zero crossing of the difference signal (red points), with interpolated trend-line (blue curve). **c**, Relative refractive index calculated from the measured phase. **d**, Relative group index calculated from the gradient of the phase.

absorption (less than 2%) and negligible distortion because the pulse is detuned by many Doppler-broadened linewidths from resonance.

Discussion

For linearly polarized continuous wave (c.w.) light the plane of polarization is rotated by an angle dependent on the medium's relative phase index, and its spectral sensitivity is dependent on the relative group index. In Fig. 5 we showed that the relative phase and group indices can differ by more than six orders of magnitude, making the phase shift highly frequency dependent and hence of interest in the fields of interferometry and polarimetry. The Faraday rotation angle was seen to increase from zero at large detunings to 15π rad close to resonance, over a frequency range of ∼20 GHz. This rotation corresponds to a Verdet constant of 3×10^{-2} rad G^{-1} cm^{-1}, three orders of magnitude larger than that in typical commercial Faraday rotators[17]. Large rotations are also seen in thin magneto-optical photonic crystals[23], but the effect in such a system cannot be varied dynamically. The rotation in the atomic vapour is temperature, magnetic-field and frequency dependent, therefore the effect can be used as a tunable polarization switch. In addition, we recall that polarimetry provides a useful spectroscopic tool with applications in, for example, laser frequency stabilization[24]. The large bandwidth of off-resonant polarimetry could provide a useful technique to probe fast dynamics of Rydberg states in a thermal
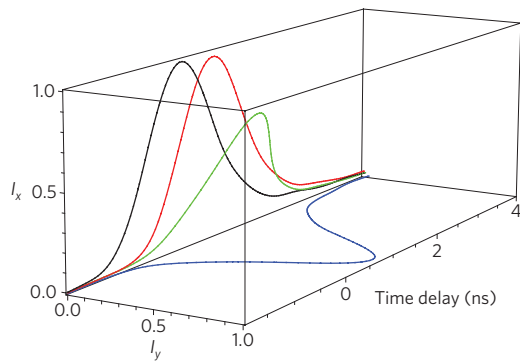
Figure 6 | Broadband Faraday rotation in a slow-light medium. An input 1.5-ns pulse initially linearly polarized in the *x*-direction (red) is delayed by 0.6-ns with respect to a non-interacting reference pulse (black), in the absence of an applied magnetic field. The pulse is red-detuned from the weighted D_1 transition centre by ~10 GHz. For a temperature of 135 °C and a field of 80 G (green) or 230 G (blue) the pulse is rotated into the *y*-direction while retaining its linear polarization and intensity.

vapour[25,26] or atomic beam[27] in the high-density regime where interactions and hence novel nonlinear optical effects are significant.

For broadband pulses, with spectral widths of hundreds of megahertz to gigahertz, in the wings of a resonance the Faraday effect manifests itself as an asymmetry in the propagation of left/right circularly polarized light. If the linearly polarized pulse's bandwidth is narrow enough such that the relative phase shift across it is essentially constant, the polarization angle is rotated in the same way as for c.w. light. Far from resonance, a gigahertz-bandwidth pulse can be rotated by $\pi/2$ rad with less than 2% loss and negligible distortion. Light switching with such large bandwidth and low loss/distortion has not been observed previously using atomic ensembles. Pulses as short as 5 ns have previously been rotated using self-induced transparency (SIT)[28]. However, this resonant technique requires intensities above saturation and the near-resonant character of the process leads to higher-order dispersive terms, resulting in considerable pulse distortion.

Increasing the phase variation across the pulse, for example by changing the applied field or carrier detuning, changes a single rotated linear pulse to split circular pulses in a dynamic way. Splitting a pulse into two components separated by more than their temporal widths could be used for pump-probe experiments, or for photon switching or atomic ensemble entanglement[29] in quantum information applications. The time separation of the two pulses can be controlled by varying the cell temperature or applied magnetic field.

At higher temperatures and magnetic fields, the available bandwidth of many gigahertz makes it possible for pulses with durations of hundreds of picoseconds to be delayed and rotated with high transmission. An appropriate choice of atomic species and laser wavelength opens up the possibility of communications at the large bit rates required for rapid data transfer in areas such as submarine communication, using, for example, the Cs $6^2P_{3/2} \rightarrow 8^2S_{1/2}$ transition at 455 nm (ref. 20) or Sr $5s^{2\,1}S_0 \rightarrow 5s5p^1P_1$ at 461 nm (ref. 27), and fibre-optics using, for example, Rb $5p^2P_{3/2} \rightarrow 4d^2D_{5/2}$ at 1.53 µm.

Outlook. The slow-light Faraday effect allows dynamic control of pulse shape and polarization. Because this control is implemented by means of the applied magnetic field, fast switching times of 1 µs or less would be difficult to achieve. However, the asymmetry in left and right circular polarizations due to the magneto-optical effect is not unique; any phenomenon that causes a change in the dispersive properties of a medium can lead to circular birefringence. An alternative method is to redistribute population in the magnetic

sublevels by optical driving. A distribution that produces different coupling strengths for the two circular polarizations leads to the same effects described in this paper. Augmenting (or replacing) the Faraday effect with optical control will potentially allow faster reconfiguration times than are possible by using alteration of the applied magnetic field. Hence any tunable device based on optical control would have faster switching times. The large bandwidth of the slow light makes possible the probing of atomic dynamics on a timescale much shorter than the excited-state lifetime. The application of the effect to probe the coherent evolution of strongly driven thermal Rb atoms will be the focus of future work.

Methods

The slow-light effect and relative dispersion. In this section we explain the advantages of working far from resonance in atomic media, and how a large group refractive index can lead to large relative dispersion. The two basic requirements of a slow-light medium are that it must have a large group index while at the same time being relatively transparent. These needs are met in an off-resonant Doppler-broadened system. To illustrate this we will assume that the laser detuning, $\Delta = \omega - \omega_0$ (laser angular frequency minus resonant angular frequency), is greater than the Doppler-broadened linewidth $\Delta\omega_D$. In this case, the atomic resonance can be approximated by a Lorentzian shaped distribution, with a natural linewidth Γ (ref. 4). Then for $\Delta > 2\Delta\omega_D > \Gamma$ the absorption coefficient, α, and phase and group indices can be approximated by

$$\alpha = Ck\Gamma/(2\Delta^2) \tag{1}$$

$$n - 1 = -C/(2\Delta) \tag{2}$$

$$n_g - 1 = C\omega_0/(2\Delta^2) \tag{3}$$

where k is the wavenumber of the light, and the constant C depends on factors such as the atomic density[22]. Comparing equations (1) and (2) we see that the absorption decreases at a faster rate than dispersion at increased detuning, so dispersive effects can be observed at high transmission (where α is small). In equation (3), the resonant angular frequency $\omega_0 \approx 2 \times 10^{15}$ rad s^{-1}, and consequently n_g is large even though $|n - 1| \approx 10^{-4}$ for Rb vapour at 100 °C. Assuming that the shift caused by an applied magnetic field is small such that it acts with equal magnitude, a, but opposite sign on the σ^+ and σ^- transitions, the relative group refractive index is $n_g^+ - n_g^- = C\omega_0(1/2(\Delta - a)^2 - 1/2(\Delta + a)^2)$. This reduces to $(4a/\Delta)(C\omega_0/(2\Delta^2))$ for $\Delta \gg a$. Thus the ratio of $n_g^+ - n_g^-$ to n_g is approximately $4a/\Delta$; the Zeeman shift is typically hundreds of megahertz for a field of hundreds of gauss, so for a detuning of a few gigahertz this ratio is greater than 0.1. Hence, in a slow-light medium where n_g is large, the relative group index can also be large.

Spectral sensitivity of Faraday rotation. Here we derive an expression for the spectral sensitivity of the Faraday effect, that is, the rate of change of rotation with frequency. In a birefringent medium of length L, the phase shift, $\Delta\phi$, between two co-propagating waves a and b is produced by a differing optical path length $L(n^a - n^b) = L\Delta n$, where n^i is the phase index experienced by wave i, and Δn is the relative refractive index. The phase shift between the two waves is given by[30]

$$\Delta\phi = \frac{\omega}{c}L(n^a - n^b) = L(k^a - k^b) \tag{4}$$

where ω is the angular frequency of the waves, and the wavenumber $k = \omega n/c$ is introduced to simplify calculations later on. Both n and k are taken to be real.

In dispersive media, n is a function of ω. Changing the angular frequency by an amount $\delta\omega$ produces a change in relative phase $\delta\Delta\phi$ given by

$$
\begin{aligned}
\delta\Delta\phi(\omega, L) &= \Delta\phi(\omega + \delta\omega, L) - \Delta\phi(\omega, L) = L[\Delta k(\omega + \delta\omega) - \Delta k(\omega)] \\
&= L\left[\Delta k(\omega) + \frac{d\Delta k(\omega)}{d\omega}\delta\omega + \frac{1}{2!}\frac{d^2\Delta k(\omega)}{d\omega^2}\delta\omega^2 + \ldots - \Delta k(\omega)\right] \\
&= \frac{L}{c}\left[\Delta n_g(\omega) + \frac{1}{2!}\frac{d\Delta n_g(\omega)}{d\omega}\delta\omega + \ldots\right]\delta\omega
\end{aligned}
\tag{5}
$$

Here $\Delta n_g = n_g^a - n_g^b$ is the relative group refractive index, and $d\Delta n_g/d\omega$ is the relative group velocity dispersion. The group velocity dispersion leads to broadening of optical pulses, while terms of higher order in the Taylor expansion lead to distortion.

In the limit that $\delta\omega \to 0$, equation (5) becomes

$$\frac{\mathrm{d}(\Delta\phi)}{\mathrm{d}\omega} = \frac{L}{c}\Delta n_{\mathrm{g}} \qquad (6)$$

A small change in frequency thus produces a change in relative phase proportional to the relative group refractive index. Thus the larger a medium's Δn_{g}, the higher its spectral sensitivity.

The Faraday effect arises due to the phase shift between the two orthogonal circular components of a linearly (or in general, elliptically) polarized wave. These components ($+$ and $-$) take the place of waves a and b in the foregoing example, and the relative phase between them manifests itself as a rotation of the composite wave. Therefore, while $n^+ - n^-$ determines the magnitude of the rotation, $n_{\mathrm{g}}^+ - n_{\mathrm{g}}^-$ describes the spectral dependence of this rotation. Because these quantities can vary by several orders of magnitude in a slow-light medium, the Faraday rotation is extremely sensitive to a variation in frequency.

Balanced polarimetry. In order to determine the relative phase shift between the circular components of light we use a balanced polarimeter[31]. We set a polarization beamsplitter at $\pi/4$ rad to the linearly polarized light such that in the absence of any optical rotation there is an equal amount of vertical and horizontal light incident on separate photodetectors. By subtracting the two signals we are left with a zero background; a small change in the amount of light in either linear polarization can be easily detected. For an input polarization $\mathbf{e} = 1/\sqrt{2}(\hat{\mathbf{x}} + \hat{\mathbf{y}})$, the output intensity signals for an initial intensity $I_0 = I_{x0} + I_{y0}$ are[24]

$$I_x - I_y = I_0 \sin(\Delta\phi)\mathrm{e}^{-(\alpha^+ + \alpha^-)L/2} \qquad (7)$$

$$I_x + I_y = \frac{1}{2}I_0(\mathrm{e}^{-\alpha^+ L} + \mathrm{e}^{-\alpha^- L}) \qquad (8)$$

Notice in equation (7) that the period of oscillation does not depend upon any attenuation due to the absorption coefficients $\alpha^{\pm}$: the difference signal is sensitive to optical rotation while being insensitive to ellipticity induced through circular dichroism.

Experimental method. The experimental setup is seen in Fig. 6. The source of both the c.w. and pulsed light was a Toptica DL100 external cavity diode laser (ECDL) with wavelength of 795.0 nm. The beam had a $1/e^2$ radius of (2.00 ± 0.05) mm. The light was then split using a $\lambda/2$ plate and polarization beamsplitter cube (PBS). Most of the light was used to produce an optical pulse, a small fraction was used for the c.w. spectroscopy. The (1.5 ± 0.2) ns full-width at half-maximum (FWHM) pulse has a peak intensity of 4 mW mm^{-2}. The pulse temporal profile is approximately a Gaussian profile, and therefore has a spectral FWHM of $\sim$300 MHz and bandwidth of $\sim$1 GHz; the bandwidth is here defined as the frequency range containing 99% of the pulse spectrum. The pulse was produced using a Pockels cell (PoC) placed between two crossed polarizers, which was driven by a pulse generator with a repetition rate of 50 Hz. The polarizations of the separate beams were then adjusted with waveplates before entering the vapour cell, and the c.w. beam was attenuated to 30 nW mm^{-2} such that it was in the weak-probe limit[22]. The 75-mm fused silica cell contained a mixture of the two naturally occuring isotopes of Rb according to the ratio ^{87}Rb : ^{85}Rb of 99 : 1. The cell windows were angled to prevent etalon fringes due to back-reflection. The cell was placed in a solenoid heating unit, based on the design of ref. 32. The current produced both the magnetic field and Joule heating required for the experiment; data requiring zero applied field were taken by briefly turning off the current. The variation in magnetic field along the cell was $\sim$10%. No attempt was made to shield the apparatus from the laboratory field.

References

1. Krauss, T. F. Why do we need slow light? *Nature Photon.* **2,** 448–450 (2008).
2. Hau, L. V., Harris, S. E., Dutton, Z. & Behroozi, C. H. Light speed reduction to 17 metres per second in an ultracold atomic gas. *Nature* **397,** 594–598 (1999).
3. Vanner, M. R., McLean, R. J., Hannaford, P. & Akulshin, A. M. Broadband optical delay with a large dynamic range using atomic dispersion. *J. Phys. B* **41,** 051004 (2008).
4. Camacho, R. M., Pack, M. V., Howell, J. C., Schweinsberg, A. & Boyd, R. W. Wide-bandwidth, tunable, multiple-pulse-width optical delays using slow light in Cesium vapor. *Phys. Rev. Lett.* **98,** 153601 (2007).
5. Tanaka, H. *et al.* Propagation of optical pulses in a resonantly absorbing medium: observation of negative velocity in Rb vapor. *Phys. Rev. A* **68,** 053801 (2003).
6. Gauthier, D. J., Gaeta, A. L. & Boyd, R. W. Slow light: from basics to future prospects. *Photon. Spectra* **40,** 44–50 (2006).
7. Fleischhauer, M. & Lukin, M. D. Dark-state polaritons in electromagnetically induced transparency. *Phys. Rev. Lett.* **84,** 5094–5097 (2000).
8. Liu, C., Dutton, Z., Behroozi, C. H. & Hau, L. V. Observation of coherent optical information storage in an atomic medium using halted light pulses. *Nature* **409,** 490–493 (2001).
9. Phillips, D. F., Fleischhauer, A., Mair, A., Walsworth, R. L. & Lukin, M. D. Storage of light in atomic vapor. *Phys. Rev. Lett.* **86,** 783–786 (2001).
10. Shi, Z., Boyd, R. W., Gauthier, D. J. & Dudley, C. C. Enhancing the spectral sensitivity of interferometers using slow-light media. *Opt. Lett.* **32,** 915–917 (2007).
11. Purves, G. T., Adams, C. S. & Hughes, I. G. Sagnac interferometry in a slow-light medium. *Phys. Rev. A* **74,** 023805 (2006).
12. Shi, Z., Boyd, R. W., Camacho, R. M., Vudyasetu, P. K. & Howell, J. C. Slow-light fourier transform interferometer. *Phys. Rev. Lett.* **99,** 240801 (2007).
13. Urban, E. *et al.* Observation of Rydberg blockade between two atoms. *Nature Phys.* **5,** 110–114 (2009).
14. Gaëtan, A. *et al.* Observation of collective excitation of two individual atoms in the Rydberg blockade regime. *Nature Phys.* **5,** 115–118 (2009).
15. Aharonov, Y., Albert, D. Z. & Vaidman, L. How the result of a measurement of a component of the spin of a spin-1/2 particle can turn out to be 100. *Phys. Rev. Lett.* **60,** 1351–1354 (1988)
16. Hosten, O. & Kwiat, P. Observation of the spin Hall effect of light via weak measurements. *Science* **319,** 787–790 (2008).
17. Budker, D. *et al.* Resonant nonlinear magneto-optical effects in atoms. *Rev. Mod. Phys.* **74,** 1153–1201 (2002).
18. Awschalom, D. D. & Kikkawa, J. M. Electron spin and optical coherence in semiconductors. *Phys. Today* **52,** 33–38 (1999).
19. Atatüre, M., Dreiser, J., Badolato, A. & Imamoglu A. Observation of Faraday rotation from a single confined spin. *Nature Phys.* **3,** 101–106 (2007).
20. Menders, J., Benson, K., Bloom, S. H., Liu, C. S. & Krevaar, E. Ultranarrow line filtering using a Cs Faraday filter at 852 nm. *Opt. Lett.* **16,** 846–848 (1991).
21. Grischkowsky, D. Adiabatic following and slow optical pulse propagation in rubidium vapor. *Phys. Rev. A* **7,** 2096–2103 (1973).
22. Siddons, P., Adams, C. S., Ge, C. & Hughes, I. G. Absolute absorption on rubidium D lines: comparison between theory and experiment. *J. Phys. B* **41,** 155004 (2008).
23. Kahla, S. & Grishin, A. M. Enhanced Faraday rotation in all-garnet magneto-optical photonic crystal. *Appl. Phys. Lett.* **84,** 1438–1440 (2004).
24. Pearman, C. P. *et al.* Polarization spectroscopy of a closed atomic transition: applications to laser frequency locking. *J. Phys. B.* **35,** 5141–5151 (2002).
25. Mohapatra, A. K., Jackson, T. R. & Adams, C. S. Coherent optical detection of highly excited Rydberg states using electromagnetically induced transparency. *Phys. Rev. Lett.* **98,** 113003 (2007).
26. Mohapatra, A. K., Bason, M. G., Butscher, B., Weatherill, K. J. & Adams, C. S. A giant electro-optic effect using polarizable dark states. *Nature Phys.* **4,** 890–894 (2008).
27. Mauger, S., Millen, J. & Jones, M.P.A. Spectroscopy of strontium Rydberg states using electromagnetically induced transparency. *J. Phys. B* **40,** F319–F325 (2007).
28. Gibbs H. M., Churchill, G. G. & Salamo, G. J. Faraday rotation under cw saturation and self-induced transparency conditions. *Opt. Commun.* **12,** 396–399 (1974).
29. Hammerer, K., Sorensen, A. S. & Polzik, E. S. Quantum interface between light and atomic ensembles. arXiv:0807.3358v2 [quant-ph] (2008).
30. Boyd, R. W. *Nonlinear Optics*, 3rd edn (Academic Press, 2008).
31. Huard, S. *Polarization of Light* (Wiley, 1997).
32. McCarron, D. J., Hughes, I. G., Tierney, P. & Cornish, S. L. A heated vapor cell unit for dichroic atomic vapor laser lock in atomic rubidium. *Rev. Sci. Instrum.* **78,** 093106 (2007).

Author contributions

P.S. carried out the experiment and theoretical modelling, and contributed to the writing of the paper. N.C.B. and Y.C. assisted with the experiment. C.S.A. and I.G.H contributed to the writing of the paper and were responsible for project management.

Additional information

Reprints and permission information is available online at http://npg.nature.com/reprintsandpermissions/. Correspondence and requests for materials should be addressed to P.S.

Ultrashort pulse characterization

Pulse measurement equipment is now easier to use than ever before, with many devices offering easy-to-align solutions and plug-and-play computer operation, reports **Neil Savage**.

Ultrafast lasers, which produce pulses of light as short as a few femtoseconds, are of widespread interest in applications that require high peak power but need to have the power turned off before its effects, such as heat, can spread to surrounding materials. They are now a popular tool in applications ranging from materials processing and laser surgery to scientific research. For instance, chemists looking for new ways to synthesize pharmaceuticals with minimal waste are using them to study the chemical bonds of molecules. If they can shape an ultrafast pulse so that it matches the vibrational frequency of the molecule, they can cause the bonds to break in ways that would not naturally occur, giving the researchers greater understanding of and control over the reactions.

For such applications, researchers need to be able to characterize the pulses. "People are actually shaping pulses these days, making them extremely complicated in time and frequency," says Rick Trebino, a professor of ultrafast optics at Georgia Institute of Technology in Atlanta, USA, and president of pulse measurement company Swamp Optics.

Trebino says the methods used for characterizing pulses break roughly into three approaches. The first approach is to use autocorrelators. These split an ultrashort pulse into two, and overlap the two pulses in a nonlinear medium that provides second-harmonic generation, allowing users to measure the duration of the pulse. The second approach is the use of a frequency-resolved optical gating (FROG), which measures both temporal and frequency resolution of the pulse simultaneously.

The third and last approach, Trebino says, uses some form of spectral interferometry, such as spectral phase interferometry for direct electric-field reconstruction (SPIDER). Trebino argues that none of these methods is flawless. In fact, he calls autocorrelation "completely obsolete". Because the measuring pulse lasts as long as the measured pulse, it provides only blurry temporal resolution, he says. FROG, however, provides poor spatial resolution of pulses. SPIDER, Trebino says, can only measure simple pulses with small

time–bandwidth products (a measure of pulse complexity), and it tends to introduce chirp, which distorts the pulse being measured.

Trebino says that he and his group have resolved the issues with a new version of spectral interferometry that he calls Sea Tadpole. The approach uses a reference pulse to measure both the spatial and temporal profiles of a pulse's electrical field. He hasn't yet commercialized this new approach. "We've spent the last 20 years developing practical methods that work," Trebino says. "In my opinion, essentially all the problems have been solved. Getting those solutions into the laps of users in another story."

PRODUCT ROUND-UP

The Reef autocorrelators from **Del Mar Photonics** (San Diego, CA, USA) have been designed to determine laser pulse-width characteristics on a femtosecond timescale. The Reef-RT is a scanning, real-time autocorrelator that uses two-photon absorption as its detection method. It can analyse pulses with widths from 10 fs to 6 ps at a repetition rate from 10 kHz to continuous-wave mode-locked. The required minimum average power for a measurement is 1 mW at 100 MHz. The scan rate is variable from 0.1 to 20 Hz, with scan nonlinearity of less than 1%. The device is designed for input pulses with a linear horizontal polarization, but vertical polarization operation is available as an option. The wavelength range of operation is 700 to 1,000 nm and readout is by means of

an external oscilloscope. Del Mar also offers the Reef-SS, a single-shot autocorrelator with a pulse-width measurement capability from 20 to 500 fs. Pulse repetition rate compatibility is from 1 to 10 Hz for a single-shot pulse measurement, and >10 Hz for a multiple-shot measurement. Required input pulse energy at 1 to 10 Hz repetition rate is >500 nJ, at >1 kHz is >50 nJ, and at >10 MHz is >50 pJ. Readout is by means of a charge-coupled device (CCD) detector, and a USB connector provides interface with a PC.
www.dmphotonics.com

The single-shot Autocorrelator SSNA from **Altechna Co. Ltd** (Vilnius, Lithuania) displays and measures in real time the temporal pulse shape of a single light pulse with a duration from 30 fs to 40 ps. The autocorrelator relies on nonlinear second-harmonic generation, in which the spatial distribution of the second harmonic light contains information on the time behaviour of the fundamental light pulse, providing background-free measurement. The device is designed for use with many commonly used ultrashort pulse lasers. It can be built to make temporal shape measurements of pulses down to 30 fs duration in the spectral range from 523 to 1,400 nm, and with lower temporal resolution for wavelengths up to 4,000 nm. Using a linear photodiode array with the autocorrelator allows an oscilloscope to display the temporal shape of a single pulse with sufficient accuracy for laser and compressor adjustment.
www.altechna.com

DEL MAR PHOTONICS

The FROG Scan pulse measurement system from **Mesa Photonics** (Santa Fe, NM, USA) measures pulses in the 450- to 1,800-nm range with pulse widths from 15 fs to tens of picoseconds. A high-speed translation stage coupled with the included VideoFROG software allows the system to make measurements at a rate exceeding 2 Hz, with a 32 × 32 grid at approximately 70 spectra per second. Based on second-harmonic generation, the system operates on a multi-shot configuration, using a translation stage to scan a beam through different pulse delays and compare it to a beam sent through a fixed delay. Incorporating a spectrometer from Ocean Optics (Dunedin, Florida, USA) into the system allows it to collect 16-bit spectral data, improving dynamic range and sensitivity. The system has a temporal range of 30 ps, temporal resolution of 2 fs or better, spectral resolution from 0.2 to 1 nm, spectral range from 100 to 600 nm, time–bandwidth product >50, intensity accuracy of 2% and phase accuracy of 0.01 radians.
www.mesaphotonics.com

The LX SPIDER from **APE** (Berlin, Germany) uses the SPIDER technique for complete spectral and temporal characterization of femtosecond laser pulses. It uses a single crystal to up-convert the two test pulse replicas and to introduce spectral shear without the need for an additional chirped pulse. By measuring the pulse's spectral amplitude and phase, its temporal amplitude and phase can be derived in real time. The LX measures 180 × 215 × 100 mm, and APE says that it has an automatic calibration feature that reduces calibration time to a few seconds. The device performs real-time measurements in the 750- to 900-nm wavelength range. Several optics sets for different measurement criteria are available. One optics set measures pulses with a spectral bandwidth of 13 to 40 nm and duration of 25 to 80 fs. It can also make less accurate measurements down to 16 fs and 65-nm bandwidth. The other optics set measures pulses with a bandwidth of 5 to 15 nm and a duration of 70 to 200 fs. For measurements, minimum required input power is 10 mW at 80 MHz and 80 fs. The required input polarization is linear and input beam height is 70 mm.
www.ape-berlin.com

The FROG pulse analyser from **Southern Photonics** (Auckland, New Zealand) is optimized for high-speed optical communications systems. The analyser uses complete optical phase recovery, measuring both pulse shape and phase so that bias and modulation depth can be optimized and any chirp characterized. The device suits use with almost any return-to-zero pulse type, and works with mode-locked sources, directly modulated lasers and externally modulated lasers. The high-resolution model HR 150 offers spectral resolution of 50 pm, temporal resolution of 15 fs and pulse temporal range (full width at half maximum, FWHM) of 0.3 to 10 ps, with options available for longer pulses if required. Spectral range of operation is from 1,520 to 1,610 nm, with spectral bandwidth of 10 nm. The 1-μm-wavelength Yb-FROG SR 100 analyser, designed for use with Yb-fibre lasers and other sources at 1-μm wavelength, has a temporal range (FWHM of pulses) of 500 fs to 10 ps, temporal resolution of 15 fs, spectral range from 1,000 to 1,100 nm, and spectral resolution of 0.25 nm. The ultra-short-pulse model HR200 version has a temporal range (FWHM of pulses) of 50 fs to 5 ps, temporal resolution of 0.5 fs, spectral bandwidth of 50 nm and spectral resolution of 0.5 nm.
www.southernphotonics.com

The Grenouille range of pulse analysers from **Swamp Optics LLC** (Atlanta, Georgia, USA) are based on second-harmonic generation FROG and are able to measure pulse intensity and phase as a function of time as well as pulse spectrum and spectral phase. Versions for use with either Ti:sapphire lasers or short-pulse lasers operating in the near-infrared are available. According to Swamp Optics, their Grenouille devices are much easier to use than autocorrelators with no difficult alignment and minimal weight and size: it is simply a case of placing the device in the beam and connecting a USB cable to a laptop computer. Five models for use with Ti:sapphire lasers are now available, allowing pulse measurements between 700 and 1,100 nm for pulse lengths ranging from 10 fs to 5 ps. The accuracy of intensity and phase measurements is specified as 2% and 0.01 rad respectively. A collimated 2 to 4-mm-diameter input beam is required. Four versions for use with near-infrared lasers cover the spectral range from 0.9 to 1.62 μm and can measure pulses as short as 40 fs up to 1 ps. The analysers are capable of free-running and triggered single-shot measurements with a sensitivity of 1 μJ.
www.swampoptics.com

The Phazzler PH-S-750-850 dual-mode femtosecond pulse shaping and measurement system from **Fastlite** (Paris, France) includes an autocorrelator and uses SPIDER to measure transform-limited pulses and FROG for measuring complex pulse shapes. The Phazzler is fully computer controlled and requires no realignment when switching between measurement techniques. For repetition rates below 30 kHz, it has a pulse measurement range of 20 to 700 fs, a centre wavelength range from 750 to 850 nm, and requires a minimum energy of 1 μJ per pulse. For repetition rates from 30 kHz to 300 kHz or more, it has a pulse measurement range of 60 to 700 fs and a centre wavelength range from 720 to 930 nm. Between 30 and 300 kHz it requires minimum energy of 100 nJ per pulse, and above 300 kHz 2 nJ per pulse. Input polarization is vertical, maximum input energy is 30 μJ, and maximum input diameter is 2.5 mm.
www.fastlite.com

The FR-103MC is a palm-size autocorrelator from **Femtochrome Research** (Berkeley, CA, USA). It can be configured for interferometric operation with a two-photon conductivity photosensor, or background-free operation with a nonlinear crystal and second-harmonic generation. It handles

pulse widths from 10 fs to 10 ps and an input sensitivity $(P_{av}P_{pk})_{min}$ of 10^{-5} W^2. Resolution is <3 fs and scan range is >40 ps. Wavelength range of operation is 500 to 3,000 nm. The device is polarization-insensitive. It can be provided either with a free-space or a fibre-coupled input. It can also be equipped with a computer data acquisition option for the display and analysis of autocorrelation traces using a PC. The standard version is suitable for pulse repetition rates >10 kHz. With the computer data acquisition option, it can handle any input pulse rate >5 Hz. A second version, the FR-103TPM, provides a high-resolution pulse-width monitor for two-photon microscopy applications.
www.femtochrome.com

The HAC-150 femtosecond autocorrelator from **Alnair Labs** (Tokyo, Japan) offers characterization of light pulses in the telecommunication window (1,400-1,650 nm) and claims to be alignment-free and polarization-insensitive. The analyser, which connects to a computer through a USB port, is designed for 'plug-and-measure' operation and uses two-photon

absorption to provide a high measurement sensitivity. Autocorrelation traces and key pulse parameters of measured pulses are displayed in real time on the PC. The HAC-150 is available with a range of fibre-input connectors (FC or SC, APC or SPC).

It can measure pulses from 0.1 ps to 15 ps and has a resolution of 25 fs and a refresh rate of 5 Hz. The unit measures $110 \times 110 \times 210$ mm.
www.alnair-labs.com

The Femtometer from **Femtolaser Produktions GmbH** (Vienna, Austria) is a Michelson-interferometer-based autocorrelator for ultrashort pulse characterization that comes complete with software for data acquisition, processing and evaluation. The company says that this is the only computerized pulse characterization tool that provides access to the timescale of the oscillation period of light, allowing the measurement of few-cycle pulses. Its dispersion-compensated design offers high-fidelity pulse measurement down to 5 fs. The use of removable detection modules

provides flexibility. A fast detector with a megahertz response can characterize ultrafast oscillators, and a kilohertz detector measures amplified pulses. The Femtometer can be operated as a plain Michelson interferometer, and a special megahertz detector is available for measurements in the focus of microscopes. The Femtometer connects to a laptop for data acquisition. The interferometer head has a spectral range of 650 to 950 nm. The spectrometer head has a spectral range of 550 to 1,050 nm, with input either through free space or optical fibre. It evaluates pulses from 5 to 150 fs, with a range up to 350 fs optional.
www.femtolasers.com

NEIL SAVAGE is a freelance science and technology journalist based in Lowell, Massachusetts, USA.

The mention of a company's name or product is not an endorsement by Nature Photonics *and* Nature Photonics *takes no responsibility for the accuracy of the product information or the claims made by companies.*

Practical plasmonics

Magnetic hard disk technology is approaching its limits. *Nature Photonics* spoke to William Challener, Ed Gage and Mark Re from Seagate about their demonstration of heat-assisted magnetic recording.

■ What are the current approaches for recording data?

When considering rotating media, hard disk drives and optical disk drives are the standard. Magnetic hard drives are approaching their technological limit and optical drives are stuck at the diffraction limit (roughly half the wavelength).

### ■ What are the limitations of the current magnetic and optical approaches?

The problem is that as areal density increases the magnetic grain has to keep getting smaller to maintain the signal-to-noise ratio. However, the stability of the grain's magnetic state is proportional to the volume. As the grains get smaller, they become much less stable until finally just the kT — the thermal energy — can randomly reverse the magnetic state of the grain. It is a little bit uncertain, but projections for the ultimate limit for magnetic hard drives are of the order of a terabit per square inch.

Far-field optical approaches have diffraction-limited spot sizes. Blu-ray optical disks use a far-field approach at a short wavelength of 405 nm with a large numerical aperture of 0.85. That gives you a spot size of the order of 240 nm. To get to Tb in^{-2} densities you need to record marks with an area of $(25 \text{ nm})^2$, which would require optical spot sizes about 50 nm in diameter (or much less than that), well below the diffraction limit and beyond the capability of Blu-ray. The biggest challenge is to transfer optical energy into the recording medium in a sub-diffraction-limited spot, efficiently.

■ What is HAMR?

HAMR is an acronym that we invented here for heat-assisted magnetic recording. The process is similar to conventional magneto-optic recording in that we are using a laser beam to heat a magnetic layer to record information on it in a high-temperature state which then becomes stable when it cools back down.

HAMR combines optical storage technology with conventional magnetic technology, but there are important distinctions. Magneto-optic recording is done by using a larger unconfined external magnetic field and modulating the focused laser at the data rate to store information,
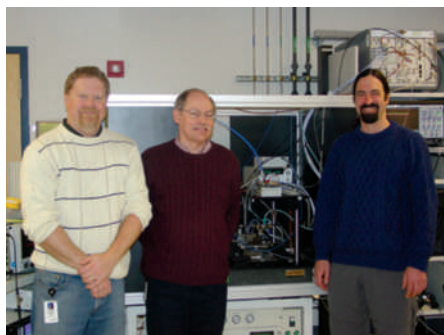
Edward Gage (left), William Challener (centre) and Mark Re (right) at Seagate, in Pittsburgh.

whereas in HAMR the laser is constantly on and we modulate the high magnetic field near the optical spot. We fly a transducer just 15 nm above a recording medium at 2,700 r.p.m. In our case, we confine our spot to below 50 nm. If our light spills over, it begins to heat the neighbouring tracks and erase previously recorded information. Also, in read back, in magneto-optic approaches that is done optically by looking at the polarization state of the reflected light, but we have a magnetic sensor on the recording head measuring the magnetic state of the recorded track. HAMR should be able to go an order of magnitude higher in density than the products now on the market, but nobody knows yet how far we can go.

■ What is important when designing the actual recording head?

The head had to be compatible with the standard fabrication processes in the hard disk drive industry: lithography and thin-film type techniques. A near-field transducer that could be easily fabricated by lithography in the wafer processing stage, not in a subsequent stage after the wafer had been diced, was crucial. The more processing you have to do at later stages, the more expensive it becomes.

■ What sets your work apart from previous HAMR studies?

Other groups have done HAMR but with a static head which uses piezo systems to scan the head. The systems are not integrated. The biggest difference here is that we have a completely integrated head — flying over

the rotating recording medium — with recording pole, reader and optics. We have also done static testing and we know the challenges in going to a real flying head. The other big step was going to materials that have the potential to be used in real HAMR products. Previous attempts had used materials that were convenient for demonstrations but not really capable of high-density data storage.

■ What data density did you achieve in your proof-of-principle work?

We use light at a wavelength of 830 nm and have a track width of less than 80 nm, which is less than one-tenth of a wavelength. With a 15 dB signal-to-noise ratio, we achieved an areal density of the order of 350 Tb m^{-2} (0.2 Tb in^{-2}). This is a higher density than we were able to achieve without a near-field plasmonics transducer using blue-wavelength light.

■ What are the remaining challenges before commercialization?

What we have done is demonstrated the proof-of-principle. There are still lots of engineering challenges that have to be addressed. For example, one thing we didn't really go into in the paper is a practical way to deliver the light to the recording head. That could be through an optical fibre or placing a laser directly onto the recording head; these types of issues still have to be figured out. The recording medium itself currently would not allow a small enough head-to-medium spacing to get to the Tb in^{-2} areal data density. The surface smoothness and grain size need to be improved. There are certainly thermal issues too. We need to look into the repeated heating and cooling of the head and those kinds of things.

We are expecting HAMR not to change the cost of a drive significantly and to reduce the cost per gigabyte. The only additional component is the laser diode, which is similar to those used in today's inexpensive CD recorders. Those drives cost significantly less than our hard drives today.

INTERVIEW BY DAVID PILE.

William Challener and his team have a Letter on heat-assisted magnetic recording on page 220 of this issue.